ABSTRACT

Title of Document: WAFER-SCALE PROCESS AND MATERIALS OPTIMIZATION IN CROSS-FLOW ATOMIC LAYER DEPOSITION

Laurent Christophe Lecordier,
Doctor of Philosophy, 2009

Directed By: Professor Gary W. Rubloff
Department of Materials Science and Engineering

The exceptional thickness control (atomic scale) and conformality (uniformity over nanoscale 3D features) of atomic layer deposition (ALD) has made it the process of choice for numerous applications from microelectronics to nanotechnology, and for a wide variety of ALD processes and resulting materials. While its benefits derive from self-terminated chemisorbed reactions of alternatively supplied gas precursors, identifying a suitable process window in which ALD's benefits are realized can be a challenge, even in favorable cases.

In this work, a strategy exploiting in-situ gas phase sensing in conjunction with ex-situ measurements of the film properties at the wafer scale is employed to explore and optimize the prototypical Al_2O_3 ALD process. Downstream mass-

spectrometry is first used to rapidly identify across the [H_2O x $Al(CH_3)_3$] process space the exposure conditions leading to surface saturation. The impact of precursor doses outside as well as inside the parameter space outlined by mass-spectrometry is then investigated by characterizing film properties across 100 mm wafer using spectroscopic ellipsometry, CV and IV electrical characterization, XPS and SIMS.

Under ideal dose conditions, excellent thickness uniformity was achieved (1σ/mean<1%) in conjunction with a deposition rate and electrical properties in good agreement with best literature data. As expected, under-dosing of precursor results in depletion of film growth in the flow direction across the wafer surface. Since adsorbed species are reactive with respect to subsequent dose of the complementary precursor, such depletion magnifies non-uniformities as seen in the cross-flow reactor, thereby decorating deviations from a suitable ALD process recipe. Degradation of the permittivity and leakage current density across the wafer was observed though the film composition remained unchanged. Upon higher water dose in the over-exposure regime, deposition rates increased by up to 40% while the uniformity degraded. In contrast, overdosing of TMA and ozone (used for comparison to water) did not affect the process performances. These results point to complex saturation dynamics of water dependent on partial pressure and potential multilayer adsorption caused by hydrogen-bonding.

WAFER-SCALE PROCESS AND MATERIALS OPTIMIZATION
IN CROSS-FLOW ATOMIC LAYER DEPOSITION

By

Laurent Christophe Lecordier

Dissertation submitted to the Faculty of the Graduate School of the
University of Maryland, College Park, in partial fulfillment
of the requirements for the degree of
Doctor of Philosophy
2009

Advisory Committee:
Professor Gary W. Rubloff, Chair
Professor Elisabeth Smela
Professor Ichiro Takeuchi
Professor John Cumings
Professor Oded Rabin

© Copyright by

Laurent Christophe Lecordier

2009

Dedication

To my wife, Mary, for all her support, patience and love.

Acknowledgements

I would like to first acknowledge all the Rubloff group members, past and present, with whom I have had the privilege and pleasure to work with over the past twelve years at the University of Maryland. I must address special thanks to Dr Wei Lei with whom I started the ALD adventure in 2003 as well as Dr Yiheng Xu and Pr Theodosia Gougousi who were my first co-workers when I arrived at UMD and who taught me many of the skills that have allowed me to get to this point. More recently, Erin Robertson, Parag Banerjee and Dr. Israel Perez have been my closest collaborators and friends and I sincerely thank them for their help in the lab and the many fruitful discussions we have had together. I would also like to thank the staff at the UMD Nanocenter Fablab for their kind advice and instruction.

I am most grateful to my committee members for spending the time reviewing this thesis and providing me guidance throughout this work.

I certainly would like to acknowledge Dr Mariano Anderle, who worked with me on this project during his summer visits in 2007 and 2008. It was one of the highlights of this project to have Dr Anderle around. His dedication at work and enthusiasm for life were most valuable to me. I am also very grateful that he provided me access to the resources at the Bruno Kessler Foundation (Trento, Italy).

Most of all, I would like to address my most sincere gratitude and appreciation to Pr Gary Rubloff who has always been an outstanding advisor, mentor and friend.

Finally I would like to acknowledge our funding partners without whom this work would not have been possible. This work has been partially supported by the UMD-NSF-MRSEC under grant DMR 05-20471, the NSF-IMI under grant DMR-0231291, the Laboratory for Physical Sciences, and MKS Instruments.

Table of Contents

Dedication ... ii

Acknowledgements ... iii

Table of Contents ... v

List of Tables ... ix

List of Figures ... x

Chapter 1: Introduction ... 1

1.1 - Background on Atomic Layer Deposition ... 1

1.2 - Details of ALD process sequence ... 4

1.3 - Process requirements to achieve self-terminated ALD ... 7

1.3.1 Precursors ... 7

1.3.2 Sample preparation ... 8

1.3.3 Saturating exposures ... 9

1.3.4 Purge window ... 10

1.3.5 Temperature window ... 11

1.4 - Impact of reactor design on film deposition ... 12

1.4.1 Cross-flow channel vs. top injection design ... 12

1.4.2 Precursor delivery ... 14

1.5 - Impact of reactant partial pressure on adsorption ... 16

1.5.1 Examples ... 16

1.5.2 Adsorption equilibrium in ALD ... 18

1.6 - Motivation and objectives ... 19

1.7 - Organization of the thesis 23
Chapter 2: Experimental setup 25
2.1 - ALD system 26
2.1.1 Reactor design 26
2.1.2 Gas delivery and reactant dose control 29
2.1.3 Process control 31
2.2 - Quadrupole mass spectrometry 33
2.2.1 Operational principles 33
2.2.2 MKS Vision 1000C mass-spectrometer 35
2.3 - Spectroscopic ellipsometry (SE) 36
2.3.1 Operational principles 36
2.3.2 Sopra GES5 ellipsometer 39
2.4 - CV and IV electrical characterization 40
2.4.1 Operational principles 40
2.4.2 Automated probe station for electrical characterization 41
2.4.3 MOS and MIM capacitor fabrication 43
Chapter 3: In-situ process optimization using mass-spectrometry 45
3.1 - Introduction 45
3.2 - Review of in-situ sensing methodologies used in ALD 46
3.3 - Review of prior work in W ALD 50
3.4 - Experimental setup 52
3.5 - QMS-based optimization for reactant exposures 53
3.6 - In-situ exploration of ALD process space 55

3.7 - Prediction of thickness uniformity using QMS 59

3.8 - Real-time monitoring of nucleation kinetics 61

3.9 - Discussion and conclusion.. 62

Chapter 4: Cross-wafer thickness uniformity in Al_2O_3 ALD 65

4.1 - Introduction 65

4.2 - Experimental protocol 66

4.3 - Results: across-wafer uniformity... 67

4.3.1 Effect of water dosing on thickness uniformity....................................... 67

4.3.2 Effect of TMA dosing on thickness uniformity...................................... 69

4.3.3 Effect of dose ratio.. 71

4.3.4 Results: uniformity and purge times... 73

4.3.5 Al_2O_3 ALD from TMA and ozone... 75

4.4 - Discussion and conclusion.. 77

Chapter 5: Characterization of Al_2O_3 intrinsic properties 84

5.1 - Introduction 84

5.2 - Al_2O_3 electrical and optical properties 85

5.2.1 Experimental.. 85

5.2.2 Results.. 86

5.3 - Surface analysis 91

5.3.1 Experimental.. 91

5.3.2 Dynamic SIMS results 92

5.3.3 XPS measurements 94

5.4 - Conclusions 96

Chapter 6: Conclusion and Future Work 98

6.1 - Conclusion 98

6.2 - Future work 102

Appendices 105

Bibliography 122

List of Tables

Table 1 – Short list of materials deposited by ALD.[41] Puurunen listed more than 75 elements and 125 compounds that could be deposited by ALD in its 2005 review.[3] 4

Table 2 – Key precursor requirements [43] 8

Table 3 – Reactant control temperatures and vapour pressures.................................. 29

Table 4 – Process conditions for wafers characterized by XPS and SIMS 91

Table 5 – XPS results showing atomic percentage of elements present on the surface of sample A for 7 positions across the wafer. Ratio of oxygen to aluminium is listed in the last column. 95

List of Figures

Figure 1 – Linear correlation between cycle number and deposited thickness in ZrO_2 ALD at 275˚C. [4] 1

Figure 2 – TEM image of 210 Å hafnium aluminate film deposited by ALD into high aspect ratio SiO_2 features. [4] 1

Figure 3 – Example of nanolaminate TiO_2 / Al_2O_3 ALD nanolaminate.[5] 1

Figure 4 – Yearly publications related to ALD. Based on online search in ISI Web of Science, (Sept. 2009) 2

Figure 5 –Sequence of alternating reactant exposures and purges during one Al_2O_3 ALD cycle with TMA and water. In this specific case, the reaction by-product is the same for both half reactions, i.e., methane CH_4.. 5

Figure 6 - Nucleation retardation in HfO_2 ALD. Hf surface coverage measured by RBS based on different surface preparations (circles: Hf-last, squares: chemical oxide, stars: rapid thermal oxides, plus: rapid thermal oxinitride). Source: [44] 9

Figure 7 – Al_2O_3 deposition rate as function of purge time and H_2O exposure time. Saturating self-limited reactions ensure that the deposition rate reaches a plateau once the reactant doses are at or above saturation level. Source: [45] 9

Figure 8 – ALD process windows showing deposition rate as a function of (a) purge times and (b) process temperature. 11

Figure 9 – Dependence of the Al_2O_3 growth rate with the H_2O pulse length at (a) small ($8x10^{-6}$ g/s) and (b) large ($2x10^{-4}$ g/s) water flow rates. [38].......................... 17

Figure 10 – Thickness profile of Al_2O_3 films as a function of process pressure.[54] 17

Figure 11 – UHV ALD reactor – a) ALD platform with load-lock and ALD chamber. b) Embedded mini ALD reactor in UHV chamber. c) Schematic of ALD chamber.. 27

Figure 12 – Cross-section of mini-reactor 28

Figure 13 – View of the 100 mm diameter substrate heater with visualization of flows across the wafer.. 28

Figure 14 – Schematic of gas delivery setup. TMA and water vapours are introduced in volume V until pressure P is reached prior to release through dose valves............ 31

Figure 15 – Record of maximum and minimum pressures in TMA delivery volume over 100 cycles. Estimated doses (open diamonds) are shown on the right axis. 31

Figure 16 – Schematic of quadrupole mass spectrometer (QMS) 33

Figure 17 – MKS Vision 1000-C QMS integration downstream to ALD reactor...... 36

Figure 18 – Ellipsometry measures the change of polarization upon reflection of a linear polarized light on a surface. Upon interference with the film, the reflected light is elliptically polarized. The measured phase change Δ and amplitude change ψ reflect film properties, thickness and refractive index.[66] 38

Figure 19 - Configuration of the Sopra GES5 ellipsometer. 39

Figure 20 – Matlab renditions of electrical properties for 15 nm Al_2O_3 film deposited under underdosed water conditions. CV/IV characteristics measured over 190 Au / Al_2O_3 / Si capacitors. a) Capacitance map based on measurement at 10kHz and -2V. b) Leakage current map. Current determined at -1MV/cm field. Flow direction is along vertical axis from bottom to top.. 42

Figure 21 – Schematics of metal-insulator-metal (MIM) and metal-oxide-semiconductor (MOS) capacitors. 43

Figure 22 - Mass-spec signals observed during one W ALD cycle. H_2 and SiF_4 by-product generations, occurring respectively during the SiH_4 and WF_6 exposures, clearly reveal the self-limited nature of ALD chemistry. [56].................................. 50

Figure 23 - Integrated SiF_4 mass-spec signals computed as function of respective cycle number. The nucleation regime from cycle 0 to 30 is clearly identified and followed by a plateau indicating a linear ALD growth regime. The QMS results are corroborated with 5 ex-situ runs.[56].. 50

Figure 24 – Mass-16 (CH_4^+) QMS spectra over eight consecutive ALD cycles. The higher peaks correspond to TMA pulses, the smaller to water................................. 53

Figure 25 – QMS mass-16 (CH_4) integrated during water half cycles. 20 cycles were run at 5 TMA doses under a fixed 4.9 µmol water dose... 54

Figure 26 – QMS mass-16 averaged over 10 cycles (Figure 25) as a function of a) TMA dose (fixed H_2O dose at 4.9 µmol) and b) H_2O dose (fixed TMA dose at 4.5 µmol)... 54

Figure 27 - Averaged integrated mass-18 during H_2O dose. Mass 18 was integrated over H_2O half-cycle period. 55

Figure 28 - QMS data for mass-16 (CH_4) integrated over H_2O half cycle periods and averaged over 10 cycles at different TMA and water doses...................................... 56

Figure 29 – Schematic of ALD regimes based on growth per cycle vs. reactant exposure: a) "ideal" ALD process with saturating self-limited growth, b) non- ideally saturating growth. 56

Figure 30 – Correlation between film thickness uniformity across 100 mm wafer and downstream QMS sensing. a) thickness profiles for four Al_2O_3 ALD runs at varying

TMA doses and a fixed 6.5 μmol dose of water. b) in-situ QMS data for mass-16, integrated over water half cycles and averaged over the whole run (left scale), and ex-situ thickness non-uniformity (right scale) as a function of TMA doses.................... 60

Figure 31 – QMS mass-16 integrated over water half cycle vs. cycle number for Al_2O_3 ALD runs at 3.2 μmol TMA and 6.5 μmol H_2O exposures over 3 Si wafers: untreated, HF-cleaned last, HF-cleaned and DI water rinsed last.............................. 61

Figure 32 – Film thickness measured by ellipsometry for 4 ALD runs at 275˚C with varying number of cycles. Linear regression confirms the absence of nucleation-induced growth delay.. 61

Figure 33 – Integrated QMS data (mass-16) for 3 runs at 200, 250 and 300˚C. 62

Figure 34. Across-wafer thickness profiles for five water doses with fixed TMA dose (6.3μmol). 68

Figure 35. Across-wafer thickness profiles for fixed water dose (3.9 μmol) and varying TMA doses. The data were split in 2 graphs for clarity (a) emphasis for TMA doses close to saturation (b) emphasis for TMA dose in under-exposure regime..... 70

Figure 36. Uniformity for under-dose conditions of TMA (0.31 μmol) and water. (a) Thickness profiles show improved uniformity, though deposition rates are lowered and ALD uniformity is not achieved. (b) Area-averaged deposition rate as a function of r=water/TMA dose ratio. Height of vertical bars indicates extremes of deposition non-uniformity on the wafer. 72

Figure 37. Across-wafer uniformity for over-dosed water (4.86 μmol) and under-dosed TMA (0.3 μmol), with varying duration of purge cycle after water dose. Purge time after TMA dose = 20 s. 74

Figure 38 - Across-wafer thickness profiles for 8 ozone doses with fixed TMA dose (1.6 µmol). 76

Figure 39 - Across-wafer thickness profiles for 12 TMA doses with fixed ozone dose (3.2 µmol). 76

Figure 40 – Schematic contour map of across-wafer non-uniformity as a function of TMA and water doses, obtained from thickness profiles in this work. 78

Figure 41 – Al_2O_3 film characteristics for H_2O and O_3 based chemistries as a function of TMA exposure: a) across wafer non-uniformity (measured as 1σ/mean); b) corresponding deposition rate averaged over 9 measurements.................................. 82

Figure 42 – Electrical characteristics measured over 30 capacitors for 238Å Al_2O_3 film deposited under saturating TMA and water conditions. (a) Capacitance vs. voltage (b) current density vs. applied field... 87

Figure 43 – Electrical characteristics of Au/Al_2O_3/Si MOS capacitors measured across the wafer along the direction of the flow. Film deposited in underdosed water conditions a) CV characteristics at 100 kHz b) IV characteristics for 0 to -5V voltage sweep... 88

Figure 44 – Thickness, capacitance, permittivity and current density at -1MV/cm as a function of position across wafer for Al_2O_3 film deposited in water-starved conditions. Permittivity calculated with 10Å SiO_2 interfacial layer included (solid triangle) or excluded (open triangles). 89

Figure 45 - Properties of two Al_2O_3 films deposited over 600 cycles under fixed TMA underdosed conditions (0.33µmol) and 2.65 µmol (solid squares) and 0.81 µmol (open triangles) water doses 90

Figure 46 – Dynamic SIMS measurements for sample B and C at 5 positions across the wafer. ^{27}Al, ^{16}O and ^{28}Si species are measured.. 93

Figure 47 - SIMS measurements of carbon concentration as a function of depth a 5 locations across sample B. 94

Figure 48 –O (1s) to Al (2p) ratios obtained by XPS for 7 points across the wafer for sample A, B and C. Inset histogram shows the means and ±1σ bars for the 3 samples. 95

Figure 49 – XPS spectra for samples A, B and C measured at 7 locations across the wafer. First row corresponds to O(1s) peak and second row to Al(2p) peak. 95

Chapter 1: Introduction

1.1 - Background on Atomic Layer Deposition

ALD is a gas phase process for synthesizing thin solid films by sequentially exposing a substrate to 2 or more gas reactants. It is widely accepted that high quality films with thickness control at the atomic level (Fig. 1), excellent thickness uniformity and conformality (Fig.2) can be produced by Atomic Layer Deposition.[1-3] In addition, precise control of the film composition in multi-component systems allows engineering the physical and electronic film properties in nanolaminate and alloy structures. (Fig.3) These key attributes are inherent to the self-limited nature of ALD reactions where reactants are sequentially pulsed to initiate saturated chemisorbed surface reactions in order to achieve growth, one (sub)monolayer at a time .

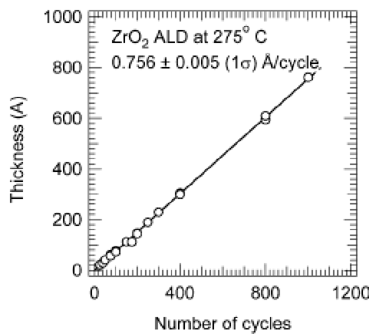

Figure 1 – Linear correlation between cycle number and deposited thickness in ZrO_2 ALD at 275˚C. [4]

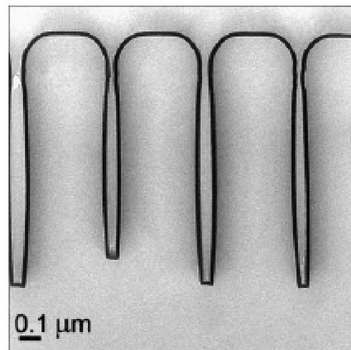

Figure 2 – TEM image of 210 Å hafnium aluminate film deposited by ALD into high aspect ratio SiO_2 features. [4]

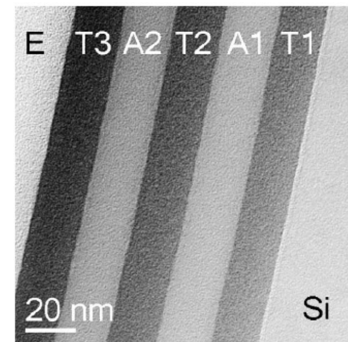

Figure 3 – Example of nanolaminate TiO_2 / Al_2O_3 ALD nanolaminate.[5]

ALD was first developed in Finland in the mid 70's for ZnS epitaxial film growth to be used in electroluminescent flat panel display (and was therefore called atomic layer epitaxy at the time).[6] It initially received limited attention as it could not fulfill the stringent standards for throughput that are critical in semiconductor manufacturing.[4] The current renewed interest in ALD, as illustrated in Figure 4 by the sharp increase of yearly publications, stems primarily from the drive by the semiconductor industry in scaling down feature size of logic and memory devices while increasing aspect ratio and complexity. Since 1995, the International Technology Roadmap for Semiconductors (ITRS)[7] had clearly indicated that the continued transistor downscaling predicted by Moore's law would require new processes and materials with higher permittivity to replace the ubiquitous SiO_2 gate dielectric in MOSFET[1] devices. With a permittivity of 3.7, the physical oxide thickness of SiO_2-based gate dielectrics were predicted to measure less than 4 atomic layers (<1 nm) at the 0.45 nm technology node (implemented in 2009) which would result in leakage currents in excess of 1A/cm^2 at 1MV/cm and cause unacceptable power dissipation.[8]

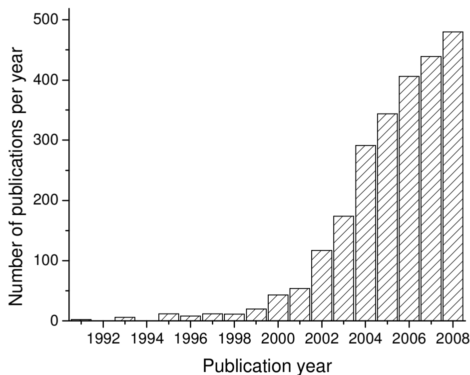

Figure 4 – Yearly publications related to ALD. Based on online search in ISI Web of Science, (Sept. 2009)

---

[1] Metal Oxide Semiconductor Field Effect Transistor (MOSFET)

Conventional deposition methods used in manufacturing, primarily CVD and thermal oxidation, were also becoming inadequate to control the thicknesses of such thin films.

Due to its ability for unprecedented thickness control, ALD has emerged over the past 10 years as a key enabling technology, resulting with the introduction of the first ALD-based sub-nm HfO_2 dielectric in volume production at Intel in 2006.[9] Memory manufacturers have also taken advantage of ALD excellent conformality to deposit metal-insulator-metal (MIM) stacks films in high aspect ratio DRAM[2] structures.[10]

With the technology becoming more mature, the range of applications has expanded far beyond the field of conventional CMOS[3] logic and memory devices, and is now permeating fields as varied as optoelectronics[2], microelectromechanical systems (MEMS)[11-15], energy storage [16], or catalysis[17, 18] to cite a few. ALD has become a key enabler in the field of nanotechnology where complex 3 dimensional structures can be filled or coated to produce nano-particles[18-20], nano-tubes[16, 21, 22] and nano-wires[23-27].

To support the rapidly expanding field of applications, a broad selection of precursors suitable for ALD has also been developed in the last few years by chemical supplier [3, 28, 29] allowing for the deposition of a wide variety of oxide, nitride, semiconductor and elemental materials (Table 1).

---

[2] Dynamic Random Access Memory (DRAM)

[3] Complementary Metal-Oxide-Semiconductor (CMOS)

Oxides	Nitrides	Sulfides	Semiconductors	Elements
Al_2O_3 [11, 20-22, 30-40]	TiN	SrS	GaAs	Si
In_2O_3	NbN	CaS	Si	Ge
ZrO_2	TaN	BaS	InAs	Cu
HfO_2	Ta_3N_5		InP	Mo
Ta_2O_5	MoN		GaP	W
SiO_2	WN		InGaP	Ta
TiO_2	BN			Ti
SnO_2				Pt
Nb_2O_5				Ru
ZnO				Ni
RuO				

Table 1 – Short list of materials deposited by ALD.[41] Puurunen listed more than 75 elements and 125 compounds that could be deposited by ALD in its 2005 review.[3]

1.2 - Details of ALD process sequence

Similarly to CVD, ALD is based on chemisorbed surface reactions where adsorbate species will form strong chemical bonds with atoms on the surface[4]. While in CVD the precursors are flown simultaneously, the precursors are pulsed sequentially in ALD to initiate self-limited chemical reactions so that for each reactant exposure only one (or less than one) monolayer will chemisorb. To illustrate

[4] Chemisorption, i.e., chemical adsorption, is to be distinguished from physisorption, i.e., physical adsorption. Chemisorption involves a chemical reaction between the adsorbing molecules and the surface with the formation of strong chemical bonds. Physisorption originates from weak Van der Waals interactions where minimal changes occur in the structure of the adsorbing molecule. Physisorption can occur over multiple layers as the interaction is not specific to surface-molecule interactions. For water used as a precursor, an intermediate hydrogen bonding configuration (between hydrogen from one water molecule and oxygen from a neighboring one) is also a possibility, directly relevant to the interpretation of results presented here.

the basic concept of the ALD process cycle, we can consider the prototypical example of the Al_2O_3 deposition resulting from the sequential exposures of the metal precursor trimethylaluminum $Al(CH_3)_3$ (TMA) and water. During the first $Al(CH_3)_3$ exposure, the molecules will adsorb on the active ligands present on the surface, in this case hydroxyl –OH^* groups. A thermally activated reaction will occur where the $Al(CH_3)_3$

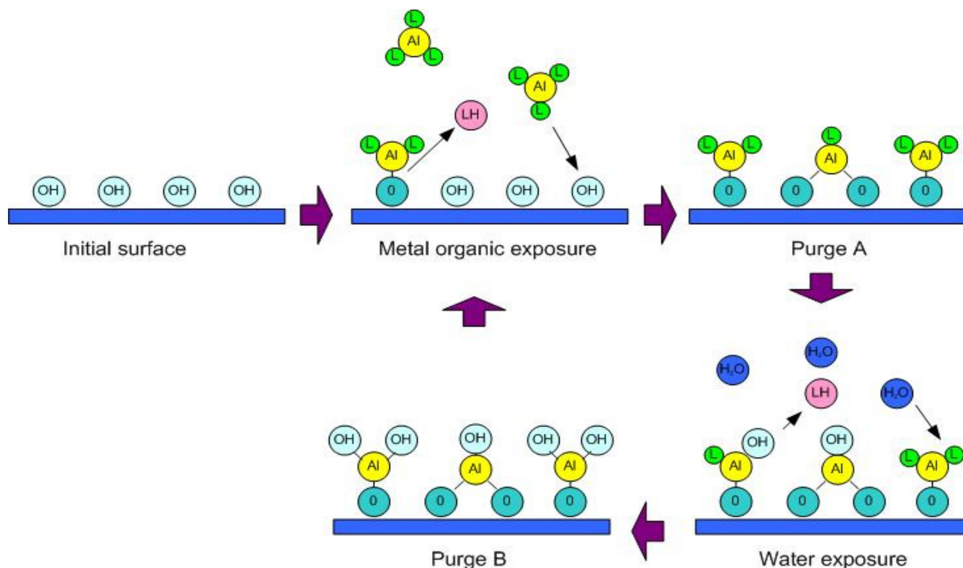

Figure 5 –Sequence of alternating reactant exposures and purges during one Al_2O_3 ALD cycle with TMA and water. In this specific case, the reaction by-product is the same for both half reactions, i.e., methane CH_4.

molecules are split on the surface. The CH_3 ligands combine with hydroxyl surface groups to form a volatile compound, i.e., methane CH_4, that will desorb from the surface. The remaining part of the molecule chemisorbs to the surface to chemically bound aluminum atoms to oxygen. This type of reaction is referred to as a ligand-exchange reaction. It should be noted that the $Al(CH_3)_3$ molecule can react with either one or two hydroxyl groups in order to achieve the stoichiometric Al_2O_3. This

first “half” reaction stops when all the hydroxyl active sites that are physically accessible by the larger $Al(CH_3)_3$ molecules have been reacted.

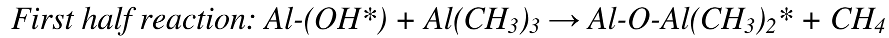

First half reaction: $Al\text{-}(OH^*) + Al(CH_3)_3 \rightarrow Al\text{-}O\text{-}Al(CH_3)_2^* + CH_4$

where the asterisks denotes the active surface species [36, 42]

Excess TMA molecules as well as desorbed reaction by-products are purged out of the reactor and the surface is left chemically complementary to the 2nd precursor, in this case water. Similarly water will bind to the methyl groups via another ligand-exchange reaction causing the release of the remaining methyl bonds as CH_4 molecules.

Second half reaction: $Al\text{-}O\text{-}Al(CH_3)_2^* + H_2O \rightarrow Al\text{-}OH^* + CH_4$

The essential aspect of ALD is that after completion of the 2 half reactions, the surface is once again reactive to TMA and therefore a new layer can be deposited by repeating the same sequence. This sequence of 4 steps constitutes a reaction cycle which adds a fixed amount of material to the surface, referred to as the growth per cycle (GPC). It must be noticed that in most processes the GPC is less than one monolayer. This is a direct consequence of steric hindrance as the methyl ligands from the chemisorbed $Al(CH_3)_2^*$ species shield part of the surface from being accessible the TMA molecules. In the case of Al_2O_3, the growth rate is ~ 0.1 nm/cycle or less than half the atomic spacing.

It should be noted that the $Al(CH_3)_3$ / H_2O process is considered “ideal” for ALD as the reactants are highly reactive but at the same time thermally stable, and the

gaseous byproduct, methane, does not interfere with the growth. Nevertheless, even in this "ideal" case, complex surface reactions can occur in parallel with the ligand exchange reactions described above. For example, $Al(CH_3)_3$ can react dissociatively with coordinatively unsaturated (c.u.s.) Al-O pairs of alumina to produce Al-$(CH_3)^*$ and O-$(CH_3)_2^*$ surface species. [3, 42] Hydroxyl groups can also recombine to form a water molecule. This temperature-induced dehydroxylation can significantly impact the surface OH concentration and therefore the GPC.

1.3 - Process requirements to achieve self-terminated ALD

Self-limited reactions are the foundations for the excellent characteristics of films deposited by ALD. However a number of factors, often interdependent with one another, can impact the performances of the process. The following section offers an overview of some of the key requirements and challenges found at the process level.

1.3.1 Precursors

In order to achieve ALD, the chemical precursor must fulfill a number of requirements. (1) Their volatility must be high enough (at least above 0.1 Torr) so that they can be easily transported in gas phase to the reaction zone. Gases and high vapor pressure liquids are preferable. However a majority of the ALD precursors are low vapor liquids or even solids at room temperature and will therefore require heating to raise their vapor pressure. (2) Precursors must exhibit a good thermal stability and not decompose either in the source or on the substrate. Decomposition

Table 2 – Key precursor requirements [43]
Volatility
Aggressive and complete reactions
No-self decomposition
No etching of the film or substrate
No dissolution into film or substrate
Sufficient purity
Non-reactive volatile byproducts
Inexpensive
Nontoxic
Easy to synthesize

reactions are likely to induce non self-limited reactions and higher GPC as well as film contamination from the incorporation of C, N, H or halide atoms depending on the precursor. Metal organic compounds start usually decomposing around 300-350˚C limiting the temperature process window. (3) To achieve self-terminated reactions, the precursor must react aggressively and completely with the species left on the surface during the previous exposure and not react with its own adsorbates.

1.3.2 Sample preparation

The ALD process being based on surface reactions, initial surface conditions sensitively affect the ALD film. Like in chemical and physical vapor deposition (CVD and PVD), a nucleation must occur preliminary to the growth phase. In the nucleation regime, only a fraction of the molecules will actively react on the surface resulting in smaller GPC. Minimizing the nucleation retardation is critical to achieve not only good thickness control at the atomic level but also to minimize the impact of film discontinuities and roughness present in the island growth regime. One of the key benefits of ALD over conventional deposition methods is that such nucleation regime can be extremely short, i.e., 1 or 2 cycles, assuming that the right ligands are uniformly present on the surface. (Figure 6) In less favorable conditions, e.g., hydrogen-terminated surfaces for oxide growth, poor reactivity of the reactants or low

temperature, the nucleation delay can increase significantly to 30-50 cycles or more.[44]

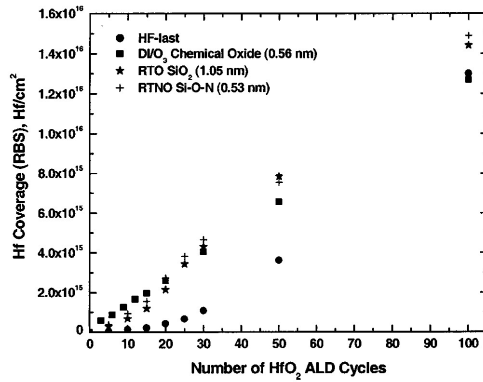

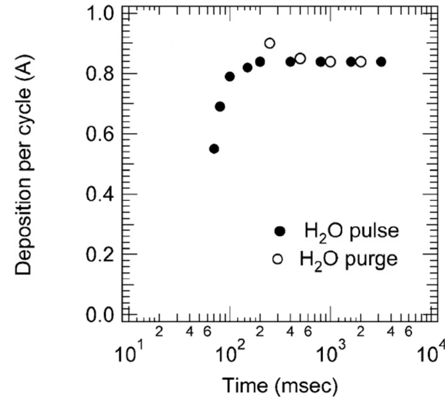

Figure 6 - Nucleation retardation in HfO_2 ALD. Hf surface coverage measured by RBS based on different surface preparations (circles: Hf-last, squares: chemical oxide, stars: rapid thermal oxides, plus: rapid thermal oxinitride). Source: [44]

Figure 7 – Al_2O_3 deposition rate as function of purge time and H_2O exposure time. Saturating self-limited reactions ensure that the deposition rate reaches a plateau once the reactant doses are at or above saturation level. Source: [45]

1.3.3 Saturating exposures

In order to achieve thickness uniformity and conformality across the deposition zone, the precursor exposures must be sufficient to fully saturate the active sites on the surface. Determining the proper saturating dose is usually the first step when optimizing an ALD process. This time consuming procedure is achieved by incrementally increasing the dose of one precursor and measure ex-situ the GPC. Upon dose saturation, the growth rate will reach a plateau corresponding to an “ideal” ALD regime. (Figure 7) In many cases, the dose used will be about 50% higher than

the exact saturating dose. Overdosing the materials will require increased purge times and waste expensive precursor while underdosing will result in thickness non-uniformity and lower GPC.

Depending on the precursors, saturation of the surface in a self-terminated reaction can be limited by steric hindrance of the ligands, the number of reactive sites or the reactant partial pressure (more on this subject in section 1.5).

1.3.4 Purge window

A purge time too short to fully exhaust previous precursor from the reactor will result in an overlap of the precursors (e.g., simultaneous presence of both precursors), allowing the ALD process to transition to a CVD mode. If the overlap occurs prior to the deposition zone, the reactants are likely to be consumed before reaching the substrate, resulting in a lower deposition rate. Alternatively if the temperature is too low, multilayer adsorption may occur in which case the excess of reactant will react with the next precursor resulting in a higher growth rate. (Figure 7, Figure 8a) Polar molecules such as water or ammonia are especially prone to this type of behavior due to weak hydrogen bonding and do require longer purge times. However, too long a purge can result in thermal decomposition of the adsorbed species leading to possible film contamination or composition changes in the films depending if the decomposed molecules remain on the surface and potentially react with the next precursor or if they desorb. (Figure 8a)

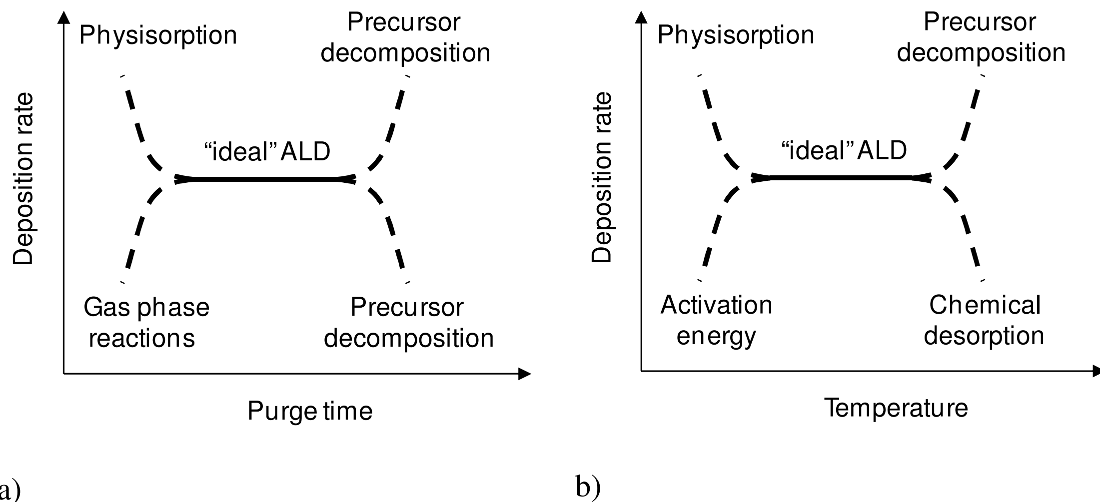

Figure 8 – Process windows showing deposition rate as a function of (a) purge time and (b) process temperature. These figures illustrate potential trends that can be found in ALD, depending on a variety of factors including process chemistries, reactor designs or operational conditions.

1.3.5 Temperature window

Similarly to the purge window, a temperature window can be identified where the ALD deposition rate remains constant. (Figure 8b) Outside this window, low temperature is likely to result in a decreased deposition rate as the reactant cannot overcome the activation energy required for the chemisorption. In some cases, the low temperature may result in precursor physisorption and higher growth rate if the purge is insufficient. High temperature on the other hand may cause precursor decomposition if the precursor exhibits thermal instability [46], or desorption of the adsorbates before they get exposed to the 2nd reactant. The latter case is known to occur with water through dehydroxylation where the adsorbed –OH^* groups recombine at high temperature to form H_2O.[38]

It should be noted that ALD processes have a relatively low thermal budget, a majority of the processes being run below 350˚C. As a consequence, ALD films are typically amorphous. This can be an advantage for dielectric oxides as grain boundaries in crystalline structures provide a preferential pathway for leakage current. However the low temperature may induce residual impurities and defects which can affect device reliability. Post-deposition annealing is therefore often required to achieve device-quality films.

1.4 - Impact of reactor design on film deposition

1.4.1 Cross-flow channel vs. top injection design

Because of its self-terminating nature, ALD is often assumed to be a surface-controlled process where process parameters other than the reactants, substrate and temperature have little impact on the process performances. It is true that GPC, uniformity and conformality, the gold standards of process performance, are not as dependant on flux dynamics as in CVD as long as the saturating exposures are provided. Therefore most reactor designs primarily focus on achieving fast cycle times while ensuring that there is no overlap of reactants which would lead to CVD-type reactions.

To ensure rapid cycling of the gases, most ALD reactors are flow-type systems operating in the 0.1-10 Torr pressure regime. Inert purge gases such as argon or nitrogen are typically used in between pulses since purging is faster than evacuating the reactor. Two different types of reactors can be distinguished

depending on how the precursor flow is directed to the substrate: (1) the flow channel type where reactants flow across the length of the substrate [31, 47, 48] and (2) the top injection type (or showerhead) where the reactant flow is perpendicular to the surface.[4, 49, 50] The flow type systems usually have a smaller volume that leads to shorter residence times of the molecules in the chamber and thus shorter cycle times. As the molecules flow along the narrow channel, they will impinge on the wall multiple times, increasing the probability of finding an open adsorption site and therefore minimizing the exposure and reactant consumption.

Reactant depletion along the flow direction is however a concern if the exposure is insufficient. Also re-adsorption of by-products molecules is more likely to occur as they travel in front of the precursor pulse. Adsorbed by-product molecules will block reactants from potential reaction sites and will affect the uniformity as their concentration increases downstream to the flow.[51] On the other hand, in top injection systems, reactant molecules should impinge the surface at the same time before the byproducts can (possibly) re-adsorb. However by-product re-adsorption is usually limited even in the more prone halide-based chemistry and can be avoided by using the right precursors. Also top injection systems have usually a larger volume to accommodate the shower head and are therefore slower to purge. As a consequence, the simpler and "faster" flow channel reactor design is usually favored.

Because flow-type reactors operate in the 0.1-10 Torr, roots blowers and mechanical rotary pumps rather than high vacuum turbo molecular pumps are typically used on commercial and custom-built tools. The assumption is that purging

with an inert gas is more efficient to remove gas molecules than low base pressure. Use of load-lock systems to minimize the exposure of the chamber walls to air appears mainly limited to manufacturing tools used for the most stringent gate dielectric applications where minor contamination of the film can impact the quality of the device. As water is the most commonly used ALD oxidant, not much effort is made to prevent water moisture to enter the system in the first place (at least for oxide film deposition). Reactor walls are kept at sufficient temperature to minimize the physisorption of the polar water molecules but not so hot that gas desorption could affect the ALD chemistry. As a result, reactor walls are often kept at the same temperature as the wafer.

From a vacuum perspective, requirements for ALD are therefore less stringent than for evaporation and sputtering-based techniques (e-beam or thermal evaporation, molecular beam epitaxy, RF/DC sputtering) where ultra high vacuum conditions are required in order to achieve mean free path larger than the geometrical size of the chamber. Considering that these techniques are also line of sight and result in poor uniformity and conformality, the benefits of ALD can be significant.

1.4.2 Precursor delivery

Achieving accurate and reproducible delivery of minute reactant doses, i.e., a few micromoles per dose, is arguably one of the most challenging aspects of an ALD reactor design. Most of the precursors used for ALD are typically liquids or solids at room temperature. While the vapor pressure of water, a commonly used oxidant, is relatively high, 23 Torr at 25˚C, the vapor pressure of most ALD metalorganic

precursors will range from 10 to as low as <0.01 Torr. Though the vapor pressure exhibits an exponential behavior with temperature, the temperature window is often narrow as most precursors start thermally decomposing at 100-150˚C.[28, 46] Additionally achieving homogeneous temperature distribution to avoid “cold spot” and possible reactant condensation in the delivery line is difficult in a vacuum system that includes many parts of different thermal masses, e.g., valves, filters, orifices, ¼” lines.

For reactant whose vapor pressures can be safely increased above ~1 Torr, e.g., water or $Al(CH_3)_3$, (Appendices, Fig. VI) the exposure can be controlled by simply timing the actuation of a fast-switching ALD valve mounted between the source vessel and the delivery line. This method is commonly used for its simplicity and low cost. The self-termination can be conveniently observed by monitoring the deposition rate as a function of exposure time. A needle valve can also be added to regulate the flow and concentration of the precursor in the reactor. This method however lacks accuracy as the dose is determined by the vapor pressure of the source. The vapor pressure of the source can be affected not only by minor external temperature but also from the endothermic vaporization of the liquid. In addition, it is difficult to quantitatively determine the accurate amount of precursors delivered.

For reactant with a vapor pressure less than ~1 Torr, an inert gas can be bubbled into the source vessel in order to increase the surface exchange between liquid and gas and facilitate the reactant evaporation. However such approach makes it difficult to measure and control accurately the precursor dose being delivered as the

dose will vary not only with the pulse time, inert gas flow rate and temperature but also the geometry of the bubbler and the amount of precursor left in the vessel.

The lack of accuracy of the previous two methods is usually addressed by operating in an over-exposure mode, relying on the self-limited nature of ALD reactions to compensate for small exposure variations.

Liquid injection systems that vaporize liquid are also available though their lack of accuracy to deliver the very small doses needed for ALD, as well as concerns about thermal decomposition of the precursor in the high temperature vaporizer has hampered their use.

As we will see throughout the upcoming work, the type of the delivery system can significantly impact the process performances at the wafer scale. Its design may not only depend on the choice of reactants (and their vapor pressures) but also on the type of applications. For example, the design requirements to deposit a uniform gate dielectric film on a planar wafer with cycle times of less than 1s or so will likely be different than to deposit conformal films in high-aspect ratio and high surface area 3D structure. This issue will be discussed in further details.

1.5 - Impact of reactant partial pressure on adsorption

1.5.1 Examples

Water is the most commonly used oxidant in ALD, primarily because it is inexpensive, inherently safe, with a high vapor pressure (25 Torr at room temperature) and reacts energetically with many metal precursors either halide or

metalorganic-based. Using a commercial cross-flow reactor, Matero and al. investigated in Al_2O_3 ALD the growth rate dependence with the water dose in the $Al(CH_3)_3$ / H_2O process. In this case the water dose was controlled by adjusting the flow rates through a needle valve and regulating the pulse time. As shown in Figure 9, under high and low flow rate conditions, extending the pulse time beyond 2.5s did not yield further increase of the GPC. This suggests that in both cases the reaction were self-terminated. However the growth rate increased by 22% from 0.95 to 1.16 Å/cycle at higher flow rate. Matero and al. reported the same trend with different materials systems including Ta_2O_5, TiO_2, ZrO_2 and the effect of precursor concentration on GPC was also reported by other groups.[52, 53] The purge time did not affect the GPC indicating that the higher growth rate was not due to a CVD-like reaction and the origin of the higher GPC was attributed without further details to a density increase of the hydroxyl groups on the surface upon higher flow rates.

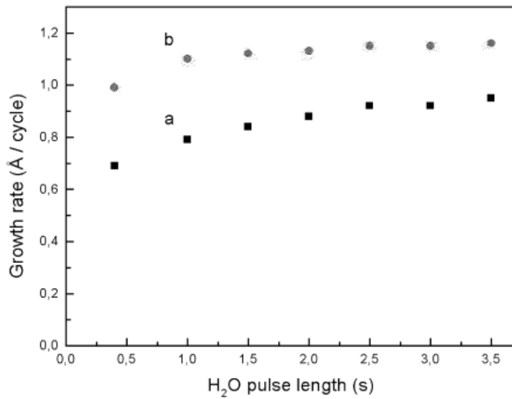

Figure 9 – Dependence of the Al_2O_3 growth rate with the H_2O pulse length at (a) small ($8x10^{-6}$ g/s) and (b) large ($2x10^{-4}$ g/s) water flow rates.[38]

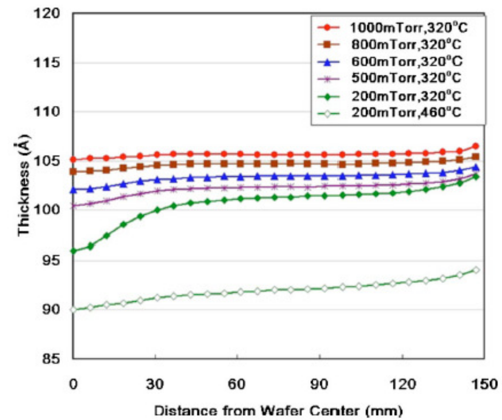

Figure 10 – Thickness profile of Al_2O_3 films as a function of process pressure.[54]

Though the flow rate of water appeared to change the GPC, Matero's results showed that the film composition, density as well as electrical and optical properties remained unchanged at higher water doses. Similarly Li and al. investigated the impact of process pressure on GPC and thickness uniformity in an Al_2O_3 ALD process using $Al(CH_3)_3$ and O_3 in a Genus manufacturing tool for 300 mm diameter wafers.[54] As shown in Figure 10, higher process pressure lead to higher GPC and uniformity and the authors suggested that it was caused by a higher conversion of the surface sites.

1.5.2 Adsorption equilibrium in ALD

These two examples illustrate an important issue of ALD reactions which is not often emphasized, namely that a distinction should be made between self-termination and saturation. The self-terminated nature of ALD is linked to the fact that a reactant in the gas phase can only chemisorb with a complementary active chemical species present on the surface. The fact that this gas reactant cannot react with its own adsorbed species, e.g., $Al(CH_3)_3$ cannot react on CH_3*, guarantees that the reaction will be self-limited. However in all chemisorption processes, the amount of adsorbed material is based on a gas-surface chemical equilibrium that converges toward a constant value when the partial pressure is increased.[55] This means that upon extended pulse time, the reaction doesn't necessarily terminate because of all the active sites have been consumed. Rather reaction saturates when an equilibrium between desorption of additional precursor (beyond the reacted species) and adsorption of further species from the gas phase has been reached at a given

temperature and partial pressure. However, if all surface sites have been converted or are occupied with a chemisorbed species preventing further adsorption (via steric hindrance for example), then increasing the partial pressure will have no effect.

1.6 - Motivation and objectives

While the favorable consequences of the self-limiting, saturative nature of ALD precursor adsorption/saturation is striking, chemisorption processes in general can be complex. This is particularly true for the kinds of precursor species employed in ALD (organometallics, halides, water), inviting deviations from ideal monolayer self-limiting behavior through steric hindrances, complex molecular geometries to satisfy mass balance constraints and resulting crystal structure, subsidiary or parasitic reactions, or weaker interactions involving hydroxyl species. As in other chemical processes, the challenge is thus to identify the parameter regime that constitutes an "ALD process window", i.e., in which the benefits of ALD are realized. Thus, development of ALD processes requires a set of experiments to identify minimum precursor doses that cause saturation of growth rate, demonstrate that higher doses do not alter growth rate, and confirmation that these indicators are validated by across-wafer uniformity and perhaps conformality studies, as well as analysis of the material properties sought (electrical, etc.). It is striking that despite hundreds of publications and other reports, from a variety of industry sources as well as university and government laboratories, few convey a rigorous evaluation of true ALD process windows where superb uniformity and conformality are achieved.

Identifying an ALD process window can be nontrivial, since a variety of factors can have a direct effect on the process outputs - growth rates, uniformity, step coverage, and material quality. Examples of such factors include (but are not limited to): precursor choice, substrate selection and preparation, process parameters (reactant dosage, cycle purge, process temperature or pressure) or reactor designs. Due to the number of variables involved and the interdependency between some of these variables, the procedure to optimize an ALD process for a given chemistry/reactor can prove time consuming, and even more so as we consider a shift towards ternary and quaternary materials systems or the application of ALD to production-size substrates where uniformity requirements present a stringent test for ALD process performance.

To investigate new methodologies aiming at the optimization of ALD process and materials performance, an ALD reactor was designed and implemented. This cross-flow wafer-scale system enables accurate end-point pressure control of reactant exposures in order to achieve spatial distribution of reactant flux across the reactor leading to spatial gradient in thickness and materials properties.

The overall strategy focuses around two concepts: (1) to implement in-situ sensing to rapidly delineate the contours of the ALD process space that lead to saturating self-terminated reactions and uniform monolayer growth; (2) to characterize within that space the film properties across the wafers in order to understand the physicochemical contributions that impact process and materials performances under different reactant exposure regimes.

To achieve the first goal, we implemented in-situ quadrupole mass-spectrometry (QMS) downstream to the ALD reactor. We have previously used this approach as a means for real-time monitoring and thickness metrology in tungsten ALD. [56, 57] By sampling and quantifying reaction product concentrations during individual ALD precursor doses, the progress of the ALD reaction within a dose cycle and from one cycle to another was observed. Time-dependent mass spectrometry signals can therefore be used to reveal the dynamics of surface adsorption, reaction, and saturation within a dose cycle, providing essentially real-time estimation of saturation dose levels needed for each precursor. As such, the QMS approach was used to map out the ALD process space over a wide range of reactant exposures.

Within the QMS-defined region-of-interest, we then investigated the correlations between key process metrics, i.e., reactant exposures and purge times, and film properties at the wafer scale, both extrinsic (GPC, thickness uniformity) and intrinsic (electrical, optical, compositional).

An important aspect of this research is that the ALD processes are to be run in a cross-flow system that mimics larger systems commonly found in manufacturing (further details in Chapter 2). The impact of the spatial distribution of the reactant flux is investigated on 100 mm wafers rather than on chip-size samples as commonly done in academic and small R&D ALD systems.

This work focuses on the prototypical case of Al_2O_3 ALD using $Al(CH_3)_3$ as a metal precursor, and water and ozone as oxidants. Al_2O_3 ALD is considered an “ideal” ALD process as the precursors are highly reactive but at the same time

thermally stable, and the gas reaction byproduct, methane, does not interfere with the growth. The robustness of the Al_2O_3 ALD process in conjunction with good thermal, electrical and mechanical properties of this oxide has resulted in steady interest for this system both in research and manufacturing.[2, 4, 34, 35, 39] However, as mentioned by Puurunen in his extensive review paper[3], despite the broad number of publications and applications related to Al_2O_3 ALD, many physicochemical behaviors that govern Al_2O_3 processes are still not fully understood, particularly at the wafer scale.

Of particular interest is the impact of water dosage on film growth and the dose interactions between TMA and water. Matero and al. showed that higher GPC was achievable at higher water concentrations and attributed this effect to an increased density of hydroxyl groups. Water is the most commonly used ALD oxidant but the impact of water dosage on key process performance metrics such as thickness uniformity has not been established at the wafer scale. Water has long been known in the vacuum technology community for its propensity to multilayer adsorption by hydrogen bonding. In order to better understand the physicochemical contributions of water on film growth, we have compared water- and ozone-based chemistries. Ozone is usually favored in manufacturing as it can result in higher quality films with lower carbon contamination levels since it is more prompt to react with the organic ligands on the surface.[37, 50, 54, 58, 59] Ozone, a non-polar molecule, is also not prone to hydrogen-bonding and follows a different reaction pathway than water.[60] As such, it provides an interesting case for comparison.

1.7 - Organization of the thesis

This thesis consists of five chapters in addition to the first Introduction chapter. The summary of each chapter is given below.

Chapter 2: This chapter reviews experimental setups that were implemented to carry out this research. It focuses primarily on the design and upgrade of the UHV ALD reactor, the integration of an in-situ mass-spectrometer, the construction of an automated CV and IV probe station and the implementation of a new commercial Sopra GES5 spectroscopic ellipsometers.

Chapter 3: This chapter focuses on the use of mass-spectrometry for in-situ process diagnostic and optimization in the case of the Al_2O_3 ALD process using water and TMA. The results build on contributions from prior works in which I was closely involved related to real-time wafer-state metrology in CVD [61-65] and ALD [56, 57] processes. A few key results from the prior ALD study are summarized in the introduction of this chapter. The new data illustrate how in-situ sensing can be used to rapidly determine the exposure conditions that lead to saturation, a requisite for ALD process optimization.

Chapter 4: The impact of reactant exposures on thickness uniformity are investigated within the ALD process window identified in-situ in Chapter 3. The results focuses on the $Al(CH_3)_3$ / H_2O system and the impact of the polar H_2O molecule on the film growth. A comparative study with $Al(CH_3)_3$ / O_3 is also be presented to illustrate how different chemistries can impact process performances at the wafer scale.

Chapter 5: In this chapter, the intrinsic film properties are studied to address their relation to ALD process chemical conditions. The impact of reactant exposure on film composition and contamination is investigated using XPS and dynamic SIMS measurements. IV and CV measurements made on Metal Insulator Semiconductor (MIS) and Metal Insulator Metal (MIM) capacitor structures are presented to evaluate the film electrical properties.

Chapter 6: The thesis is concluded with a summary of the contributions of this research and some thoughts regarding the future works.

Chapter 2: Experimental setup

The following chapter focuses on the tools that had to be implemented in order to carry out the proposed research. The ALD reactor used in this study was the first ALD prototype to be implemented in our research group. It was designed in 2003 and built with the help of Wei Lei, a prior doctoral student[5]. The primary objective of this work was to investigate the use of mass-spectrometry in W ALD processing for in-situ sensing and real-time wafer-state metrology.[56, 57] After completion of this work in 2006, a funded collaboration with equipment supplier MKS Instruments was initiated to investigate new venues for ALD process optimization. The tool was overhauled with donated equipment, including a MKS Vision1000C mass-spectrometer, an O_3mega™ ozone generator and a liquid injection system for low vapor pressure precursors (not used in this work). Additionally a new delivery system was built to accommodate low vapor pressure precursors whose mode of delivery was radically different than those used in the W ALD work[6].

Being able to characterize in-house the films deposited was also essential to evaluate and optimize rapidly the ALD process performances at the wafer scale. An automated probe station was designed and built to measure CV and IV characteristics

[5] Contributions to design and implementation of equipment are listed in Appendices #1

[6] W ALD precursors, tungsten hexafluoride and silane, are both gases above atmospheric pressure at room temperature.

of up to several hundred capacitors on a single wafer. A Sopra GES5 spectroscopic ellipsometer was also acquired to provide maps of thicknesses and optical properties across the wafer on a run-to-run basis.

2.1 - ALD system

2.1.1 Reactor design

A custom-built ALD reactor was used for this study, shown in Figure 11 (detailed drawings in Appendices, Fig. I to IV). This ultra high vacuum system integrates two large 8”-diameter 6-way UHV conflat (CF) chambers used respectively as a loadlock and ALD process chambers. The stainless steel walls of the ALD process chamber are maintained at 150˚C using heating tapes to minimize water physisorption while a Pfeiffer TPU261 TMP with a nominal pumping speed of 260 l/s allows a base pressure below 1E-8 Torr with no gas load. A smaller 50 l/s TMP is used for the loadlock leading to a pressure below 1E-5 Torr within 5 minutes of pump down from atmospheric pressure. The loadlock is essential to rapidly load/unload a wafer without exposing the main process chamber to atmosphere and minimizing potential contamination of the ALD reactor environment and wall memory effects. The relatively large volume of the process chamber, i.e., 16 liters, is inadequate for a fast cycling of reactant gases required for ALD. A smaller mini-reactor was therefore embedded in the UHV process chamber as shown in Figure 11b. The volume of this mini-reactor is only 0.2 liters allowing for rapid gas exchange during ALD exposure and purge cycles. In the sub-torr pressure regime, short residence time of less than

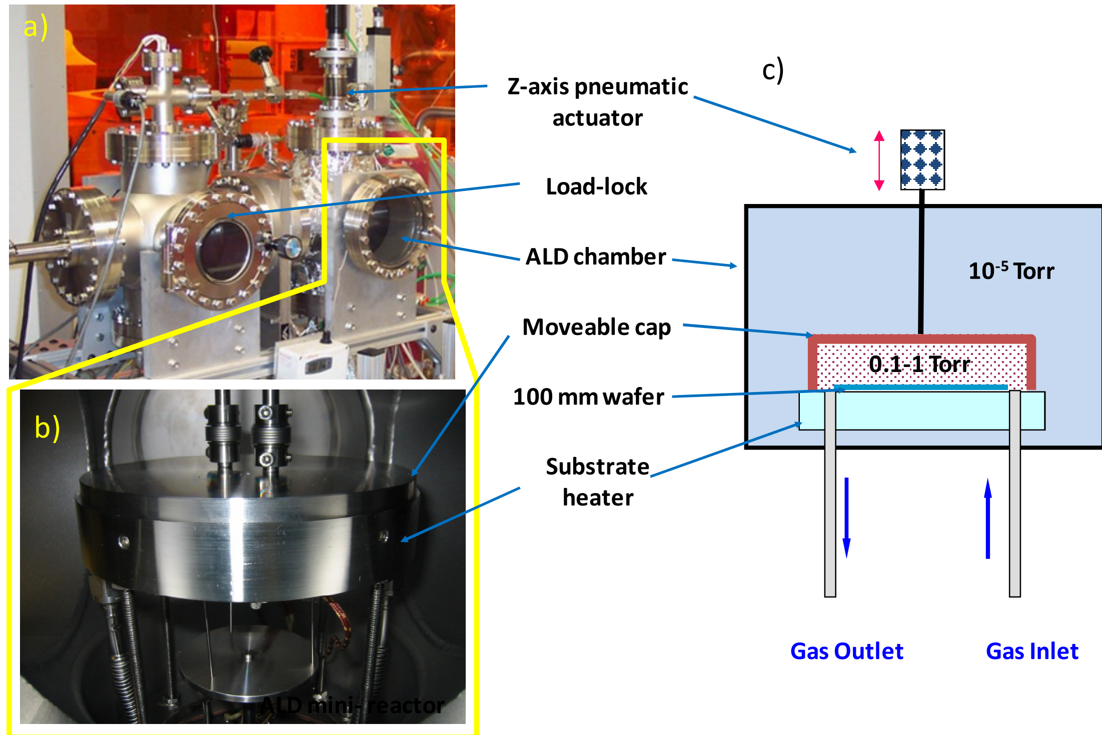

Figure 11 – UHV ALD reactor – a) ALD platform with load-lock and ALD chamber. b) Embedded mini ALD reactor in UHV chamber. c) Schematic of ALD chamber.

one second was estimated. This design also reduces the ratio of wall to wafer surface areas to about 3 to 1. Earlier work showed that such low ratio was essential in achieving in-situ process sensing for wafer-state metrology using mass-spectrometry and minimizing "memory effects" associated with adsorption/desorption from the mini-reactor walls.[56, 57]

The mini-reactor features a stainless cap that is vertically actuated so that a wafer can be transferred from the loadlock onto the substrate heater. In the down position, the cap provides a rough vacuum seal between the mini-reactor and main

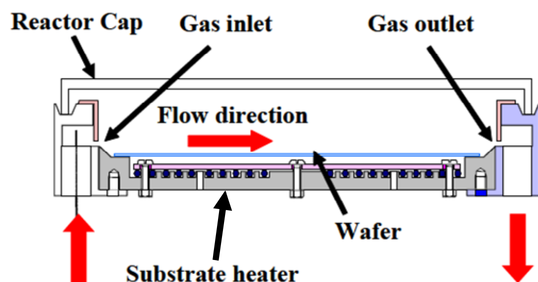

Figure 12 – Cross-section of mini-reactor

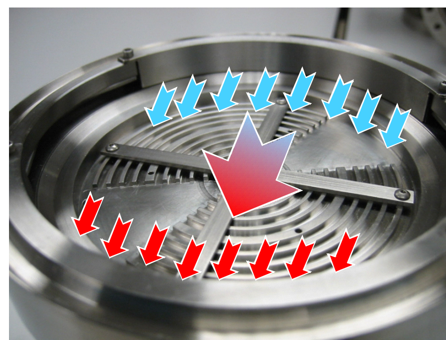

Figure 13 – View of the 100 mm diameter substrate heater with visualization of flows across the wafer.

chamber allowing for a pressure differential respectively from ~0.1-1 to 1E-5-1E-4 Torr under gas load conditions, typically 10 to 100 sccm.

In order to run wafer-scale substrates, i.e., 100 mm diameter wafers, a stainless steel substrate heater was custom-designed and built at the UMD physics shop. (Figure 12) 1/4" diameter gas inlet and outlet lines are integrated directly into the base of the heater. Process gases are introduced and exhausted through two diametrically opposed slits at the upstream and downstream positions of the mini-reactor, each positioned 3 mm above the wafer and measuring 1mm wide by 100 mm long. (Figure 13) The mini-reactor is typically operated at 100 mTorr, the gases being exhausted to a 20 ft^3/min mechanical pump. A MKS capacitance pressure gauge located on the exhaust line provides the pressure reading for the mini-reactor.

The heater temperature is regulated by a proportional integral derivative (PID) control loop based on the feedback of a thermocouple attached on the bottom side of the heater. Based on the reading of a 100-mm 13-point SensArray™ thermocouple

wafer, the temperature non-uniformity at 250 ˚C and 0.1 Torr was measured to be less than 5% across the wafer (based on 1σ/mean). The use of a thermocouple wafer is critical to calibrate the actual substrate temperature vs. the control temperature as pressure will significantly impact the thermal coupling between heater and wafer. (Appendices, Fig. V)) All temperatures indicated in this work will therefore refer to the estimated wafer temperature. It is to be noticed that the mini-reactor is a relatively isothermal environment, the cap being conductively heated via contact with heater. The cap temperature is about 20˚C lower than the heater temperature and is therefore subject to deposition as well.

2.1.2 Gas delivery and reactant dose control

Beside water and ozone (gas) oxidants, trimethylaluminum (TMA) and titanium tetraisopropoxide (TTIP) were used as metal precursors with respective vapor pressure of 11 Torr and 0.04 Torr at 25˚C. Each liquid precursor vessel was heated in order to achieve a desired vapor pressure (see Table 3). Since in the context of this work it is critical to accurately and reproducibly control the doses, a novel approach was used. Reproducible precursor dosage was achieved by implementing a pressure end-point control scheme where each precursor vapor was inlet through a needle valve into a temperature-controlled volume. (Figure 14) Upon reaching a given pressure setpoint, the inlet valve between the precursor source and the volume was closed and the gases released into the chamber for 0.3 s.

Reactant	Water	TMA	TTIP
Vessel temperature [˚C]	25	25	60
Vapor pressure [Torr]	23.1	11.4	0.6

Table 3 – Reactant control temperatures and vapour pressures

By monitoring the minimal and maximal pressures during each cycles, the doses were approximated from the ideal gas law, pV=nRT (where p is the pressure, V the volume, n the amount of substance, R the gas constant and T the absolute temperature). Using a LabView-based software to control the pulse sequence, doses as small as 0.3 μmol were controlled within ±1.5% over the run duration. (Figure 15) After each pulse, the gas remaining between the fill valve and needle valve, whose pressure is typically higher than the setpoint pressure, were dumped via a bypass valve.

It is important to notice that by controlling the dose via end-point pressure control rather than by regulating the exposure time (as seen in Chapter 1.4.2), when a higher dose/pressure setpoint is selected, the reactant partial pressure and concentration of the precursor over the wafer also increase. In other words, this is similar to increasing the flow rate of water as in Matero's example [38] reported in Chapter 1.5.1.

An MKS O_3mega™ ozone generator was also implemented. O_2 (Grade 5 or better, Praxair) flowing at 200 sccm was converted up to 20 wt% ozone (300 g/m^3) in a single electrical discharge cell operating at 20 psig. The high flow and high pressure required for the operation of the O_3mega™ required a different control scheme of the ozone exposure. The O_2/O_3 mixture was flowed continuously into an HA-series catalytic ozone destruct from Ozone Engineering to deactivate ozone into oxygen.(Figure 14) A fraction of the total flow was pulsed into the reactor using a fast action ALD valve. A Swagelok medium flow metering valve was implemented

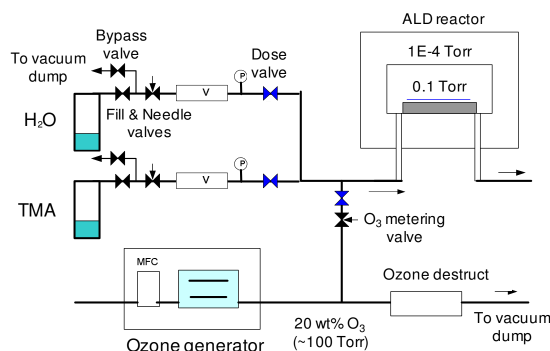

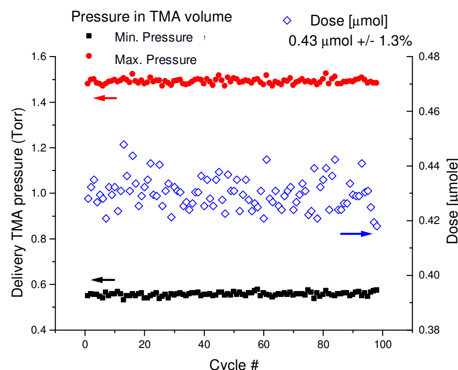

Figure 14 – Schematic of gas delivery setup. TMA and water vapours are introduced in volume V until pressure P is reached prior to release through dose valves.

Figure 15 – Record of maximum and minimum pressures in TMA delivery volume over 100 cycles. Estimated doses (open diamonds) are shown on the right axis.

upstream to the ALD valve to regulate the flow. For a given needle valve conductance, the ozone doses in µmol were estimated by integrating the pressure peaks measured in the mini-reactor for different exposure times and comparing them to integrated peaks from known doses achieved by end-point pressure control in the TMA and water vessels.

2.1.3 Process control

An automated PC-based control platform was implemented to accurately control the valve sequences for precursor exposure and purges. A National Instruments LabView™ program was written to monitor and control the ALD process including the sequencing of the 16 valves for reactant delivery, the reading of the pressure signals in the delivery volumes and reactor as well as the mass-spectrometry signals (detailed in the in-situ sensing section). Recipes loaded from Excel spreadsheets were created to easily define the process setpoints for each precursors at

each cycles as well as to determine the sequence of pulses for each cycle. For example, assuming A, B and C correspond to 3 different precursor pulses, H_2O, TMA and TTIP, possible pulse sequences could be:

$[A-B]^n$ for a 2 component oxides where n defines the number of cycles

$[A-B-A-C]^n$ for an aluminum titanium oxide alloy structure

$[(A-B)^m, (A-C)^n]^p$ for an Al_2O_3 – TiO_2 nanolaminate where m, n define the thickness of each individual oxide layer, and therefore the composition, and p defines the total number of supercycles and therefore the total thickness.

From a hardware perspective, all 16 solenoid-actuated pneumatic valves (Swagelok ALD diaphragm valves, P/N 6LVV-ALD3TFR4-P-C) were driven by a 24V DC signal actuated via a National Instruments external solid-state-relay board (SSR-16 backplane) configured with 16 DC output relay (ODC5) modules. The timing of the valves was controlled by LabView with a 10 ms timing loop increment for optimal accuracy. Analog 0-10V input signals for pressure readings and analog output signal for flow control of carrier gas were handled by a NI-6014 universal data acquisition board. All signals, i.e., valve actuation, pressures, mass-spec sensing, were monitored in real-time providing direct feedback to the user for potential fault diagnostic and proved extremely valuable in troubleshooting and optimizing both tool operation and process.

2.2 - Quadrupole mass spectrometry

2.2.1 Operational principles

Quadrupole mass spectrometry (QMS) is a semi-quantitative microanalytical technique with high sensitivity and chemical selectivity requiring only a few nano-moles of sample to obtain characteristic information regarding the molecular weight and the structure of gas-phase molecules. QMS has been widely implemented as an invaluable analytical tool for process contamination identification, gas purity analysis, vacuum system leak detection, chemical reaction verification, photoresist detection, endpoint detection, tool diagnostics, and preventative maintenance in semiconductor manufacturing.

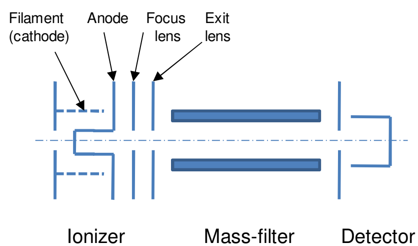

Figure 16 – Schematic of quadrupole mass spectrometer (QMS)

Quadrupole mass spectrometer consists of the ion source (ionizer), the quadrupole mass filter and the ion detector.(Figure 16) Some of the gas molecules are ionized in the ion source and separated by mass/charge ratio in the mass filter. The partial pressures of the respective gases can be determined from the ion current measured in the ion detector.

Inside the ion source, a heated filament emits electrons, which bombard the incoming gas molecules, giving them an electrical charge. The filament usually is made of iridium with either a thorium-oxide or yttrium-oxide coating, which can be turned on in high pressure without undergoing instantaneous combustion. The term

"emission current" refers to the stream of electrons emitted by the heated filament and usually is below several thousand microamperes. The anode is positive with respect to the filament and the potential between the anode and filament, called electron energy, will directly impact the degree of ionization of the molecules. By adjusting the electron energy, ions of the same mass but from different species can be distinguished. The ions exit the ion source through the source exit lens negatively biased with respect to anode. The ion energy characterizes the potential difference between source exit lens and anode.

The mass filter in a quadrupole mass spectrometry consists of 4 cylindrical rods positioned in a square array. The trajectory of the ions will be subject to the electrical field in the mass filter and only those of specific mass/charge ratio will pass through the mass filter and reach the ion detector. A combination of DC and RF voltage is typically used at the two pairs of rods.

The ion detector counts ions passing the mass filter. An Electron Multiplier (EM) is usually coupled to a Faraday Cup (FC) to achieve optimal measurements. The EM which acts as a preamplifier for sensitivity improvement usually is placed before the FC, which measure the electron output current of EM. The EM gain characterizes the ratio of the electron output current to the incident ion current. The drawback for EM is that its gain will degrade after being exposed to high pressure.

Interpretation of mass spectrometry data requires a good understanding of the ionization process that gases undergo within the ion source. At electron energy above 70 eV, dissociation and ionization mechanisms usually occur simultaneously for most

gas molecules. Illustrated below are just a few examples that may occur in the ion source.

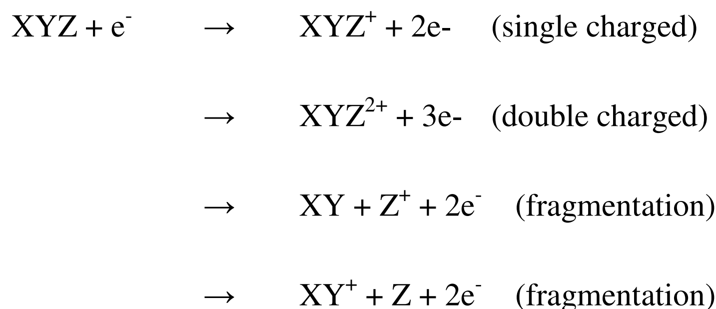

$$XYZ + e^- \rightarrow XYZ^+ + 2e- \quad \text{(single charged)}$$

$$\rightarrow XYZ^{2+} + 3e- \quad \text{(double charged)}$$

$$\rightarrow XY + Z^+ + 2e^- \quad \text{(fragmentation)}$$

$$\rightarrow XY^+ + Z + 2e^- \quad \text{(fragmentation)}$$

Libraries of the fragmentation patterns of the most common species are available and are very helpful in qualitative analysis.

2.2.2 MKS Vision 1000C mass-spectrometer

A Vision 1000C quadrupole mass-spectrometer was donated by MKS Instruments for this study. The sensor features a 300 amu closed ion source. The sampling platform includes a differential pumping setup with a proprietary fast response UniBloc™ inlet system allowing for sampling at both background and process pressure using orifices with carefully selected diameters, i.e., respectively 1 mm for UHV and 50 µm for process conditions (see Fig VIII appendices for UniBloc configuration). The 50 µm orifice allows for a linear QMS response with regard to partial pressure up to 2.5 Torr total pressure. To avoid condensation of the reactants on the walls, the UniBloc and quadrupole are heated to 70˚C.

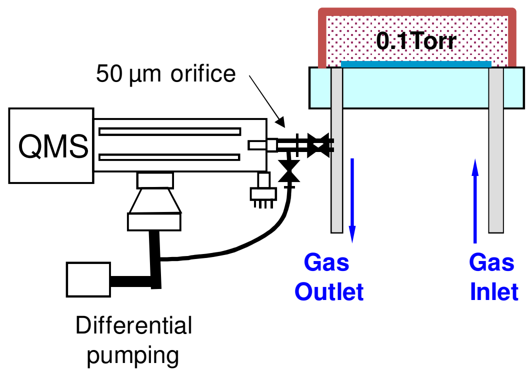

Figure 17 – MKS Vision 1000-C QMS integration downstream to ALD reactor.

\

The Vision 1000-C includes Process Eye 2000, a flexible 32-bit software application operating under Microsoft Windows. To analyze in real-time the QMS data, a Transmission Control Protocol (TCP) link was established between Process Eye and the LabView process control software. Upon request from Labview, Process Eye passes the data as 2 strings, one containing system status, e.g., valve and pump status, the other partial pressures for user-selected masses of interest. The strings are then parsed into LabView and the data plotted and integrated at completion of each half-cycle. In order to reduce the QMS acquisition time, 4 masses were usually monitored at a scanning rate down to 200 ms per spectra.

2.3 - Spectroscopic ellipsometry (SE)

2.3.1 Operational principles

Ellipsometry is one of the key techniques to measure thickness and optical constants as it is fast, non destructive and accurate for films ranging from ~1 to ~10000 nm. In addition it can also be applied to characterize composition, crystallinity, roughness, doping concentration, and other material properties associated with a change in optical response.

Ellipsometry works by directing a linear polarized light to the surface and measuring how much ellipticity was induced from reflection. The measured changes in polarization from the reflected light can be correlated to the thickness of the film as well as its complex refractive index ñ=n+ik where n is the optical index and k the extinction coefficient. The complex dielectric function ε can also be determined where $\tilde{\varepsilon} = \tilde{\varepsilon}_1 + i\tilde{\varepsilon}_2$, with $\varepsilon_1=n^2-k^2$ and $\varepsilon_2=2nk$.

The light source which provides unpolarized light over a broad spectral range, usually from near infra red to UV, is passed through a polarizer to only allow light to pass thru the direction of polarization. The linear polarized light incident on the sample can be decomposed into 2 components: a *s* component for the oscillation contribution perpendicular to the plane of incidence and a *p* component for the contribution parallel to the plane of incidence. Ellipsometry essentially measure how *p*- and *s*-components change in relation with one another upon reflection on the surface. In effect, the complex metric ρ is measured where $\rho = \tan(\psi)\, e^{i\Delta}$. Δ is the phase shift induced by the reflection and $\Delta=\delta_1-\delta_2$ where δ_1 and δ_2 denote the phase difference between the *p*- and *s*-wave respectively before and after the reflection. tan(ψ) corresponds to the ratio of $|R_p|$ over $|R_s|$ where $|R_p|$ and $|R_s|$ are the magnitudes of the amplitude diminution of the *p*- and *s*-waves before and after reflections (also referred to as complex Fresnel reflection coefficients). One of the advantages of ellipsometry is that it measures the ratio or differences of two values as opposed to measuring an absolute value, making this technique highly accurate and reproducible.

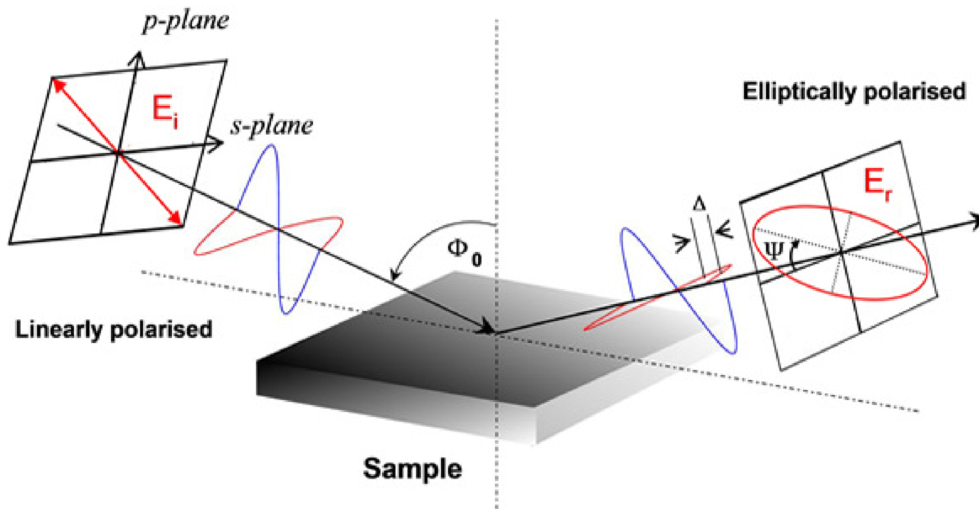

Figure 18 – Ellipsometry measures the change of polarization upon reflection of a linear polarized light on a surface. Upon interference with the film, the reflected light is elliptically polarized. The measured phase change Δ and amplitude change ψ reflect film properties, thickness and refractive index.[66]

The main difficulty with ellipsometry resides in the fact that the film properties are not directly measured (only ψ and Δ are) but instead must be must extracted from models. These models are constructed to describe the samples and allow fitting the data via regression analysis. One must recognize that the refraction index will change for very thin films.[67] As the number of unknown properties increases, so must the amount of information contained in the data. As such, variable angle spectroscopic ellipsometers such as the Sopra GES5 allow investigating complex structure as each wavelength and angle will provide a new set of (n, k) values and corresponding equations.

2.3.2 Sopra GES5 ellipsometer

To allow for rapid film characterization in-house, a Sopra GES5 ellipsometer was acquired. The GES5 is a spectroscopic ellipsometer using a 75W high intensity Xenon arc lamp to obtain a continuous spectrum of light from 1.2 to 6.5 eV (190-1030 nm). The ultra-violet extended range is particularly suited to study high band gap materials. A configuration with a rotating polarizer and a fixed analyzer is used (Figure 19). At location A after the polarizer, the light is linearly polarized and the direction of polarization varies with time. Upon reflection, the light is elliptically polarized and the ellipticity changes with time (as polarizer rotates). The light is again linearly polarized in C but this time its amplitude varies with the relative position of the polarizer with the fixed analyzer. The detector used is a Charge Coupled Device (CCD) adapted to a grating spectrograph. The grating disperses the light on all 1024 pixels simultaneously. A goniometer allows varying the angle of incidence θ from 7° to 90° and 200 mm travel XY stages enables automated wafer mapping. The beam spot size can be reduced from its nominal 1-5 mm dimensions to 365x270 µm using microspot optics.

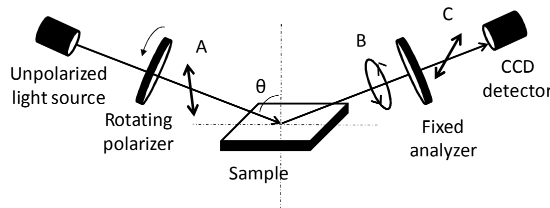

Figure 19 - Configuration of the Sopra GES5 ellipsometer.

2.4 - CV and IV electrical characterization

2.4.1 Operational principles

Electrical properties of Al_2O_3 oxide films are to be measured across the wafer to establish a correlation between process and materials performances over a set of process conditions. The objective is not to achieve an exhaustive characterization of the dielectric performance but instead to focus on two key metrics, capacitance and leakage currents.

Oxide dielectric thin films are characterized by their capacitance C:

Equation 1

$$C = \frac{\varepsilon_0 \varepsilon_r A}{d}$$

where ε_0 is the absolute permittivity, ε_r the relative permittivity of the dielectric (also called dielectric constant and noted K) , A the surface area of capacitor, and d the film thickness.

To a large extent increasing the capacitance C of high-K dielectric has been the main driver for the scaling down of CMOS-based devices allowing for higher drive current between source and drain when used as a gate dielectric in transistor devices. Accordingly to Equation 1, larger capacitance is achieved by decreasing the thickness of the film or increasing the permittivity of the dielectric.

The capacitance can be determined with an LCR meter (inductance (L), capacitance C, resistance R) by measuring the impedance of a device under test (DUT). An AC voltage is applied over the dielectric and the current through the DUT

is measured. LCR determines both the real and imaginary part of the impedance from which the capacitance is extracted. To take into account that the dielectric constant will vary with frequency as a result of different polarization mechanisms in the medium, e.g., ionic or electronic polarization, capacitance values are measured at different frequencies ranging from a few Hz to MHz. In MOS structures, the capacitance is measured as a function of voltage (CV characteristics) and the dielectric constant is determined in the accumulation regime where concentration of the majority carriers in the semiconductor has reached its maximum in response to the applied field across the dielectric.

Another key performance metric of dielectric thin films is the leakage current density at a given electric field (usually 1MV/cm). Leakage current is caused by electron tunneling through the thin oxide layer. For gate dielectric applications, leakage currents are expected to be maintained below 1E-7A/cm^2 at 1MV/cm field and 1E-2A/cm^2 for DRAM applications.[8] Leakage currents are measured by sweeping a DC voltage (V) across the capacitor and measuring the current (I). The current density J is determined from the ratio of the measured current over the capacitor area. Due to the small current density involved, high precision parametric analyzers are required.

2.4.2 Automated probe station for electrical characterization

In order to map the electrical characteristics at the wafer scale, an automated probe station was implemented. 2 Newport ILS 150 motorized stages with 150 mm

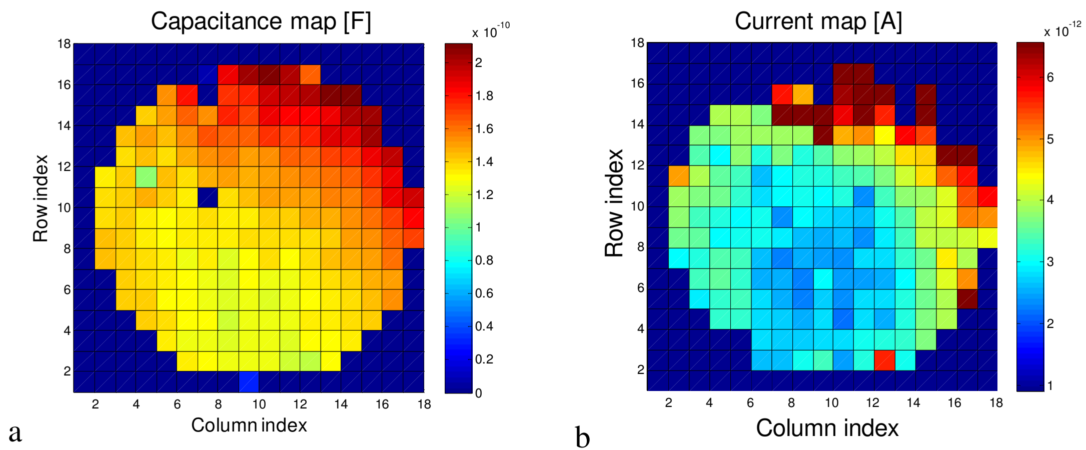

Figure 20 – Matlab renditions of electrical properties for 15 nm Al_2O_3 film deposited under underdosed water conditions. CV/IV characteristics measured over 190 Au / Al_2O_3 / Si capacitors. a) Capacitance map based on measurement at 10kHz and -2V. b) Leakage current map. Current determined at -1MV/cm field. Flow direction is along vertical axis from bottom to top.

travel and 0.5 μm resolution are used for x and y translation of the sample. A Newport 850G actuator with 50 mm travel is used to lower the probe onto the capacitor. A LabView application was written for motion control and data acquisition. IEEE-488 GPIB (General Purpose Interface Bus) connections and LabView VISA commands were used for communication and data transfer. (User interface shown in Appendices, Fig. IX) CV measurements were executed on an Agilent E4980A LCR precision meter using a 0.1V amplitude AC voltage signal over 20 Hz to 1MHz frequency range. IV characteristics were performed on an HP4145 parametric analyzer. Flexible 0.005" diameter tungsten tips (Micromanipulator 7S model) were used. Full wafer maps can be achieved by automatically probing several hundred capacitor structures. (Figure 20)

2.4.3 *MOS and MIM capacitor fabrication*

The CV and IV characterization of dielectric films were achieved on MOS- and MIM-type capacitor structures fabricated in the cleanroom of the Nanocenter FabLab at the University of Maryland. (Figure 21) Several fabrication methods were investigated using different patterning techniques (shadow mask, lithography/wet etch, lithography/lift-off), different metallization methods (thermal and e-beam evaporation, DC sputtering) or electrode materials (aluminum, gold, platinum). The combination of thermal evaporation with use of a stainless steel shadow mask was the most straightforward and economic approach. However, shadowing effects resulting from the curving of the 0.2 mm thick mask and lack of resolution for dots smaller than 0.5 mm diameter lead to inaccurate capacitor areas. An approach based on UV photolithography was favored using the Fablab Oriel 87436 or EVG 620 mask aligners. Devices built using a lift-off based process rather than wet chemical etching showed up to 30% higher permittivity, indicating a possible reaction of the oxide film with the wet Transene etchants (TFA-type for gold and D-type for aluminum). (Appendices, Fig. X)

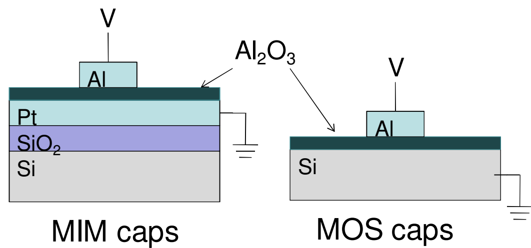

Figure 21 – Schematics of metal-insulator-metal (MIM) and metal-oxide-semiconductor (MOS) capacitors.

An operating procedure using AZ® 5214E photoresist was developed to achieve image reversal with negative wall profiles which are suitable for releasing the

photoresist and metal layers during the lift-off sequence . (Appendices XI) A standardized 5” diameter chrome photomask on soda-lime glass (0.1 µm spot size) was designed and fabricated by Microtronics Inc. (Appendices Fig. XII). It includes 816 sets of features with 3 capacitor shapes (circular, square, crenel) and 4 surface areas corresponding to 0.5, 0.25, 0.1 and 0.05 mm diameter caps. Aluminum capacitor performances were noticed to degrade over several weeks in storage likely due to an oxidation of the metal surface. As a result gold capacitors deposited by thermal evaporation were ultimately favored over aluminum.

Chapter 3: In-situ process optimization using mass-spectrometry

3.1 - Introduction

As with any deposition technique, determining an appropriate process window of parameters for which specified characteristics are achieved is a critical first step when optimizing a new ALD process. This is usually accomplished by a limited number of deposition experiments combined with post-process thickness and uniformity measurements. In the case of ALD, an effective regime is typically indicated by a process parameter regime in which constant thickness per ALD cycle is obtained within a precursor dose range. In some cases this is confirmed by wafer-scale measurements of across-wafer uniformity. This approach based on ex-situ film characterization can prove excessively time consuming. As we have seen in Chapter 1, the ALD process space includes many parameters that can impact the GPC. Even when limiting ourselves to the most obvious ones, reactant exposures, purge times and temperature, the task of finding an optimal set of conditions can take several dozen runs. The problem becomes even more challenging when dealing with chemistries that exhibit substantial nucleation retardation behavior or when depositing multi-component films such as ternaries and quaternaries.

In order to address some of these challenges, we used downstream quadrupole mass spectroscopy (QMS) to infer process behavior from reaction products and reactant depletion and delineate the contour of the ALD process space. The ability to

identify saturation conditions as a function of reactant exposure by this method provides an avenue to more rapid determination of ALD process regimes, since multiple dose recipes can be investigated on a single wafer, without having to remove it and make post-process measurements.

3.2 - Review of in-situ sensing methodologies used in ALD

A number of in-situ characterization methods have been applied to study the process chemistry and reaction mechanisms in ALD processes. It should be noticed that in general in-situ sensing is challenging in ALD due to the relatively high pressure regime (0.1-10 Torr), the transient nature of the flow where gases are rapidly pulsed in and out and the minimized volume of most ALD reactors to achieve short residence time which physically impedes sensor integration.

Quartz crystal microbalance (QCM) is widely used in line-of-sight PVD technique at room temperature to monitor growth rate and thickness in in-situ and real-time. QCM is also used in ALD for process diagnostic.[31, 39, 68, 69] It is sensitive enough to detect mass variations caused by adsorption/desorption reactions during a single ALD half-cycle via measurement of the resonant frequency of a quartz crystal. QCMs are reliable sensors to monitor film growth in situ and as such have been used successfully as a process optimization tool to determine the exposure and purge times leading to saturating and self-limited growth.[31]

QCMs however are fundamentally limited in several ways. (1) Due the temperature dependence of ALD growth, the sensor must be maintained at the same temperature as the substrate which mostly limits its use to isothermal furnace systems. QCMs are

difficult to implement in substrate heating ALD reactors usually found in manufacturing environment. (2) QCM measurements are sensitive to temperature, pressure variations, gas flow velocity and film stress.[31, 70] (3) QCM measures the mass change on gold-coated quartz and film deposition may differ between the wafer and sensor because surface status is initially different, especially during the nucleation phase. (4) Due to the absence of chemical-selectivity, QCMs can only provide limited information related to the chemistry. The overall mass changes during each half reaction can be measured and correlated to a stoichiometric mass balance as long as the chemistry of that reaction has been determined via other venues. [39, 69]

Among in-situ techniques that measure the film directly on the wafer surface, spectroscopic ellipsometry is the most widely studied and is now offered as a characterization method on commercial and R&D tools. [71-73] In-situ SE has been shown to produce accurate measurements of growth rate and has been successfully used to determine the onset of ALD saturation with exposure and to study initial film growth during nucleation. Additionally optical properties such as refractive index and optical bandgap can be retrieved as well as information about the film crystallinity.[72] However as mentioned in Chapter I, the validity and accuracy of the information extracted from the measurement of the optical parameters Ψ and Δ depend critically on the quality of the modeling. This is particularly true in the case of very thin films (<10 nm) where thickness and optical constants are often correlated. For such thin films, SE results must be corroborated with other

measurements techniques.[74] From a hardware implementation perspective, SE benefits from not being directly affected by the ALD flow regime, pressure or temperature. However in-situ SE requires an optical access on the reactor and deposition of optically flat substrates that allow the reflection of the incident light. Such requirements not only seriously limit the type of reactor on which SE can be integrated but also the type of substrate/materials that can be probed.

Other in-situ diagnostic methods, which employs optical, surface analytical, and electrical measurements, can also be used in-situ in ALD processing, including Fourier transform infrared (FTIR) spectroscopy[42, 60, 75, 76], Auger electron spectroscopy (AES)[33], X-ray photoelectron spectroscopy (XPS)[77, 78] or low and medium energy ion scattering (LEIS/MEIS)[79]. Though these techniques can provide very detailed physicochemical information about chemical bonding, atomic composition, microstructure, thickness or nucleation, they have been limited to a research context, due to their cost, integration and operational complexity.

Quadrupole mass spectrometry (QMS) is a very sensitive sensing technique which can provide quantitative and chemically-specific information about gas molecules present at very low concentration (down to 200 ppb or 2E-11 Torr partial pressure)[7]. QMS benefits from being a non intrusive technique as gases can be sampled downstream to the reactor without interference with the process. QMS has

[7] Technical specifications for MKS Vision 1000C QMS.

been extensively implemented in semiconductor manufacturing mainly for fault detection, process diagnostic and end-point process control in CVD[64, 80] and plasma etching[81, 82]. By measuring reactant depletion and by-product generations in CVD, real time film thickness metrology using QMS has been demonstrated.[63, 64, 80, 83]

Its implementation in ALD seems at this point more limited, maybe because of the perception that the self-limited nature of ALD warrants excellent thickness control and therefore limits its potential benefits. Also QMS integration on ALD processes add extra challenges over steady state processes such as CVD: (1) the transient nature of ALD pulses and purges which requires fast response times and high scanning rates in order to track accurately the reaction dynamics, (2) the low partial pressure variations induced by solely the desorption of one sub-monolayer, (3) the use of metalorganic precursors whose cracking pattern in the QMS ionizer will have identical signatures as the by-product species to be measured.

Despite these challenges, the process chemistries of a variety of ALD processes have been successfully investigated by QMS including Al_2O_3[39, 60, 69], ZrO_2[84], TiO_2[68], Ta_2O_5 and Nb_2O_5[85], TiN[86], Ru and Pt[87], and W[56, 57, 76]. Beyond using QMS to qualitatively identify the reaction mechanisms, semi-quantitative QMS studies have been reported where saturation conditions based on reactant exposures were detected.[36, 39, 68, 84] However in these studies, all realized in an isothermal tube furnace reactor, QCM measurements were also performed and used as the primary metric to infer the GPC and optimize the process.

Beyond identifying the process chemistry, QMS was used to investigate the impact of process temperature on the reaction by monitoring trends in by-product generation at different temperatures. Also to compensate for the limited byproduct generation inherent to ALD, the total surface area was increased by loading multiple substrates, resulting to a 44x increase in surface area over a 100 mm wafer. Finally, the H_2O oxidant was substituted with D_2O in order to differentiate the actual reaction byproducts from potentially cracking pattern of the initial reactant.

3.3 - Review of prior work in W ALD

In 2003, following a series of publications related to the use of in-situ sensing in CVD for process diagnostic and wafer-state metrology [62-65, 80, 83, 88, 89], Wei Lei and myself started investigating the use of mass-spectrometry in ALD.

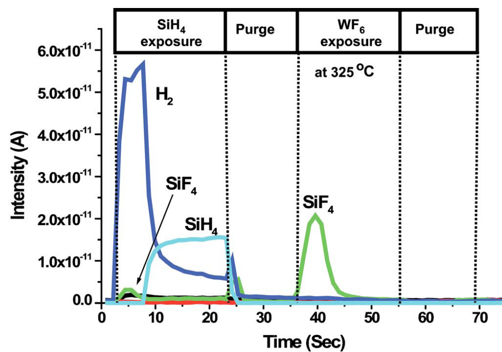

Figure 22 - Mass-spec signals observed during one W ALD cycle. H_2 and SiF_4 by-product generations, occurring respectively during the SiH_4 and WF_6 exposures, clearly reveal the self-limited nature of ALD chemistry. [56]

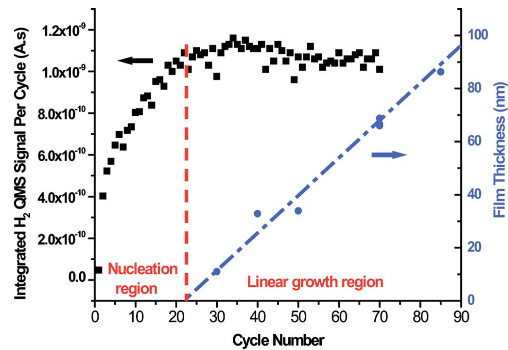

Figure 23 - Integrated SiF_4 mass-spec signals computed as function of respective cycle number. The nucleation regime from cycle 0 to 30 is clearly identified and followed by a plateau indicating a linear ALD growth regime. The QMS results are corroborated with 5 ex-situ runs.[56]

W ALD runs were carried in the UHV ALD reactor at 3 Torr using tungsten hexafluoride and silane. Sampling the gases downstream to the reactor into a differentially pumped 300-amu closed ion source mass-spectrometer, reactant depletion (SiH_4 and WF_6) and by-product generation were monitored in real-time (Figure 22). In this process the self-terminating behavior was clearly characterized as shown by the signature of the hydrogen and silicon tetrafluoride byproducts that decrease a few seconds after the reactants were introduced. ALD reactions being stoichiometric, the amount of reactant by-product generated over time was correlated to the amount of materials deposited on the surface. H_2 and SiF_4 by-product signals were automatically integrated over each half-cycles period (Figure 23). The transition from nucleation to linear growth mode was directly observed in a single run as the integrated signal reached a plateau after about 25 cycles. The validity of the in-situ diagnostic was corroborated by ex-situ film thickness measurements after 5 runs of different cycle lengths. Additionally, we showed that the integrated mass-spec signals could be summed up over the process length and provide an accurate metric correlated to the total film thickness.

These results were significant as they were obtained without interfering with the process chemistry or the reactor design. They showed that direct observation of surface saturation for each half-cycle enables the optimization of exposure and purge times in order to minimize ALD cycle time, a critical requirement for ALD manufacturability. Second, the QMS sensing provided a means to assess more subtle interactions which occur in ALD, such as imperfect surface saturation caused during

the nucleation regime. Third, real-time QMS sensing, shown to be a useful indicator of the wafer state, e.g., thickness, deposition rate, provides a basis for metrology and process control applications.

The objective of the upcoming work is to build on these foundations and demonstrate that QMS sensing can be used in the case of a new process, Al_2O_3 ALD from TMA and water, in order to identify the reactant exposures leading to surface saturation and to correlate these results with process performances at the wafer scale, i.e., cross-wafer uniformity. A QMS-based mapping over the [TMA dose x water dose] process space is to be implemented to investigate the impact of dose interactions over a wide range of dose conditions from under- to over-exposure.

3.4 - Experimental setup

For this process, trimethylaluminum (TMA) (Epichem, Electronic grade) and deionized (DI) water were used. The transition from W to Al_2O_3 ALD required a significant reconfiguration of the delivery system in order to accommodate for the low vapor pressures of the reactant (detailed in Chapter 2). Reproducible precursor dosage was achieved by implementing a pressure end-point control scheme allowing reproducible delivery doses. Exposures times were set at 500 ms with purge times usually set at 20 s. The process temperature was 275°C unless otherwise specified.

3.5 - QMS-based optimization for reactant exposures

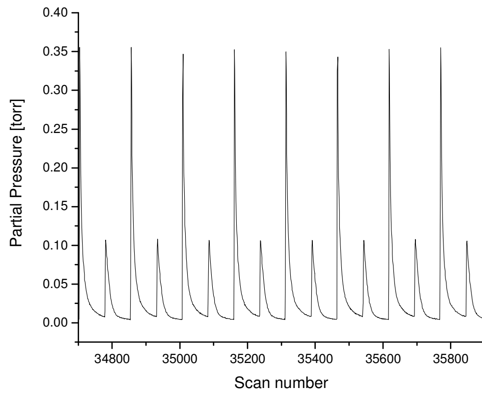

Figure 24 – Mass-16 (CH_4^+) QMS spectra over eight consecutive ALD cycles. The higher peaks correspond to TMA pulses, the smaller to water.

In order to identify the masses that offer the optimal characteristics during the Al_2O_3 process, full surveys from 0 to 300 amu were acquired under various process conditions: TMA pulses only, water pulses only, and consecutive TMA/water pulses to deposit Al_2O_3. The results indicate that mass-16 or CH_4^+ is the main chemical signature during both TMA and water half cycles, in good agreement with literature.[42] Other masses of interest were also identified: mass-17 (OH^+), mass-18 (H_2O^+), mass-57 ($(CH_3)_2Al^+$), mass-72 ($(CH_3)_3Al^+$) though the latter two could only be observed at high TMA doses and usually remained too close to background levels for accurate measurements. Therefore only masses 16, 17 and 18 were tracked with a total scan time of 250 ms. Mass-16 spectrum during 8 consecutive ALD cycles is shown in Figure 24.

In order to identify by mass-spectrometry the TMA and water exposures leading to saturation, an iterative process of varying one precursor dose while keeping the other fixed, then reversing the role, was implemented. A single Si wafer was loaded so that the reactor wall plus wafer surface area would be identical to a regular process. The dose of TMA was raised sequentially from 0.7 to 4.2 μmol with a fixed

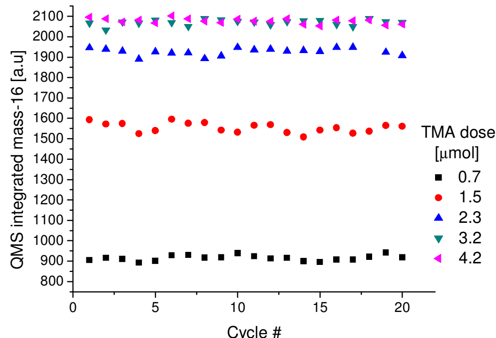

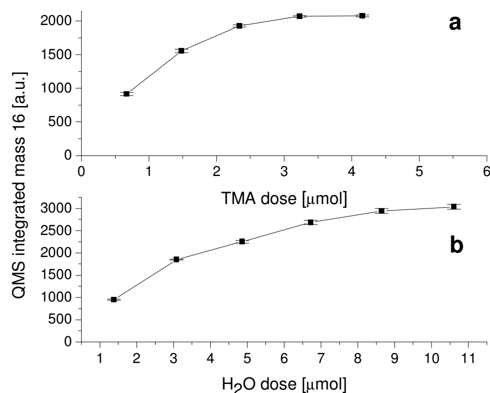

Figure 25 – QMS mass-16 (CH_4) integrated during water half cycles. 20 cycles were run at 5 TMA doses under a fixed 4.9 µmol water dose.

Figure 26 – QMS mass-16 averaged over 10 cycles (Figure 25) as a function of a) TMA dose (fixed H_2O dose at 4.9 µmol) and b) H_2O dose (fixed TMA dose at 4.5 µmol)

4.9 µmol water dose. For each TMA dose, 20 ALD cycles were run.Mass-16 peaks were integrated over each half-cycle period (Figure 25) and averaged over the last 10, discarding the potential transient results from the first 10 cycles caused by the dose change.

The results for TMA dosage in Figure 26a show that the average integrated signal reached a plateau above 3 µmol TMA dose, suggesting that this value may be a suitable saturation dose of TMA. The next experiment was carried out at a fixed 4.5 µmol TMA dose (or 1.5X the QMS-based saturating dose) while varying the water dose from 1.4 to 10.5 µmol. In this case, Figure 26b shows that the integrated mass-16 signal nearly saturates at 10 µmol water dose. The fact that the saturation is not as definitive as a function of water dose is a likely indicator for more complex

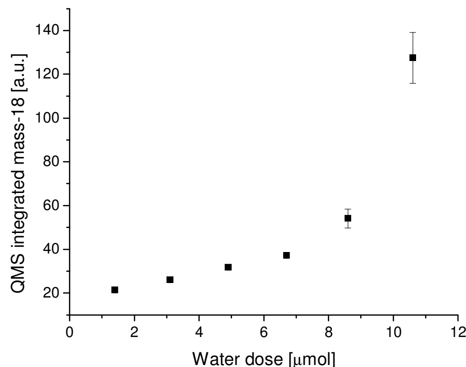

Figure 27 - Averaged integrated mass-18 during H_2O dose. Mass 18 was integrated over H_2O half-cycle period.

adsorption/desorption reactions of water on the surface, which will be discussed in further details. At this point, we take approximate saturation doses for this chemistry and temperature to be 10 μmol water and 3 μmol TMA. Measurements of mass-17 and mass-18 while varying the water dose also indicate a sharp increase of the integrated peaks during the water half-cycle beyond 8.6 μmol. (Figure 27) This suggests that the adsorbed $-Al(CH_3)_2^*$ groups from the previous TMA exposure have been fully converted into hydroxyl groups, resulting in the rapid increase of mass-18 from the excess of water.

3.6 - In-situ exploration of ALD process space

The optimization approach followed during the previous experiments was similar to the one followed in a conventional protocol where one precursor is set at a fixed dose while varying the dose of the other precursor. The in-situ approach however offers the benefits to yield the results within one single run rather than the dozen or so runs that would have been required if ex-situ measurements were undertaken. Both approaches are however limited as they offer at best a cross-sectional view of the multi-dimensional ALD process space. As such, complex

interdependencies between complementary half reactions that are likely to affect the process performances may not be revealed.

A LabView program was therefore written to automatically span the process space by varying both water and TMA doses over the broadest range allowable within the physical constraints of the delivery system. The exposure sequence was programmed as such: the first set was done at a low 1.5 μmol TMA dose and the water dose was incrementally increased from 1.2 to 10.3 μmol every 30 cycles with a 60 s purge time. At completion of this first "two-dimensional cross-section", the tool was left idle for 20 min to help lowering the water background in the system which is likely to build up due to the large excess of water relative to TMA. A second set was then initiated at slightly higher TMA dose and so on. A total of 56 dose conditions (7 TMA doses by 8 water doses) totaling 1680 cycles were explored over a single run. For each cycle, mass-16 peaks were integrated over the half-cycle periods and the results averaged over the last 15 of 30 cycles.

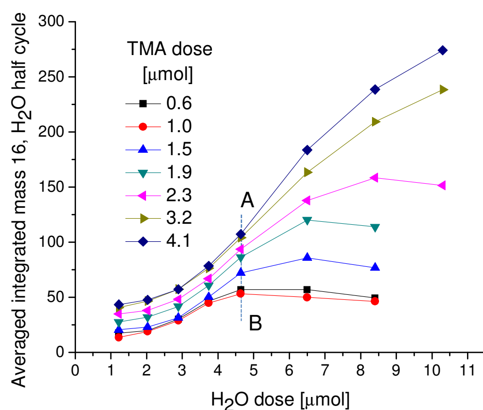

Figure 28 - QMS data for mass-16 (CH_4) integrated over H_2O half cycle periods and averaged over 10 cycles at different TMA and water doses.

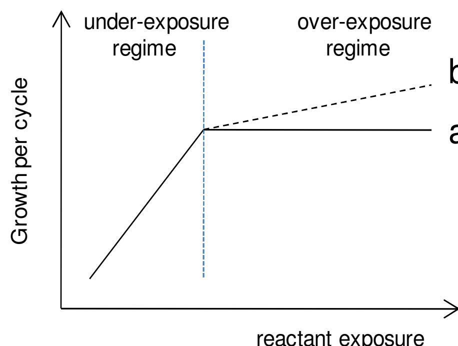

Figure 29 – Schematic of ALD regimes based on growth per cycle vs. reactant exposure: a) "ideal" ALD process with saturating self-limited growth, b) pseudo-ALD growth.

The results are shown in Figure 28 with some intermediary results left out for clarity. This graph provides a set of cross-sections of the ALD process space, each cross-section being similar in nature to the one discussed in Figure 26. A number of comments can be made in relation to Figure 28:

(1) For the first 5 cross-sections corresponding to TMA doses ranging from 0.6 to 2.3 µmol, the generation of CH_4 by-product does reach a plateau as the water dose is increased indicating saturation behaviors.

(2) Based on the results from Figure 26b where a saturation of mass-16 was observed at 4.5 µmol TMA and ~9 µmol water, it was expected to see a similar trend on Figure 28 for the cross-sections at 3.2 and 4.1 µmol TMA when the water dose reaches 10 µmol or so. The 2 sets of data appear in disagreement. It is likely that the onset of saturation for these TMA doses has drifted beyond 10 µmol of water as a consequence of exposing repeatedly the system to high water doses over long period of time which can cause a buildup of water moisture in the reactor. If so, the TMA doses needed to achieve saturation would likely increase as parasitic reactions occurs in the system.

(3) Interestingly a second set of observations can be drawn if one analyzes these data by looking at the amount of methane produced at a fixed water dose, i.e., along a vertical axis (such as the one represented by segment AB on Figure 28). Mass-16 appears to saturate at 3.2 and 4.1 µmol TMA doses for water

doses up to 4.7 μmol, and diverge above 4.7. The results at 4.7 μmol of water are in good agreement with those from Figure 26a that showed saturation at 4.5 μmol of water for TMA doses above 3 μmol. The divergence at higher water doses would be consistent with a mechanism where the density of hydroxyl reaches uniform coverage at ~4.7 μmol of water but keeps increasing at higher water exposures requiring in turn more TMA to reach saturation. Such interpretation would be in agreement with the results from Matero and al. discussed in Chapter I.

There is no question that the QMS results in Figure 28 are not consistent with ideally self-terminating and saturative reaction mechanisms where the GPC would remain constant at higher doses as depicted by curve (a) in Figure 29. Indeed under such ideal ALD growth, one should eventually observe an overlapping of the curves when the doses of TMA and water are high enough to saturate the surface. The fact that it does not occur could reflect a pseudo ALD regime where complex adsorption behavior of water at high exposures would result in increased growth rates. This behavior could be initiated by a combination of increased hydroxyl groups coverage at high water partial pressures as suggested by Kuse and Matero[38, 53] and/or multilayer water physisorption caused by hydrogen bonding. The problem may be compounded by the repeated exposures of excess water relative to TMA required to span the process space. Even the extended purge times set up in this experiment may not be sufficient to counteract the potential multi-layer adsorption of water over time

which would likely put off balance the delicate equilibrium between complementary ALD half reactions.

Despite these apparent flaws, these QMS results provide important clues regarding the saturation behaviors for both TMA and water and will be used in the next chapter as reference points when analyzing the process performances from an ex-situ perspective. The data from Figure 28 will be revisited in more details in Chapter 4 in comparison with ex-situ thickness measurements achieved across the TMA-water process space.

3.7 - Prediction of thickness uniformity using QMS

Downstream QMS sensing facilitates the tool/sensor integration and ensures that the process flow in the reactor is not disturbed by the gas sampling. However, contrary to QCM, in-situ ellipsometry or capillary-based QMS, downstream QMS cannot provide localized sensing information. We may therefore question if downstream sensing can help monitor trends such as thickness uniformity vs. reactant exposure.

Four alumina films were therefore deposited over 100 ALD cycles at 275˚C using a fixed 6.5 µmol water dose and diminishing TMA doses ranging from 3.22 to 0.29 µmol. The film thicknesses were then measured ex-situ at 9 points across the wafer in the direction of the cross-flow. The results shown in Figure 30a indicate a clear degradation of the thickness uniformity across the wafer with decreasing TMA doses. Mass-16 peaks were integrated over each water half-cycle and summed up

over the length of the run. The results shown in Figure 30b (left axis) indicate a decrease of mass-16 peaks at lower TMA doses. The thickness non-uniformity,

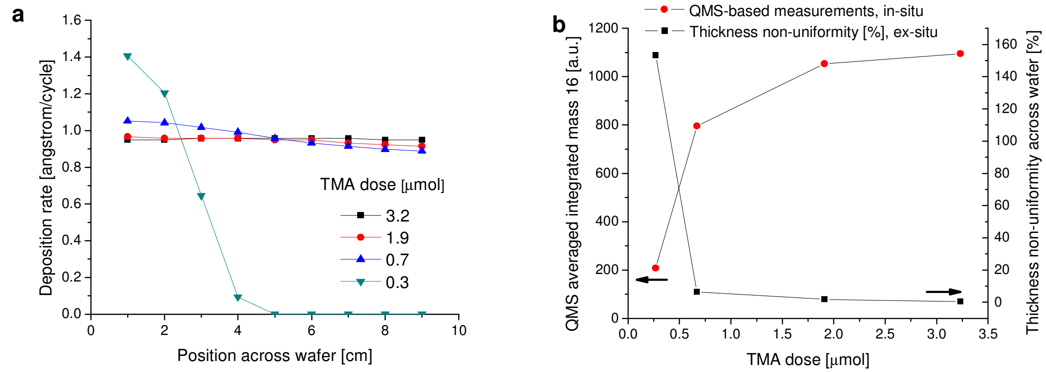

Figure 30 – Correlation between film thickness uniformity across 100 mm wafer and downstream QMS sensing. a) thickness profiles for four Al_2O_3 ALD runs at varying TMA doses and a fixed 6.5 µmol dose of water. b) in-situ QMS data for mass-16, integrated over water half cycles and averaged over the whole run (left scale), and ex-situ thickness non-uniformity (right scale) as a function of TMA doses.

calculated as 1σ/mean, is displayed on the right scale. It is apparent that ex-situ and in-situ data show a good agreement: while the non-uniformity decreases to 1.8% at 1.9 µmol and 0.4% at 3.2 µmol, the corresponding methane generation does plateau. At the opposite, the sharply lower QMS signal at 0.3 µmol reflects the substantial decrease of uniformity as alumina is deposited over less than half of the wafer.

While downstream QMS cannot provide information on local growth behaviors, it can yield reasonably accurate feedback regarding the deposition behavior at the wafer scale. As such the technique could be useful to detect potential process faults resulting in non uniform growth.

3.8 - Real-time monitoring of nucleation kinetics

In order to investigate the impact of ALD growth delays induced by nucleation kinetics, 3 runs were carried out at 275˚C using 3.2 µmol TMA and 6.5 µmol water using different sample preparation: 1) no cleaning (resulting in 2.5 nm native oxide), 2) dipped for 30 s in 5% HF solution and nitrogen blown dry, 3) dipped for 30 s in 5% HF solution, DI water rinsed and nitrogen blown dry. Mass-16 data were integrated at completion of each water half-cycle. The results shown in Figure 31 indicate that regardless of the sample preparation, the amount of generated byproduct saturates within 5 to 7 cycles. After the 3rd cycle, the byproduct generation has already reached 94% of its maximal value, illustrating the high reactivity of the TMA / H_2O system. The result on H-terminated Si surfaces, i.e., HF-cleaned, indicate that the process is sufficiently reactive to break the Si-H bonds and form Si-OH bonds instead on the whole Si surface. The fact that the 3 sets saturate at the same level is a

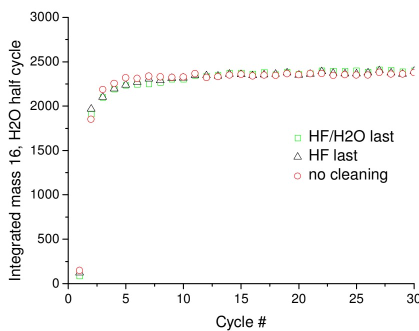

Figure 31 – QMS mass-16 integrated over water half cycle vs. cycle number for Al_2O_3 ALD runs at 3.2 µmol TMA and 6.5 µmol H_2O exposures over 3 Si wafers: untreated, HF-cleaned last, HF-cleaned and DI water rinsed last.

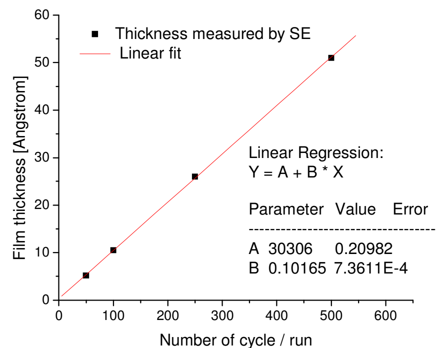

Figure 32 – Film thickness measured by ellipsometry for 4 ALD runs at 275˚C with varying number of cycles. Linear regression confirms the absence of nucleation-induced growth delay.

likely indicator of similar GPCs in the linear growth regime. The excellent thickness control of the alumina process is clearly shown in Figure 32 where, under the same exposure conditions, 4 wafers with native oxide were processed over 50 to 500 cycles. The GPC determined from the linear fit was 1.0 Å/cycle. Extrapolation to zero indicates no growth delay confirming the validity of the QMS data.

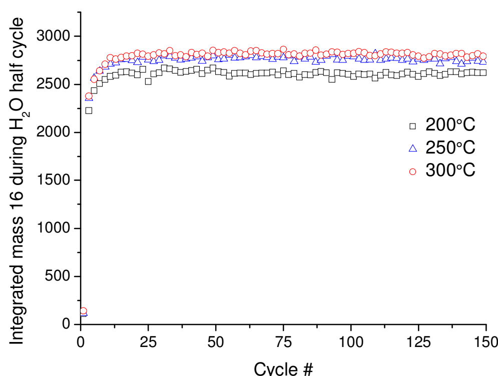

Figure 33 – Integrated QMS data (mass-16) for 3 runs at 200, 250 and 300˚C.

The effect of process temperature on film growth was also surveyed by carrying out 3 runs at 200, 250 and 300˚C. The in-situ QMS data in Figure 33 show a 6% decrease over the length of the 200˚C run which is good agreement with the decrease of growth rate measured by ellipsometry from 1.0 Å/cycle at 300˚C to 0.95 Å/cycle at 200˚C.

3.9 - Discussion and conclusion

Due to their good chemical selectivity and partial pressure sensitivity, QMS sensing has proved very valuable for fault detection and in-situ chemical diagnostics, helping to identify reaction pathways in CVD and ALD processes. Our work in W ALD was a significant contribution in the ALD field by showing that quantitative measurements of reactants and byproducts partial pressures could be correlated to

growth per cycle. This downstream approach allowed the monitoring of the process without tool or chemistry modification and provided real-time information about nucleation kinetics and wafer-state metrology.

The transition from the WF_6/SiH_4 to $Al(CH_3)_3/H_2O$ chemistry added substantial challenges. (1) The low vapor pressure of the precursors resulted in short (500 ms) pulse-type pressure bursts rather than relatively long (10 s) steady exposures delivered by mass flow controllers. Faster acquisition times achievable with the new MKS Vision 1000C were important to capture the pulse dynamics. (2) In the ion source, the metalorganic precursor $Al(CH_3)_3$ can crack in many organic compounds including CH_4^+, the main reaction byproduct. Monitoring the methane byproduct generation during the water half cycle rather than during the TMA half cycle helped at minimizing the impact of TMA cracking but prevents measuring the depletion of the TMA reactant during reaction. (3) Parasitic surface reactions induced by water high polarity proved significant. While water is commonly used as an oxidation precursor in ALD, its complex adsorption/desorption behavior in low pressure reactor systems is well known resulting in "wall memory" effects. In pursuing QMS experiments to identify a suitable ALD process window, the history of water dosing becomes a significant factor, especially because the relatively low wafer and wall temperatures employed in ALD do not allow rapid water desorption from the walls. Thus the amount of residual water in the ALD process ambient depends on the dose history of water, and dosing experiments like these are thus best carried out with monotonically increasing water doses, to minimize unwanted water background effects.

Despite these challenges the benefits of QMS sensing in the Al_2O_3 ALD were substantial from a tool and process optimization perspective. Similarly to the W ALD process, impacts of sample preparations or temperature on the film growth were readily observed. QMS sensing proved also crucial during the initial phase of the tool reconfiguration and process characterization by revealing unexpected condensation of the metal organic precursor in the delivery line which resulted in a deterioration of the process performance (unstable GPC, thickness non-uniformity). The condensation lead to a broadening of the mass 16 peaks as condensed TMA was slowly desorbing from the wall.

In the next chapter we will investigate how dose exposures and purges did impact process performances at the wafer scale. The QMS results anticipating saturating conditions at 3 µmol TMA and 3-10 µml water will be reexamined in the context of the more complete ex-situ characterization.

Chapter 4: Cross-wafer thickness uniformity in Al_2O_3 ALD

4.1 - Introduction

In the previous chapter, we used downstream mass spectroscopy to infer process behavior from reaction products and reactant depletion and delineate the contour of the Al_2O_3 ALD process space using TMA and water. In this chapter, we intend on using this parameter space as a starting point for a more detailed investigation of the ALD process regime based on ex-situ post-process uniformity measurements as a function of precursor dose conditions. Our cross-flow ALD reactor design produces a spatially varying flux of ALD impingement by precursors and products across the wafer. By measuring conditions from under-dosing to over-dosing of precursors (compared to dose amounts that achieve ideal ALD behavior, i.e. excellent uniformity) under variable purge times, the cross-flow design highlights the limits of the appropriate ALD process window, thus using real wafer-level uniformity as a metric for true ALD behavior.

It is worth noting that many publications on ALD identify a process window primarily from the dose at which growth rate saturates as measured on convenient, small "chip-size" samples and then investigate the film properties obtained at or slightly above the "ideal" saturating doses. In contrast, approaches conventional in industrial practice typically use design of experiments on full wafers. While they ultimately provide a path to viable ALD processes, they do not provide useful

feedback on either the intrinsic process limits for a given ALD chemistry or the mechanisms involved. With a dramatically expanding field of applications for ALD in sight along with more complex multi components chemistries, we believe greater insight into ALD processes will be needed to reach their full potential.

Water is arguably the most commonly used oxidant for ALD as it exhibits high chemical reactivity with ALD metal precursors, high vapor pressure at room temperature, is low cost and inherently safe. However water high molecular polarity is well known in vacuum technology to cause complex adsorption/desorption kinetics due to potential hydrogen bonding on substrate and reactor wall surfaces. As an alternative, hydrogen-free oxidants such as ozone or radical oxygen are favored in manufacturing. To illustrate the impact of water-based surface chemistry on process performances, the TMA/ozone system will be also investigated.

4.2 - Experimental protocol

The experimental setup for the Al_2O_3 ALD process has been described in details in chapters 2 and 3. Maps of the film thickness and refractive index were obtained using the Sopra GES5 spectroscopic ellipsometer. Samples were measured near the Brewster incidence angle for silicon at 75°. In the case of very thin films (<5 nm), measurements at additional angles were required to extract both thickness and refractive index. A Cauchy dispersion law was used for the modeling of the film optical properties. Al_2O_3 has an optical band gap of 8.8 eV and is non-absorbing ($k=\varepsilon_2=0$) in the visible range. In this case, the dispersion of the refractive index can be described by a standard Cauchy relationship:

$n = A_n + B_n / \lambda^2 + C_n/\lambda^4$ where A_n, B_n and C_n are the Cauchy fit parameters. The thickness profiles were measured from 10 to 30 equidistant points across the wafer in the direction of the flow. The metric for non-uniformity was established from the ratio of the standard deviation over the mean value, 1σ/mean.

4.3 - Results: across-wafer uniformity

Measurements of across-wafer uniformity are in some sense the gold standard for ALD. If the self-limited adsorption/reaction behavior of ALD is obtained for a given precursor in a specific ALD chemistry, then moderate overdosing of that precursor should not adversely affect ALD performance, but simply ensure the full surface saturation is achieved. We follow this strategy in the following. Here we investigate this metric by varying the dose of one precursor while holding the complementary dose of the other precursor constant.

4.3.1 Effect of water dosing on thickness uniformity

Using the previous QMS results as a reference for the TMA dose leading to saturation, five wafers were consecutively processed using a fixed TMA dose of 6.3 μmol (about 2x the assumed saturation dose) while varying the water dose. The corresponding thickness profiles along the direction of gas flow (left to right) in our cross-flow ALD reactor are shown in Figure 34. The purge times were maintained constant at 20 s regardless of the water dose. As expected for self-terminated ALD reactions, excellent uniformity (<1% at 1σ/mean) could be achieved under the right conditions, namely at 3.1 μmol water dose, with a deposition rate of 0.95 Å/cycle,

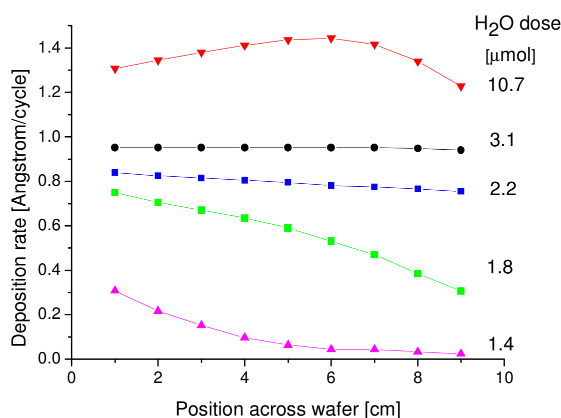

Figure 34. Across-wafer thickness profiles for five water doses with fixed TMA dose (6.3μmol).

in good agreement with the literature.[38]

At the higher 10.7 μmol dose, Figure 34 reveals a substantially higher (30-40%) growth rate per ALD cycle. This result appears consistent with the observations by Matero, Li and Kuse that we reported in Chapter 1.2 [38, 53, 54] where higher water concentration resulted in higher conversion of the active methyl sites on the surface and higher GPC. It is important to emphasize at this point that in our reactant delivery scheme, higher doses are achieved not by increasing the exposure time but by increasing the setpoint pressure in the delivery vessel. The resulting higher amplitude gas pulse translated into a higher reactant partial pressure and concentration across the wafer, similar in behavior to the higher flow rate used by Matero or higher pressure in Li's case.

The suggestion at this point is that from 3 μmol and upward, water does saturate the surface under the equilibrium conditions governed by the partial pressure achieved upon the release of the pressure-controlled dose in the delivery vessel. But increasing doses beyond 3 μmol results in higher partial pressure that allows for adsorption to higher coverage and therefore enables higher growth rates per cycle.

The 6.3 μmol TMA dose used in Figure 34 being twice the saturation TMA dose inferred from Figure 26a, enough extra TMA is available to react with the increased concentration of hydroxyls on the surfaces resulting in the 40% higher GPC at 10.7 μmol of water.

Based on these observations, the leveling of the methane byproduct signal observed by QMS around 10 μmol (Figure 26b) is a likely indicator of the maximal saturation achievable on the surface. These results would also be in good agreement with the data obtained from the automated exploration of the [$Al(CH_3)_3$, H_2O] process space (Figure 28) where we noticed the amounts of methane for $Al(CH_3)_3$ doses of 3.2 and 4.1 μmol were diverging at water doses above 4.7 μmol. Retrospectively we can attribute this divergence to an increase of the hydroxyl surface coverage which in turn requires additional TMA to react.

At lower water doses from 2.2 to 1.4 μmol, the thickness uniformity degrades progressively, as seen in Figure 34. As expected for chemisorbed surface reactions, without sufficient water to react the adsorbed TMA, we expect lower growth rates, as observed. For our cross-flow ALD reactor design, we expect depletion of water coverage across the wafer. Indeed, such a thickness gradient is observed, with a thicker film near the inlet (left) and thinning out towards the outlet of the reactor (right), with no sharp thickness discontinuity across the wafer.

4.3.2 Effect of TMA dosing on thickness uniformity

A complementary experiment was carried out at fixed water dose (3.9 μmol, i.e., 25% higher than the saturation dose determined from thickness uniformity

profiles in Figure 34) and varying TMA dose. As seen in Figure 35a, for TMA doses at or above ~3 µmol, uniformity and deposition rate remained essentially unchanged. Since the water dose was slightly above saturation value, this finding confirms that for the TMA adsorption, the maximal surface coverage of $Al(CH_3)_2^*$ species is independent of the partial pressure of TMA and is instead determined by steric hindrance of the adsorbate and the atomic arrangement on the surface.

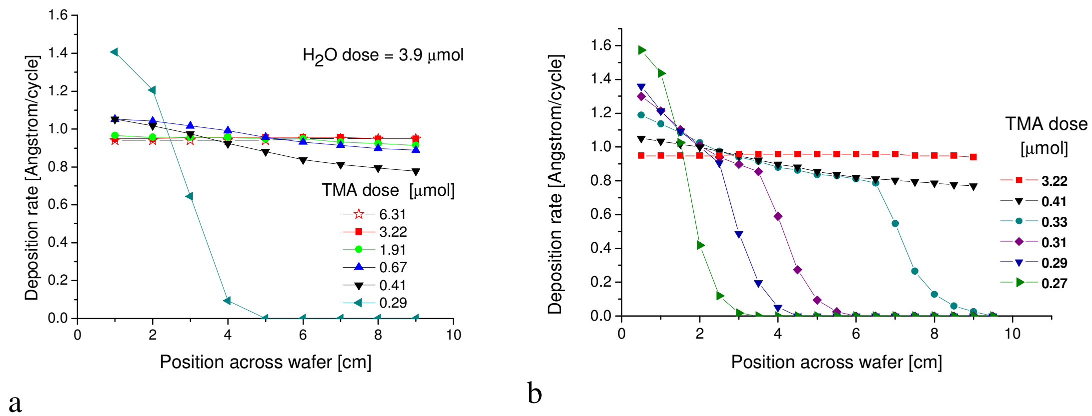

Figure 35. Across-wafer thickness profiles for fixed water dose (3.9 µmol) and varying TMA doses. The data were split in 2 graphs for clarity (a) emphasis for TMA doses close to saturation (b) emphasis for TMA dose in under-exposure regime.

With decreasing TMA dose, uniformity degrades, first evidenced by moderate depletion across the wafer, lower thickness downstream (right) and higher thickness (left), shown in Figure 35a. Below 0.41 µmol, the thickness profile exhibits a more dramatic depletion with an abrupt drop near the downstream side of the wafer. With further decrease in TMA dose, this behavior continues (Figure 35b), with the depletion edge shifting further upstream (left) and the deposition rate increasing substantially at the upstream (left) portion of the wafer.With the water dose somewhat

above (+30%) the ALD saturation dose, further water adsorption may be concentrated at the upstream end of the wafer. If the TMA can react with more than a single layer of water on the surface, as is likely, then the water will preferentially react with the limited TMA dose at the upstream end, which in turn may facilitate further water adsorption on the next cycle. In other words the thickness profile anomalies in Figure 35b may be regarded as deviations from "ideal" ALD behavior in which the cross-flow ALD reactor design emphasizes or even exaggerates deviations caused by the synergistic effects of under-dosed TMA being depleted across the wafer and increased coverage with –OH at water doses above the initial saturation at 3 µmol.

4.3.3 Effect of dose ratio

In the two previous cases, one reactant had been underdosed while maintaining the other to a level that had initially been determined as sufficient to achieve optimal uniformity and growth rate. This led to striking non-uniformities, especially for fixed saturation water dose and decreasing TMA dose, seen in Figure 35b. With strong underdosing of TMA, the question arises as to whether simultaneous underdosing of water would re-establish a reasonable measure of uniformity. To test this, the TMA dose was maintained at 0.31 µmol, an underdose condition that resulted in sharp non-uniformity in Figure 35b, while the water dose was varied from an initially saturating level, 4.86 µmol, down to 0.56 µmol over 6 consecutive runs. As seen in Figure 36, uniformity under these TMA-starved conditions is partially restored when the water dose is decreased. Between 1.38 and 0.97 µmol water doses,

the thickness profile does not exhibit the sharp discontinuity observed earlier. Thus improved uniformity results, though with lower deposition rate as a balance was re-

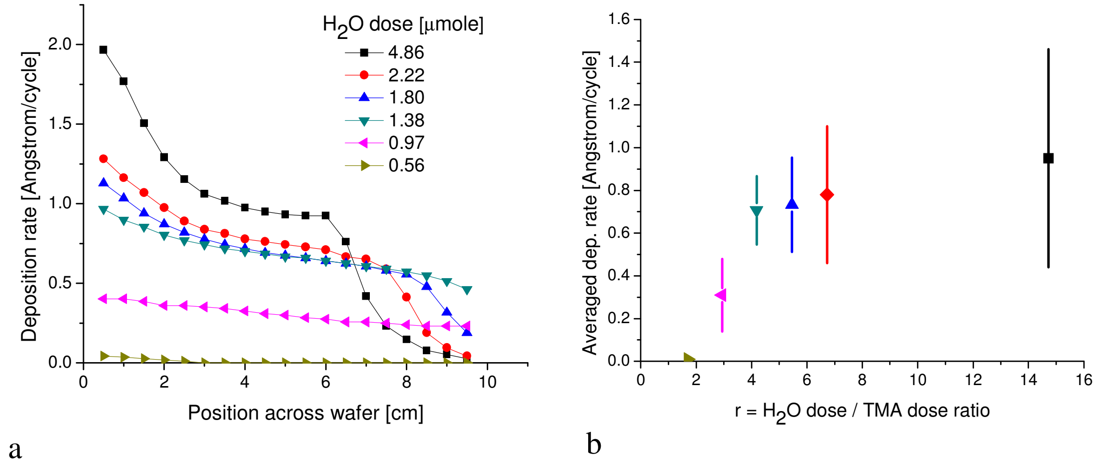

Figure 36. Uniformity for under-dose conditions of TMA (0.31 μmol) and water. (a) Thickness profiles show improved uniformity, though deposition rates are lowered and ALD uniformity is not achieved. (b) Area-averaged deposition rate as a function of r=water/TMA dose ratio. Height of vertical bars indicates extremes of deposition non-uniformity on the wafer.

established between TMA and water availability at all points across the wafer. However, none of the profiles exhibit high uniformity as expected from ALD, because neither dose was adequate for surface saturation. In addition, the cross-flow reactor design defined a clear depletion direction that is decorated by the reduction in thickness along the flow direction.

In an attempt to better quantify the non-uniformities across the wafer, we determined growth rates averaged over the two-dimensional area of the wafer, which are shown as data points in Figure 36b as a function of the water/TMA dose ratio, r. The vertical bars reflect the non-uniformity measured across the wafer for each ratio r. The results show that the non-uniformity increases when water is in excess relative

to TMA, from about 30% non-uniformity at r=4 to >100% at r=14. The average film deposition rate reveals two distinct trends. For r<4, the average growth rate drops significantly, indicating that both doses were too low to achieve full saturation across the wafer and to sustain the optimal growth rate. For r >4, the average growth becomes nearly constant, reflecting a mass balance between the amount of materials lost from depletion in the back-end region of the wafer and what is gained closer to the inlet region. At the same time, the non-uniformity increases notably, indicative of the phenomena shown in across-wafer thickness profiles in Figure 35.

4.3.4 Results: uniformity and purge times

The uniformity data indicate that when the water dose (relative to saturation) is large compared to the corresponding metric for TMA, the growth rate increases significantly near the inlet zone, up to twice the nominal value of 0.1 nm/cycle. As mentioned above, this non-ideal ALD behavior is likely a consequence of the increased coverage of hydroxyl groups on the surface resulting from the relative excess of water and the availability of $Al(CH3)_2^*$ reaction sites at the upstream portion of the wafer when TMA is under-dosed. With the complex adsorption behavior of water, that can monolayer-chemisorb at different saturation levels, or even potentially multi-layer physisorb, we can question how the purge times will impact the $–OH^*$ surface coverage and consequently the thickness uniformity. To assess this, experiments were carried out under conditions of water over-dose (4.86 μmol) and TMA under-dose (0.3 μmol), i.e., r=16, keeping TMA purge time 20 s as before but varying water purge time from 20 to 120 s.

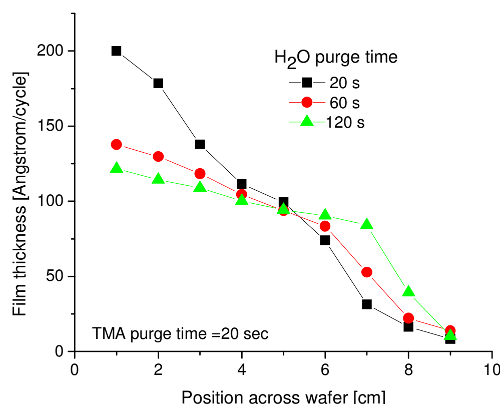

Figure 37. Across-wafer uniformity for over-dosed water (4.86 µmol) and under-dosed TMA (0.3 µmol), with varying duration of purge cycle after water dose. Purge time after TMA dose = 20 s.

Results are shown in Figure 37 and indicate that increasing the water purge time significantly reduces the overgrowth upstream near the inlet zone. This could be caused by dehydroxylation reactions where hydroxyl sites recombine on the surface to form a water molecule that can desorb. Dehydroxylation has been shown to occur at temperatures as low as 130˚C.[90] It is also possible that if water multi-layer physisorption is occurring (concurrently with chemisorption) then the longer purge times would help desorb the weakly hydrogen-bonded water molecules.

Also attenuated is the sharp depletion of deposition downstream, associated with the under-dosing of TMA. This suggests that the reaction of water upstream had been enhanced by the presence of upstream TMA (in under-dosing situation), and that the preferential adsorption of water upstream in the cross-flow geometry had caused enhanced gettering of TMA upstream. In other words, Figure 37 in concert with previous data suggests that the cross-flow reactor configuration decorates deviations from an ideal ALD process window by synergistic effects of adsorption, depletion, and reaction between the two precursors.

4.3.5 Al_2O_3 ALD from TMA and ozone

To help better understand the contribution of the oxidant on the growth mechanisms and its impact on thickness uniformity, a similar set of experiments was undertaken where water was substituted with ozone (O_3). The choice of ozone removes the possibility of hydrogen bonding as a means for added oxygen-containing species on the surface, providing a test for inferences above about the role of water-related species beyond ideal ALD surface self-limiting behavior.

In the first set of experiments, ozone exposures were controlled by adjusting the pulse time from 1.2s down to 50 ms at a fixed TMA dose of 1.6 µmol (Figure 38). Similarly to water / TMA, excellent thickness uniformity across the 100 mm wafer was achieved (1σ/mean < 0.4%) at 1.6 µmol of ozone[8]. However key differences are noticeable with the results from the water dosage experiment seen Figure 34: (1) upon ozone over-exposure (3.2 µmol), the GPC remained unchanged at 1.04 Å/cycle. Contrary to water, in the overexposure regime, the surface site conversion occurring during the adsorption of ozone doesn't appear to be dependent on the concentration of ozone. This would indicate that the ozone adsorption equilibrium is such that the surface site coverage has reached a maximum value by 1.58 µmol and that no further chemisorption is possible. Also due the absence of hydrogen bonding, potential parasitic reactions from multi-layer physisorbed molecules can be excluded. (2) Quite

---

[8] The values are taking into account the 20% O_3 and 80% O_2 mixture delivered by the ozone generator. 1.6 µmol represents 20% of the total pulse, or 7.9 µmol. Experiments with only O_2 under same process conditions showed no growth.

strikingly, when under-exposing ozone, the uniformity only moderately degrades across the wafer while the GPC decreases rapidly consistent with to the low ozone doses. In this case, the spatial distribution of the oxidant molecules in the cross-flow reactor does not result in depletion effect where the deposition rate decreases along the wafer. It is possible that the one-to-five dilution of ozone in oxygen results in a more homogeneous environment across the wafer and buffers the impact of a pulse-wave traveling across the wafer and getting depleted.

In a second set of experiments, TMA exposures were lowered from 2.46 to 0.07 µmol under a fixed 1.6 µmol dose of ozone. The results indicate a constant GPC from 1.19 to 2.46 µmol showing no effect of TMA over-exposure, as in the water/TMA case. The thickness uniformity steadily degrades between 1.19 down to 0.24 µmol as the reactant is depleted across the wafer though the deposition rate in the inlet zone remains at 1.06 Å/cycle. At 0.16 µmol and below, a monotonic depletion remains and

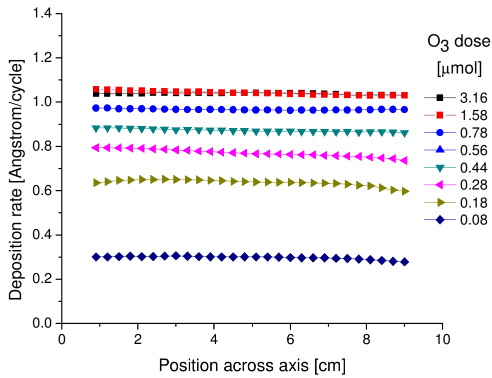

Figure 38 - Across-wafer thickness profiles for 8 ozone doses with fixed TMA dose (1.6 µmol).

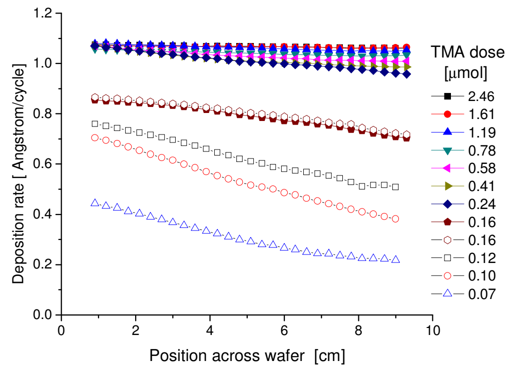

Figure 39 - Across-wafer thickness profiles for 12 TMA doses with fixed ozone dose (3.2 µmol).

the overall GPC finally decreases as the TMA doses are insufficient to saturate the surface.

4.4 - Discussion and conclusion

This work has explored a dose/purge process spaces for the TMA/water and TMA/ozone chemistries which are considerably larger than a practitioner would utilize, given the extent to which this process is already used reliably. The purpose has been to more broadly identify mechanisms which control ALD uniformity and growth rate and to develop techniques that reveal these for their subsequent use in ALD research and development for a variety of ALD chemistries and materials applications.

Across-wafer uniformity measurements achieved in a cross-flow configuration highlights and underscores the surface chemical complexity which can accompany even the most commonly used ALD process, that of Al_2O_3 from TMA and water. It is true that the cross-flow configuration exaggerates both non-uniformity and non-ideal ALD mechanisms responsible for it. However, this can be viewed as an advantage in that it identifies regimes where ALD is imperfect, perhaps to the extent that demanding applications cannot tolerate. Furthermore, cross-flow, low-volume ALD reactor designs have substantial interest for manufacturing equipment in terms of cycle time and wafer throughputs.

The behavior of water is particularly striking in these results. Its ability to monolayer chemisorb at different levels of saturations has significant ramifications for ALD process optimization that must be carefully understood in order to realize the

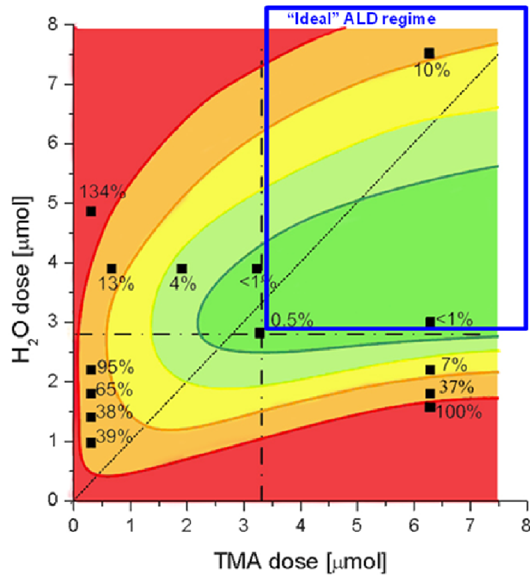

Figure 40 – Schematic contour map of across-wafer non-uniformity as a function of TMA and water doses, obtained from thickness profiles in this work.

full benefits of ALD self-limiting surface reaction, thickness control, uniformity, and conformality. These observations about water as a precursor are particularly important because water is commonly used as oxidant for oxide ALD processes.

A schematic representation of the uniformity data for the TMA/H_2O system is presented in Figure 40, over which contours have been added to reflect an interpolated view of this ALD behavior. Perfectly self-limiting adsorption/reaction, the basis of ALD's benefits, would imply essentially perfect uniformity in the upper right quadrant: as either reactant dose is increased above its saturation value for that precursor, it would cause no further surface reaction and leaves the ALD system

without interaction on the wafer. This specifies the "ideal" ALD regime denoted in the figure.

Indeed, exceptional uniformity has been observed here, and in numerous publications, as seen by the green contour of uniformity better than 1% near 3 μmol for both precursors and for higher TMA dose as well, reflecting the observation above that

TMA itself seems well-behaved in terms of self-limiting adsorption/reaction in this ALD chemistry.

The situation deviates from ideal in the direction of water overdose, where significantly enhanced growth rates (up to 40%) and non-uniformities are observed, e.g. the 10% non-uniformity at high dose in Figure 40 that arises from the 10.7 μmol water. Also, corresponding to the data in Figure 40, strong non-uniformities are indicated for under-dosed TMA and over-dosed water in Figure 35.

From these data, it appears that in order to optimize the film deposition at the wafer scale, one must take into account the complex adsorption behavior associated with water-based surface chemistry and the change in adsorption equilibrium and –OH^* saturation coverage with water concentration. As mentioned in Chapter 1.4, ALD reactor designs can significantly impact the ALD process performances. This is particularly true when it comes to designing the delivery system. The fact is that just controlling the number of molecules going into the system is not sufficient to characterize the process space. Understanding how the partial pressure is affected when controlling the dose is critical. As such, the examples based on Matero's and this current work are very revealing. Adjusting water exposure time under fixed flow rate conditions will reveal the onset of reaction self-termination but will not necessarily reveal the optimal saturation conditions that depend on the saturation equilibrium and the oxidant partial pressure. This consideration should be carefully taken into account when designing or buying an ALD system as many approaches to reactant delivery are available and likely to present pros and cons. To some extent,

the end-point pressure control adopted for this reactor offers the benefits to very accurately and reproducibly control the dose without having to rely on the exposure time (which is a less accurate way of controlling the dose). However one must certainly recognize the impact of higher partial pressures at higher doses on the saturation behavior of the water molecules.

While the hypothesis of higher hydroxyl coverage achieved through chemisorption at higher water partial pressure is favored by Matero[38] and Kuse[53], it is also known that water molecules may be adsorbed to form multilayers on the surfaces of various oxides, including Al_2O_3[91], TiO_2[92], SiO_2[45], ZrO_2[93] and HfO_2[37, 93]. It has been shown that while the first layer bonds to the surface via chemisorption, additional layers are all physisorbed with slowly diminishing bonding strength. Though these studies were not achieved in the context of an ALD process, but rather looking at interactions of water with oxides surfaces, it is however quite likely that such effect occurs in ALD during the water exposure at high partial pressure.

In light of these results, it is interesting revisiting the QMS-based results from chapter 3. Data from Figure 26a indicated a clear saturation behavior of the TMA reactants around 3 µmol which appears in excellent agreement with the results shown above. This saturation was also observed in Figure 28 where the amount of methane were identical at 3.2 and 4.1 µmol TMA for water doses below 4.7 µmol. The prognostic was more uncertain when evaluating the saturation exposure for water. Figure 26b showed partial saturation of the methane byproduct signal occurring at

water doses around 10 µmol, significantly above the 3 µmol that were showed in Figure 34 to be needed to achieve optimal uniformity and a GPC of 0.95Å/cycle. In fact, these QMS results only reflect the 40% increase of the GPC when increasing the water dose from 3 to 10 µmol as a result of an increase in –OH* coverage and the likely formation of water multilayers through hydrogen bonding. It is worth noting that more direct measurement approaches such as QCM or ellipsometry would have also showed higher values under these conditions.

Retrospectively the results obtained during the automated exploration of the [H_2O, TMA] space (Figure 28) appear quite consistent with the complex adsorption regimes revealed by ex-situ measurements. The fact that the curves obtained for different TMA doses did not eventually overlap with one another (as would have been expected from a self-saturating ALD process) was an indicator of the ability to increase the GPC beyond 0.95Å/cycle as a result of water multilayer formation. The fact that the methane generation did eventually reach a plateau[9] indicates that the number of multilayers forming in the water over-exposure regime is likely to reach a maximum value for a given TMA dose which would cause the GPC to stabilize.

A close examination of the slopes along these individual curves (Figure 29) indicates 3 different regimes as a function of the water doses: (1) the slopes increase moderately within 1 to 3 µmol water doses, (2) then more rapidly above 3 µmol before reaching a plateau (3). The first regime would correspond with an ideal ALD

---

[9] The plateau does not occur at 3.2 and 4.1 µmol but it seems reasonable to assume that it would occur outside the process window characterized in this experiment.

growth that only involves monolayer formations via reactions on hydroxyl groups distributed solely on a two-dimensional surface. Above 3 µmol of water, the OH* coverage reaches saturation and water multilayer formation is initiated due to the higher water partial pressure in the reactor. If so, TMA molecules react with water/hydroxyl groups adsorbed over several layers and the amount of methane increases rapidly as a result. Finally the water physisorption self-limits itself at the water dose increases and the amount of methane (and GPC) reach a plateau.

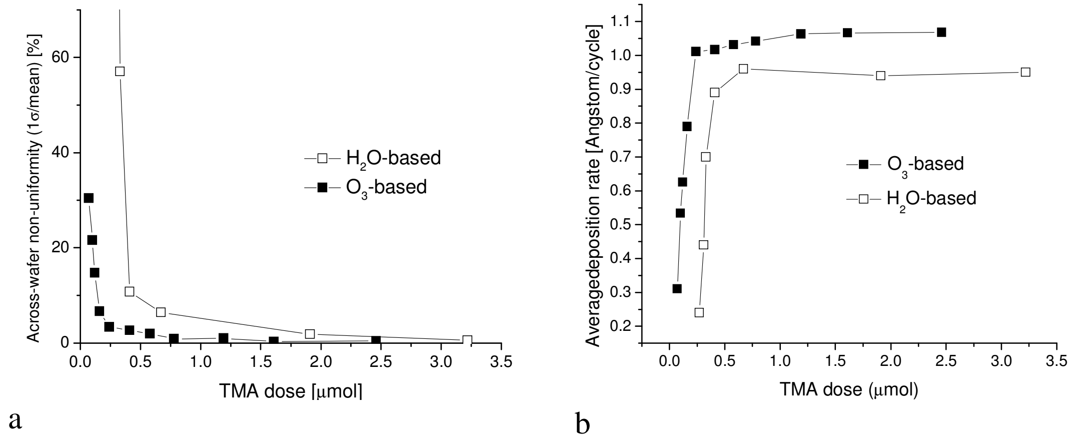

Figure 41 – Al_2O_3 film characteristics for H_2O and O_3 based chemistries as a function of TMA exposure: a) across wafer non-uniformity (measured as 1σ/mean); b) corresponding deposition rate averaged over 9 measurements

In contrast to water, the ozone / TMA system provides no evidence for formation of excess reactant adsorption beyond a saturating monolayer. From a process performance perspective, i.e., film uniformity, reactant consumption and cycle times, ozone appears a better choice than water. As illustrated in Figure 41a, the thickness non-uniformity for TMA/ozone can be maintained below 1% for

TMA doses as small as 0.8 μmol vs. ~2.5 μmol for water. The optimal GPC corresponding to a fully saturated behavior is also reached at lower TMA doses indicating a more efficient oxidation mechanism. Considering the high cost of ALD metal precursors ($20 to >$100 /g), ozone use can be economically advantageous in high volume production.

Chapter 5: Characterization of Al_2O_3 intrinsic properties

5.1 - Introduction

Accordingly to the self-terminated nature of Al_2O_3 ALD, excellent process performances was achieved under the right conditions of reactant exposure and saturation as indicated by the excellent thickness uniformity obtained from the TMA/water and TMA/ozone systems. However our results for the TMA/water system clearly show that such optimal process performances were only achievable within a relatively narrow process space and that deviations outside of this window resulted in a degradation of the process metrics such as growth per cycle and thickness uniformity. Such thickness variations are likely caused by the synergistic effects of reactant depletion inherent to cross-flow reactor design and complex adsorption/desorption mechanism associated with water chemistry. Under such non-ideal growth conditions, one can question how deviations from saturative and self-terminated monolayer growth do impact the intrinsic properties of the film such as its chemical composition or optical and electrical properties.

In addition, the ability to intentionally generate thickness gradients across a wafer by adjusting the reactant dosage while controlling the thickness at the sub-monolayer level can potentially be used as a methodology for combinatorial ALD. Thin film combinatorial synthesis has been used to achieve continuous or discrete compositional libraries for complex materials systems such as ternaries or

quaternaries [94, 95]. By correlating the materials properties (e.g., magnetization, permittivity, crystallinity), to the local materials composition across a single wafer, combinatorial materials synthesis constitutes a powerful method for rapid materials discovery and optimization of complex materials systems. The kinds of reactant impingement distributions achieved by varying precursor doses in our cross-flow reactor may provide ALD composition gradients for more complex systems such as hafnium aluminates. The objective is therefore to determine if the intrinsic film properties are affected when generating these gradients by ALD under depletion conditions.

5.2 - Al_2O_3 electrical and optical properties

5.2.1 Experimental

Al_2O_3 films were deposited at 275˚C from TMA and water. <100>, p-type, 1-10 Ω.cm resistivity, prime grade silicon substrates were used. The native oxide was stripped and the surface hydrogen-passivated by cleaning the wafer in 5% HF for 30 s, DI water rinsed and nitrogen blown dry. Film thicknesses were measured after the ALD process on the Sopra GES5 spectroscopic ellipsometer. 0.25 mm diameter MOS capacitors were then fabricated to obtain the following structure: Si substrate / 100-500Å Al_2O_3 by ALD / 2000 Å Au by thermal evaporation. Capacitor structures were fabricated via lithography patterning of Shipley 1813 photoresist and gold Transene wet etch. CV and IV wafer maps were obtained with the automated probe station described in Chapter 2. Electrical results were analyzed over ~16 points across the

wafer in the direction of the flow. Using Mathworks Matlab® software, capacitance and current measurements were correlated to thickness profiles established from ellipsometry in order to extract permittivity and leakage current density.

5.2.2 Results

Ideal saturating conditions

As a reference, a 238Å alumina film was first deposited over 250 cycles at 275˚C under ideal TMA and water saturating conditions, respectively 3.3 and 4.5 µmol. Excellent thickness uniformity was achieved (1σ/mean =0.6%). 30 MOS capacitors were characterized across the wafer. The CV characteristics were measured at 100 kHz over a voltage sweep from +4 to -4V. As seen in Figure 42, upon negative applied voltage on the gold electrode, a clear saturation of the capacitance occurs at (1.15 ±0.03) pF, characteristic of hole accumulation in the p-type silicon. A permittivity of 6.3 ±0.15 was determined from Equation 1.[10]

IV characteristics in Figure 42b indicate a leakage current of (7.0±0.7) nA/cm^2 at an applied field of 1MV/cm. The electrical breakdown of the capacitors occurs around 8MV/cm field. These IV values appeared in good agreement with the literature and emphasize the good quality of the film obtained under saturating conditions.[3, 34]

---

[10] The bulk permittivity of aluminum oxide is ~ 9. The lower permittivity can be attributed to: (1) the presence of a SiO_2 interfacial layer (ε_r=3.7). Later measurements of MOS ($Au/Al_2O_3/Si$) and MIM ($Au/ Al_2O_3/Pt$) capacitors showed a 15% higher permittivity in the MIM case where no interfacial layer is formed on Pt, consistent with an interfacial layer of ~10Å and in good agreement with literature.[34] (Appendix, Fig. XIII and XIV) (2) the fabrication method and particularly the use wet chemical etching appears to also significantly degrade the permittivity. An increase of the permittivity from 6.6 up to 8.9 was observed when using a lift-off based technique rather than wet chemical etching. (Appendix, Fig. X) However the lift-off operating procedure was only developed after the acquisition of the current results.

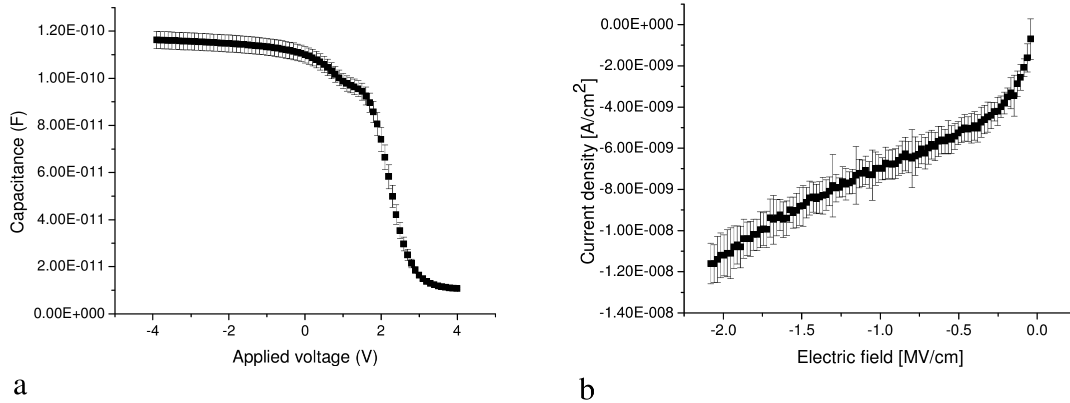

Figure 42 – Electrical characteristics measured over 30 capacitors for 238Å Al_2O_3 film deposited under saturating TMA and water conditions. (a) Capacitance vs. voltage (b) current density vs. applied field.

Water under-exposure conditions

A film was deposited under water-starved conditions, i.e., 1.8 μmol water and 6.3 μmol TMA. The CV and IV characteristics for 7 of 30 measured MOS capacitors distributed along the direction of the flow are shown in Figure 43. The capacitance in the accumulation regime does increase as the film gets thinner as was expected from the inversed correlation between the two (Equation 1). We also notice a dependence of the threshold voltage with thickness suggesting that fixed charges in Al_2O_3 are distributed throughout the film rather than existing only at the interface. As expected, the leakage current, tied to charge tunneling through the oxide, increases as the film gets thinner.

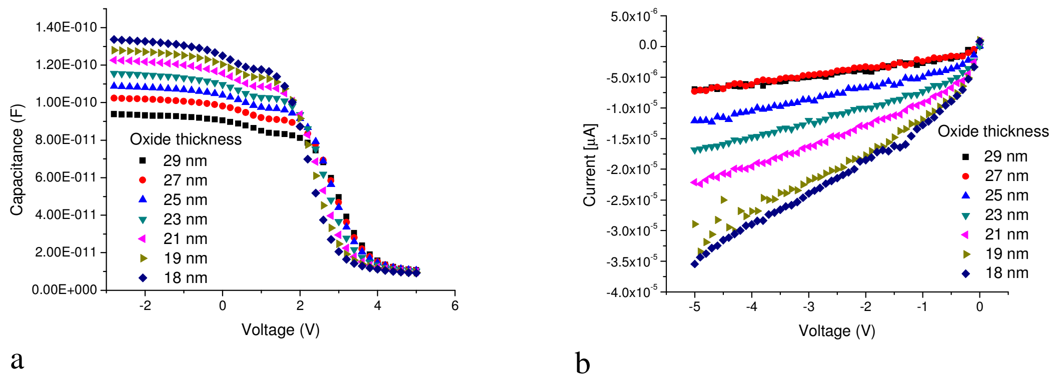

Figure 43 – Electrical characteristics of Au/Al_2O_3/Si MOS capacitors measured across the wafer along the direction of the flow. Film deposited in underdosed water conditions a) CV characteristics at 100 kHz, b) IV characteristics for 0 to -5V voltage sweep.

Using a Matlab routine, capacitance values were extracted at -2V and leakage current at -1MV/cm field. By correlating the 29 thickness measurements across the wafer with corresponding capacitance and current values, a cross-section view of the permittivity and leakage current density can be obtained. (Figure 44) While the capacitance increases as the thickness decreases accordingly to Equation 1, we note that the permittivity decreases by 15% across the wafer. Even when taking account the contribution of the SiO_2 interfacial layer (assumed to be 10Å), the corrected permittivity shown as open triangles in Figure 44 still exhibits a 13% decline. Similarly the leakage current density at a fixed 1MV/cm electric field appears to increase. This indicates that the depletion of water across not only results in a thickness gradient but also in an intrinsic change of the materials properties.

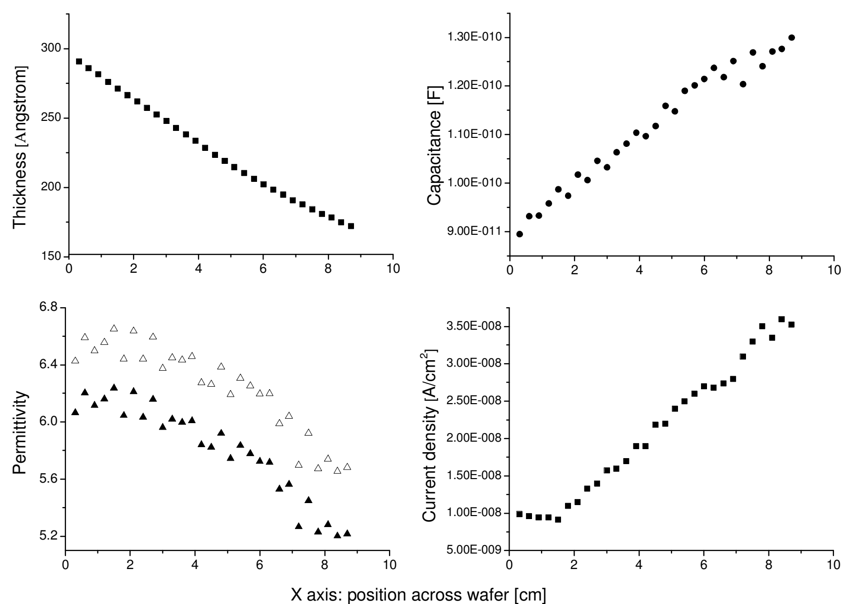

Figure 44 – Thickness, capacitance, permittivity and current density at -1MV/cm as a function of position across wafer for Al_2O_3 film deposited in water-starved conditions. Permittivity calculated with 10Å SiO_2 interfacial layer included (solid triangle) or excluded (open triangles).

TMA under-exposed conditions

The experiment was repeated, this time with an under-saturating TMA exposure (0.33 µmol). Two water doses were used at 2.65 and 0.81 µmol. Thickness, capacitance and permittivity across the wafer are shown on Figure 45, as well as the refraction index. As observed in chapter 4, sharp non-linear non-uniformities are present with a GPC increase near the inlet due to the accumulation of hydroxyl groups resulting from the high dose of water relative to TMA and a sharp GPC decline at the tail of the wafer. In the region from 4 to 7 cm, the thickness is relatively uniform (1σ/mean=4%) and the GPC close to 0.8 Å/cycle, indicating conditions close to an ideal ALD regime. The permittivity values in this region is maximal and

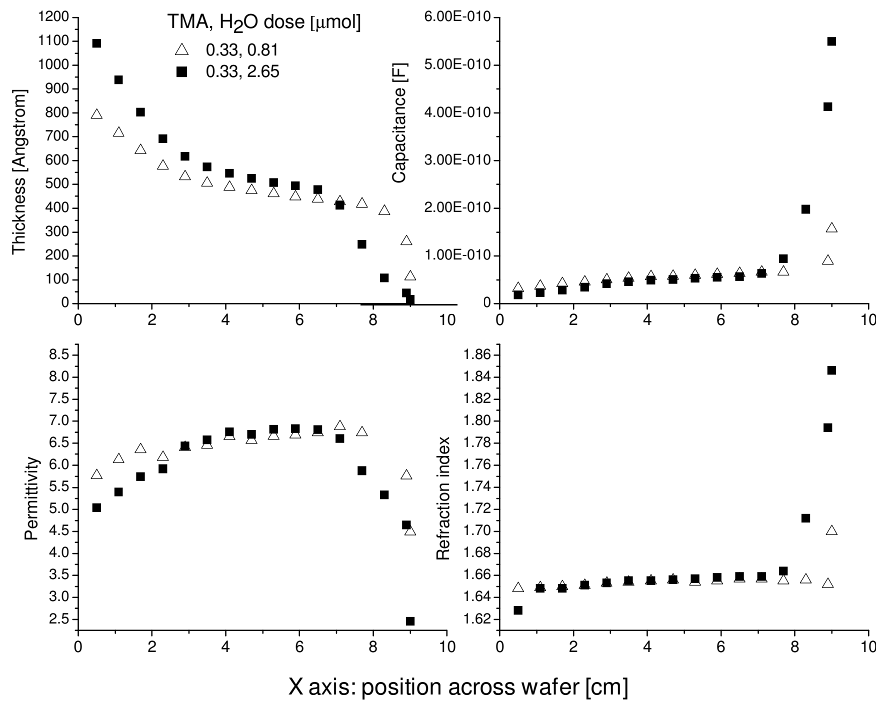

Figure 45 - Properties of two Al_2O_3 films deposited over 600 cycles under fixed TMA underdosed conditions (0.33µmol) and 2.65 µmol (solid squares) and 0.81 µmol (open triangles) water doses

relatively constant (ε_r~6.5) and the optical index is 1.65, both in good agreement with the literature.[3, 34] However, in the head and tail regions, the deviations of the GPC correspond with a degradation of the permittivity (15 to 34% decline) indicating once again that the film is intrinsically affected under the non-ideal growth conditions. We also notice that the improvement in uniformity occurring when the excess of water relative to TMA is reduced is mirrored by an optimal permittivity over a broader region (open triangles in Figure 45). The increase of the index of refraction in the tail region may seem surprising as the dielectric function is related to the complex index of refraction by the relationship $\tilde{\varepsilon} = \tilde{N}^2$. However CV measurements are done

in the kHz-MHz range vs. 1E14 Hz for ellipsometry. The different trends are likely to reflect the contribution of different polarization mechanisms, possibly ionic at lower frequency and electronic in the optical spectrum. The divergence of the refractive index may also reflect the difficulty of measuring accurately the refraction index for thin films (<200Å) as the values of tan(ψ) measured by ellipsometry exhibit a low sensitivity to refraction index variations in that region.[67]

5.3 - Surface analysis

5.3.1 Experimental

Analysis of three Al_2O_3 films deposited on 100 mm Si wafers under saturating and starved precursors conditions were undertaken using X-ray photoelectron spectroscopy (XPS) and secondary ion mass-spectrometry (SIMS). The measurements were done by staff members Lia Vanzetti (XPS) and Damiano Giubertoni (SIMS) at Fondazione Bruno Kessler, FCS Division, Trento, Italy (previously named ITC-IRST). The dose conditions for the 3 samples are summarized in Table 4.

Sample #	TMA [µmol]	H_2O [µmol]	Comments
A	6.3	3.1	Very uniform (Figure 34)
B	6.3	1.8	Water starved, non-uniform (Figure 34)
C	0.4	3.9	TMA starved, non-uniform (Figure 35)

Table 4 – Process conditions for wafers characterized by XPS and SIMS

The XPS measurements were performed on a Scienta Esca-200 instrument equipped with a monochromatized Al K_{α} (1486 eV) source. The area sampled was 1x0.2 mm^2 and a 0.4eV energy resolution was used. A fixed emission angle of 90˚, i.e., normal to the sample surface was used. In the XPS technique the sampling depth depends on the material, on the kinetic energy of the emitted electron, and on the angle between the sample normal and the analyzer axis. The sampling depth is about three times the escape depth (and with this material and in the experimental condition used probably around 10 nm).

Dynamic SIMS measurements were carried out on a Cameca SC-Ultra instrument. A Cs^+ primary ion beam at 1keV incident energy was used with a 45˚ incidence angle. This combination provides good detection limits and depth resolution. The ion beam was rastered over a 250x250 μm^2 area and the secondary electrons collected from en electronically selected 100x100 μm^2 area in the center of the crater bottom to avoid crater edge effects. The sputtering time was converted to depth by either measuring the final depth of the crater as measured by profilometry or based on the average sputtering rate measured in-situ.

5.3.2 Dynamic SIMS results

Dynamic SIMS is arguably one of the most accurate thin film analysis techniques to determine element concentration as a function of depth as the film is sputtered away at a fixed rate while measuring the secondary electrons. SIMS profiles

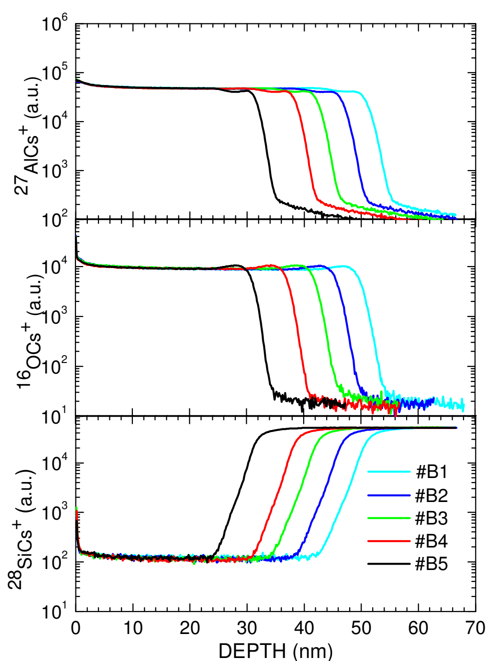

Sample B

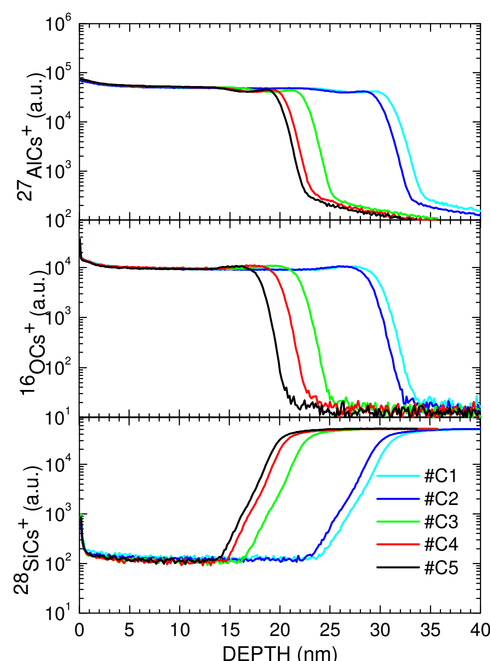

Sample C

Figure 46 – Dynamic SIMS measurements for sample B and C at 5 positions across the wafer. ^{27}Al, ^{16}O and ^{28}Si species are measured. (The transitions mark the interface from Al_2O_3 to Si and shift from left to right for samples #1 to #5)

were measured at 5 equidistant locations across the wafers. Results for oxygen, aluminum and silicon are shown in Figure 46 for samples B and C.

As expected the translation of the profiles from right (#1) to left (#5) reflects the thinning of the films across the wafer and are in good agreement with the thickness measured by ellipsometry. More importantly, we notice that for both samples the step height remain the same across the sample indicating that there is no noticeable variations of the composition as the reactants gets depleted, i.e., water in sample B and TMA in sample C.

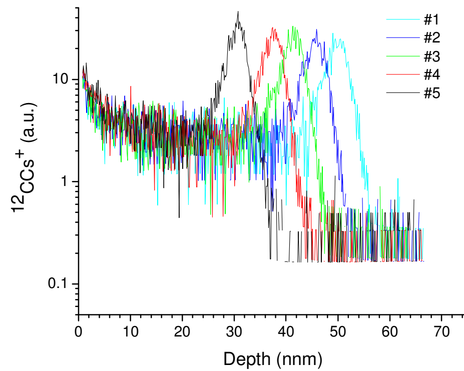

Figure 47 - SIMS measurements of carbon concentration as a function of depth a 5 locations across sample B. (samples #1 to #5 read from left to right)

It is worth noting that carbon was also detected though it appeared concentrated at the surface of the wafer and is probably due to contamination from contact with air rather than residual carbon from incomplete desorption of the methyl ligands from TMA.(Figure 47)

5.3.3 XPS measurements

For each of the 3 samples a survey in the range 2-1200 eV was acquired, to find out the elements present on the surface. Then the core levels (O 1s, C 1s, F 1s, and Al 2p) were acquired separately, and with a better energy resolution. No other elements seemed to be present on the sample surface. Table 5 show the semi-quantitative results for the elements present on the surface of sample A obtained under ideal saturating exposures. The measurements were performed at seven different points along the flow direction. The percentage of each element was calculated using the atomic sensitivity factors and does not represent the “real” content, but still is interesting to compare the four samples. The ratio O/Al is reported as well.

The ratio of oxygen to aluminum appears constant across the wafer. High carbon content was measured (~8%) which as the dynamic SIMS data indicated is

Sampling point	*O (%)*	*Al (%)*	*C(%)*	*F(%)*	*O/Al*
1	48.9	42.0	8.0	1.2	1.16
2	48.3	42.6	7.8	1.2	1.13
3	48.6	42.6	7.6	1.3	1.14
4	48.9	41.8	8.2	1.2	1.17
5	48.7	41.9	8.2	1.2	1.16
6	49.0	42.2	7.6	1.2	1.17
7	48.9	42.8	7.0	1.3	1.14

Table 5 – XPS results showing atomic percentage of elements present on the surface of sample A for 7 positions across the wafer. Ratio of oxygen to aluminium is listed in the last column.

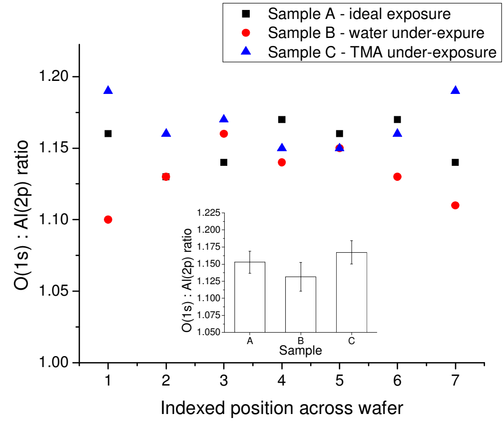

Figure 48 –O (1s) to Al (2p) ratios obtained by XPS for 7 points across the wafer for sample A, B and C. Inset histogram shows the means and ±1σ bars for the 3 samples.

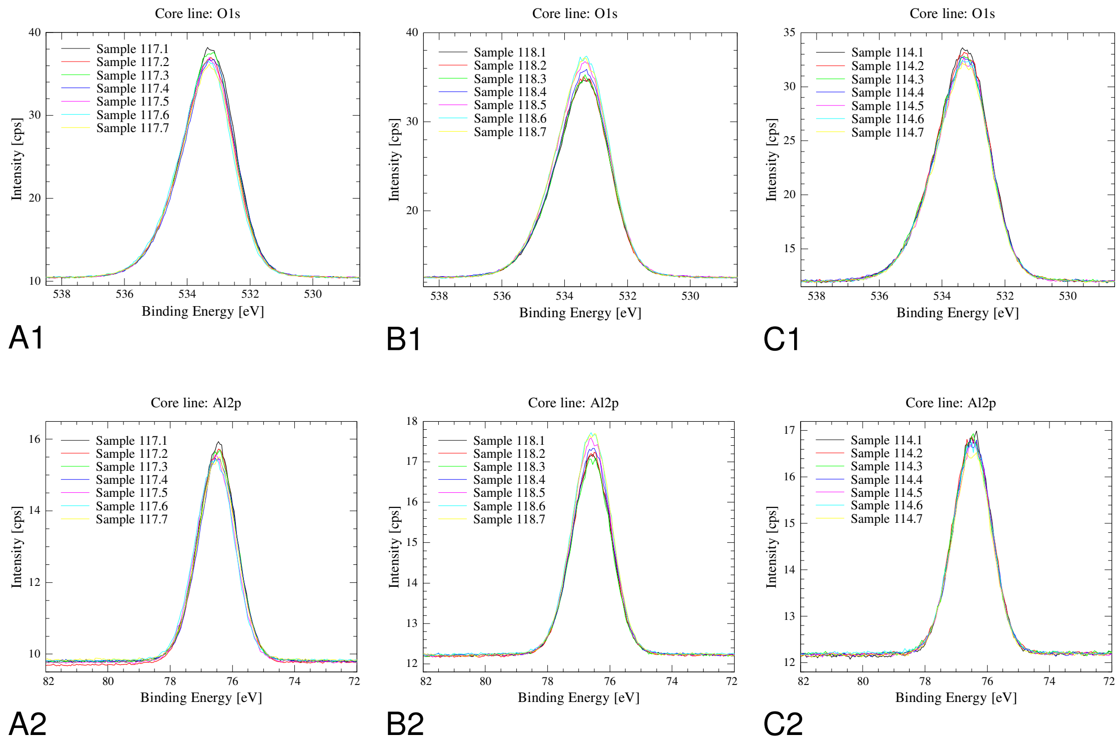

Figure 49 – XPS spectra for samples A, B and C measured at 7 locations across the wafer. First row corresponds to O(1s) peak and second row to Al(2p) peak.

likely caused by carbon contamination at the surface. The oxygen to aluminum ratios measured for the 3 samples over 7 sites across the wafer are shown in Figure 48. Though the ratio for the TMA underexposed sample is in average 3% higher than for the water underexposed sample, the variation is negligible and therefore indicates that the stoichiometry of the films is not affected by the depletion of water and TMA across the wafer.

5.4 - Conclusions

Electrical properties of Al_2O_3 films obtained from water and TMA under ideally saturating dose conditions were measured. The leakage current at 1MV/cm fields ranged in the nA/cm^2 range, in good agreement with the literature. The permittivity measured on Au/Al_2O_3/Si MOS capacitors was somewhat low (ε_r ~6.3). However by taking into consideration the presence of a 10 Å SiO_2 interfacial layer and using lift-off techniques rather than chemical wet etch, permittivity as high as 8.9 were measured.

Thickness non-uniformities caused by reactant depletion were mirrored with a 15% degradation of the permittivity across the wafer as well as with an increase of the leakage current density when the film got thinner. In an attempt to determine, the cause of this intrinsic degradation, dynamic SIMS and XPS measurements were performed to analyze the film composition and potential contamination across the depleted films. Both techniques indicate that the stoichiometry of the film remains unchanged across the wafer and no variations of contaminants such as carbon,

nitrogen or hydrogen were discernable across the wafer. Also X-ray diffraction measurements indicate that the Al_2O_3 film is amorphous as was expected from the low temperature process.

At this point we were not able to demonstrate the origin of the degradation of the permittivity along the film. However a decrease in the film density is the most likely probable cause. Indeed the permittivity of a dielectric is related to the microscopic polarization in the materials. As such, lower density translates into a decrease of the volume concentration of polarized dipoles and lower permittivity. Accurate measurements of thin film density is however difficult. X-ray reflectometry (XRR) measurements on non-uniform samples were undertaken though film density could not be extracted with sufficient accuracy to draw valid conclusions[11].

The fact that the materials properties degrade in the underdose regime as a result of reactant depletion does not provide a positive prognostic for applying this method to combinatorial materials synthesis. Indeed, if one succeeds in creating a compositionally-graded ternary film by controlling the reactant depletion across the wafer, it will be difficult in the end to deconvolute the contributions of the composition on the film properties with the degradation of the individual constituents as a result of the deposition method.

---

[11] XRR measurements were done in Prof. W.J. Lee's laboratory, Electronic Ceramic Center (ECC) in Dongeui University, Busan, Korea. An X'Pert PRO Materials Research Diffractometer(MRD) from PANalytical was used.

Chapter 6: Conclusion and Future Work

6.1 - Conclusion

In this work, a strategy exploiting the benefits of in-situ gas phase sensing in conjunction with ex-situ measurements of the film properties across 100 mm wafers was proposed to optimize the prototypical Al_2O_3 ALD process. An innovative wafer-scale reactor design was used with a small volume ALD process chamber embedded in a loadlock-configured UHV chamber and operating under cross flow conditions that mimics behaviors of larger manufacturing ALD platforms. For this work, the system was upgraded to deliver low vapor pressure reactants, i.e., $Al(CH_3)_3$ and water. Accurate control of the doses was achieved by pressure-end point control rather than adjusting the pulse time. Ozone was also implemented to compare its performance with water. A MKS Vision 1000C mass-spectrometer was integrated downstream to the reactor for in-situ chemical diagnostics.

The $Al(CH_3)_3$ / H_2O system was chosen as it is often referred to as an "ideal" ALD system due to the good reactivity and thermal stability of the precursors and the demonstrated self-limited growth under saturation conditions. As such, this system constitutes a relevant test case to demonstrate a new methodology for process optimization and investigate some of the complex physicochemical interactions that, even in the best case of the Al_2O_3 ALD chemistry, can significantly impact the ALD process performances at the wafer scale.

Downstream mass-spectrometry was first used to rapidly identify across the [H_2O x $Al(CH_3)_3$] process space the exposure conditions leading to surface saturation. Methane was identified as the primary reaction by-product. Its signature, mass-16, was integrated over half-cycle periods and used as a marker to characterize not only the state of saturation during individual cycles but also the state of nucleation retardation or overall growth metrology across the entire run. An iterative process where reactant doses were sequentially varied over a wide range of exposures was implemented to determine the onset of surface saturation over a large matrix of dose conditions. In the case of $Al(CH_3)_3$ a clear saturation behavior of adsorbed $-Al(CH_3)_2^*$ species was observed at ~3 μmol. Evaluation of the saturating conditions of $-OH^*$ groups under varying water exposure conditions proved more challenging suggesting complex saturation behaviors from the water molecules where the saturation equilibrium of the hydroxyl groups shifted upon higher water partial pressures and multilayer formation occurred.

The impact of precursor doses outside as well as inside the parameter space outlined by mass-spectrometry was then investigated by characterizing film properties across the wafer using spectroscopic ellipsometry, CV and IV electrical characterization, XPS and SIMS.

Across-wafer thickness uniformity measurements over a broad range of exposure and purge conditions depict a behavior that is inconsistent with a simple picture of ALD as alternating, fully self-limiting reactions where monolayers of complementary adsorbates pile up in compact monolayers on top of another. In that

respect, the impact of water dosage was clearly characterized by using ozone as an alternative oxidant and comparing the process performances at the wafer scale.

For TMA and water dose in the range ~3 μmol each, excellent thickness uniformity was achieved (1σ/mean<1%) at a 0.95 Å/cycle deposition rate in good agreement with literature data. In the case of TMA/ozone, an even better uniformity (~0.6%) could be achieved at a substantially lower TMA, i.e., 0.8 μmol, illustrating the high reactive efficiency of the TMA/ozone system. In both cases, under this set of ideally saturating conditions, the full benefits of ALD were realized: reproducible deposition rate at 1Å/cycle, excellent uniformity, very short nucleation delay and electrical and optical properties in agreement with literature.

Overdose of TMA or ozone did not degrade uniformity or otherwise compromise ALD performance, indicating that they both elicit self-limiting adsorption/reaction as desired in ALD. In contrast, overdosing of water caused significant (40%) growth rate increase per cycle and degradation of uniformity, to the extent that ALD provides no benefit at all in uniformity or thickness control over conventional chemical vapor deposition. The non-ideal ALD behavior in the context of high water concentration is a clear illustration of the complex physicochemical interactions that can drive ALD. Different interpretations, not exclusive with one another, were proposed. Rather the GPC increase is the result of an increased surface saturation of $–OH^*$ groups due to a shift of the adsorption equilibrium at higher water partial pressures[38, 53] or the result of a multilayer build-up of water molecules caused by hydrogen bonding, is unclear. Further investigations with more advanced

in-situ diagnostic method, e.g., transmission FTIR, would be required to determine the possible contributions.

As expected, in the under-exposure regime, depletion of TMA or water reactants resulted in increased non-uniformities and thickness gradients along the flow direction. Ozone however did not exhibit substantial degradation of the uniformity upon smaller exposures but only a uniform decrease of the GPC. As ozone is a diluted gas mixture (20% O_3 / 80% O_2), it is conceivable that the higher pulse pressure resulted in flow dynamics mitigating the effect of depletion. Interestingly our data reveal that the changing saturation behavior of water as a function of the dose did significantly impact the thickness profiles in this regime. With modest overdose of water, increasing underdose of TMA produced sharp depletion edges in the downstream portions of the wafer while piling-up material at the upstream portion of the wafer. These non-linear uniformity behaviors were attributed to increased water adsorption, depletion associated with underdose conditions for TMA, and the reactivity for TMA dose to react with the first water it experiences, and vice-versa.

These results clearly illustrate the impact of reactor design on ALD process performances. The cross-flow design magnifies non-uniformities caused by depletion thereby decorating deviations from a suitable ALD process recipe and providing a convenient feedback metric for the process optimization. The implementation of pressure-end point control for reactant doses has also important consequences, particularly in the case of water. Higher exposures, i.e., higher pressure setpoints in the delivery volume, translated into increased reactant partial pressures and

concentration across the wafer. In the case of water, this resulted in increased coverage and deposition rate (>1.0Å/cycle) even when saturation conditions had been reached. In that regard, the impact of higher water dose setpoints in our system is fundamentally different from increasing the exposure time under fixed impingement rate as commonly done in a number of ALD platforms. With the latter design, higher exposure time will not cause a change in the saturation equilibrium of water. As such, the surface coverage and deposition rate remain constant even when over-exposing the surface with water though the deposition rate will likely vary with the water vapor pressure and the flow conductance from the source to the reactor.

To a large extent, the use of ozone as an oxidant appears preferable over water. The absence of potential hydrogen bonding and the high reactivity of ozone with TMA offer clear benefits including a steady deposition rate at high ozone exposure, reduced TMA consumption by 3x factor at equivalent GPC (1Å/cycle) and uniformity (1σ/mean<1%) and faster cycle times due to more rapid purging of the excess ozone.

6.2 - Future work

Uniformity and conformality are to a large extent the gold standards to characterize the performances of an ALD process. We have showed that our cross-flow ALD system is a versatile platform to study the impact of reactant exposures and purges on thickness uniformity across a planar 2D wafer. A logical continuation of this work therefore consists in investigating how the same process metrics influence

the growth in 3D high-aspect ratio structures. This work, currently under way, looks at the conformality of TiO_2 ALD films deposited in porous anodic alumina nanotemplates. Preliminary results achieved by Erin Robertson illustrate that process conditions that lead to cross-wafer uniformity on a 2D planar wafer do not translate into conformal films in an ultra-high aspect ratio nanopore. This expected result is a direct consequence of not only the increased surface area of the 3D structures but also the transition from a viscous flow regime on the surface to a molecular flow regime in the nanopores. Understanding how precursor dose and purge time induce depletion gradients not only across the wafer but also down the length of the nanopore is a key objective of this work. Interestingly, improved conformality is achieved by increasing the residence time of the molecules in the reactor so that they can diffuse to the bottom of the pores as well as extending the purge times to allow the by-products to desorb and diffuse out of the pores. In the case of water doses, increasing the exposure will be necessary to achieve coverage down the pores. However variations of the water partial pressure along the pore may result in variations of the surface coverage under saturation and impact the conformality. As for our uniformity study, a direct comparison with ozone as an oxidant might illustrate the impact of water exposure on conformality. From a perspective of reactor design (cross-flow and dose control method), and process optimization (exposure and purge times), the investigation of the potential trade-offs between uniformity on the wafer top surface and conformality in the pores will be most interesting.

Throughout this work a number of tools and methodologies have been developed. Our ALD reactor design combines the benefits normally found in manufacturing platforms (full wafer capabilities, UHV cleanliness, advanced process control) with those found in R&D tools (process flexibility, software and hardware expandability, low cost). In combination with in-situ QMS sensing for real-time process optimization and ex-situ film characterization techniques at the wafer scale, e.g., ellipsometry, CV/IV and sheet resistance measurements, this set of tools provides a unique platform to develop new processes and applications. For example, it has been a key enabler in implementing electrostatic nanocapacitors for high energy storage applications by combining ALD-grown $TiN/Al_2O_3/TiN$ MIM structures in AAO nanotemplates.[16][12] To further improve the performance of these nanocapacitors, low resistivity (20µΩ.cm) ruthenium metal and high-K aluminum-doped TiO_2 (ε_r ~100 in rutile phase) are currently being developed on this platform, directly building on the foundations from this work.

[12] Equivalent planar capacitance of up to 100 µF.cm[2] was achieved, substantially exceeding previously reported values for nanostructures electrostatic capacitors and matching for the first time the energy density of electrochemical capacitors.

Appendices

Contributions to the design and construction of equipment described in this thesis

In 1998, I was hired by Professor G.W. Rubloff as a full-time research engineer and manager of the Laboratory for Advanced Materials Processing at UMD. In 2003, as part of my professional activities, I designed the UHV ALD tool described in Chapter 2 for a new work to be done my doctoral candidate Wei Lei. The embedded “mini-reactor” was built in the Physics Shop at the University of Maryland based on my CAD drawings shown in Appendices, Fig. I to III. The rest of the equipment (Appendices, Fig. IV) was purchased from vacuum equipment suppliers and assembled with the help of Wei Lei. I developed the Labview software platform for the control of the ALD system. In 2006, at the start of my own doctoral work, I redesigned and rebuilt the delivery system to accommodate low vapor pressure precursor sources, i.e., water and trimethlylaluminum, as well as a MKS ozone generator and a new MKS Vision 1000C mass-spectrometer.

In 2003, I also implemented and programmed the automated probe station for the measurements of electrical properties on large arrays of MOS/MIM capacitors. This equipment is still in use by members of the G.W. Rubloff group as well as external users.

Table I – Comparison of main thin film deposition techniques (CVD: chemical Vapor Deposition, MBE: Molecular beam epitaxy, PLD: Pulse laser deposition). This table does not intend to be exhaustive. The inputs are based on various sources (online, oral discussions, personal knowledge) and as such are subjective. They can vary significantly with the equipment used and the type of materials to be deposited

Method	ALD	CVD	MBE	Sputter	Evaporation	PLD
Adsorption mechanism	Chemisorption	Chemisorption	Physisorption	Physisorption	Physisorption	Physisorption
Materials	Dielectrics Metals Nitrides Semiconductor	Mainly dielectrics and few metals	III-V, II-VI	Metals and dielectrics	Metals and low melting point materials	Oxide
Thickness control	Excellent	Good	Good	Good	Good	Good
Thick. Uniformity	Excellent	Good	Good	Very good	Good	Fair
Impurity	Varies	Very low	Very low	Low	Varies	Low
Film density	Good	Good	Good	Good	Poor	Good
Step coverage	Excellent	Good	Poor	Poor	Poor	Poor
Interface quality	Good	Very good	Good	Poor	Good	Varies
Materials selection	Fair	Poor	Good	Good	Fair	Good
Grain size / crystallinity	Mainly amorphous (epitaxial possible)	1-100 nm	Epitaxial	10-100 nm	10 nm	Epitaxial
Low temperature deposition (°C)	100-400	200-1200	500-750	20-400	20-100	500-1000
Deposition rate	0.01-0.1A/s	10-100A/s	1-10 A/s	10-100 A/s (slower for dielectrics)	1-20A/s	0.1-1A/s
Industrial applicability	Good	Good	Fair	Good	Good	Poor
Vacuum quality	HV	UHV	UHV	UHV	UHV	UHV
Cost	Moderate	High	Very high	High	Moderate	Very high

Fig. I – CAD drawing: cross-section of ALD mini-reactor with cap and heater assembly.

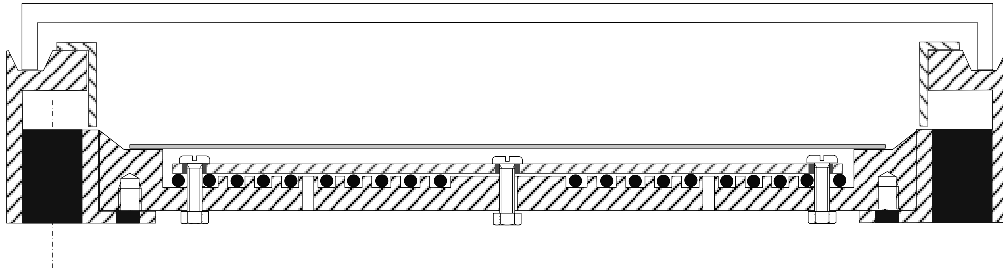

Fig. II - CAD drawings: cross-section and top view of ALD substrate heater

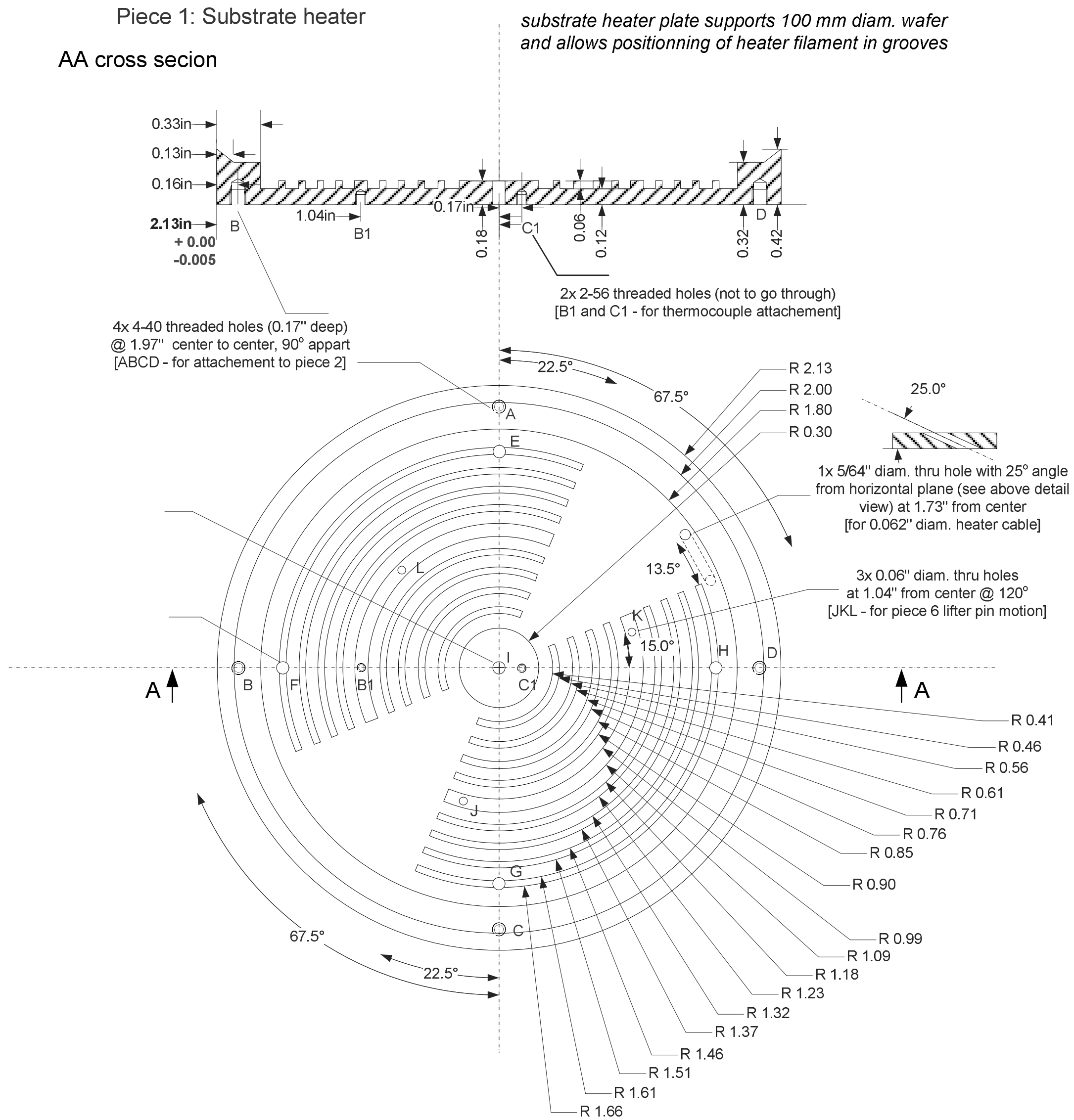

Fig. III - CAD drawings: cross-section and top view of gas inlet and outlet ring. Heater assembly is supported by this ring.

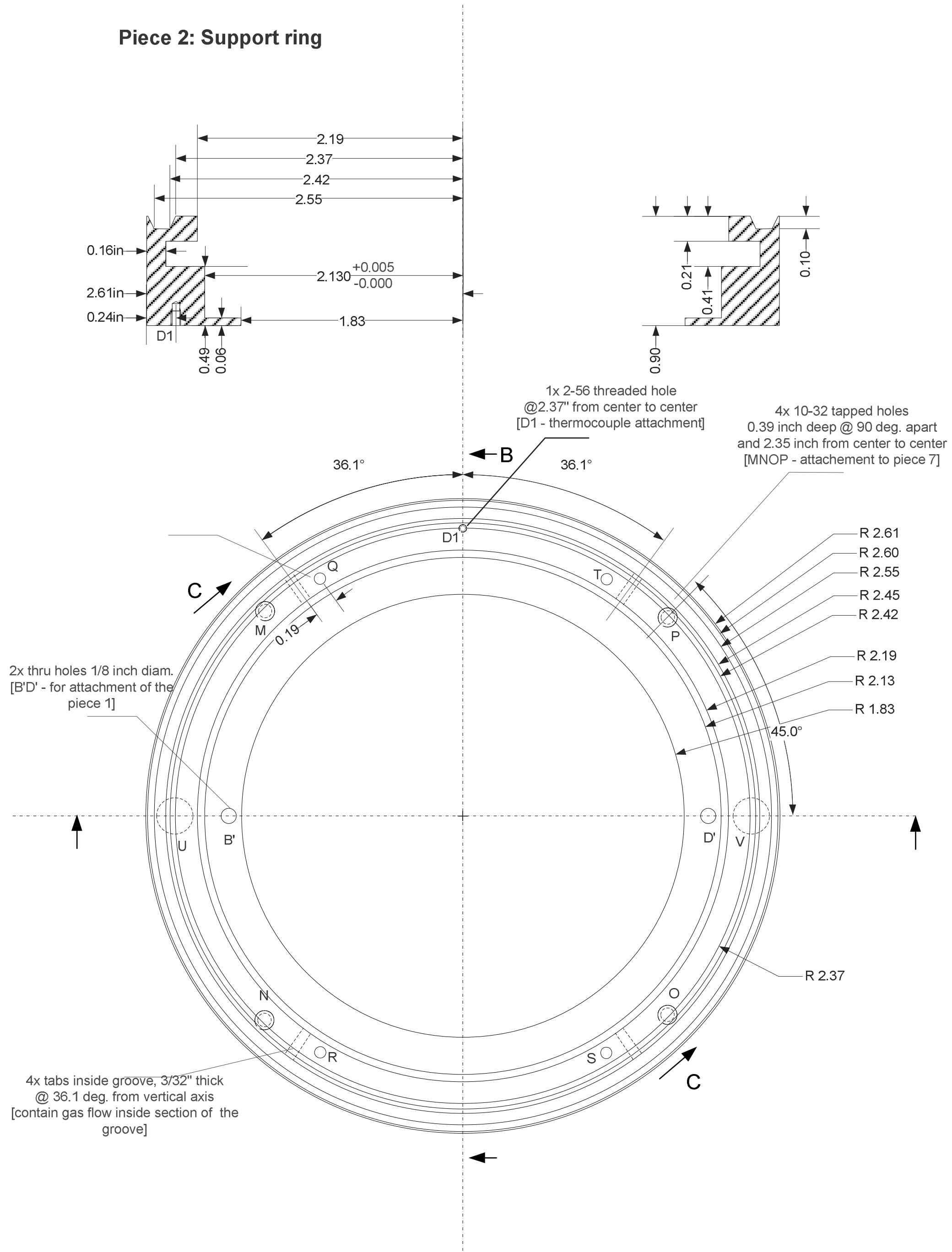

Fig. IV - CAD drawing: Side view of ALD process chamber with mini reactor, cap and actuation mechanism.

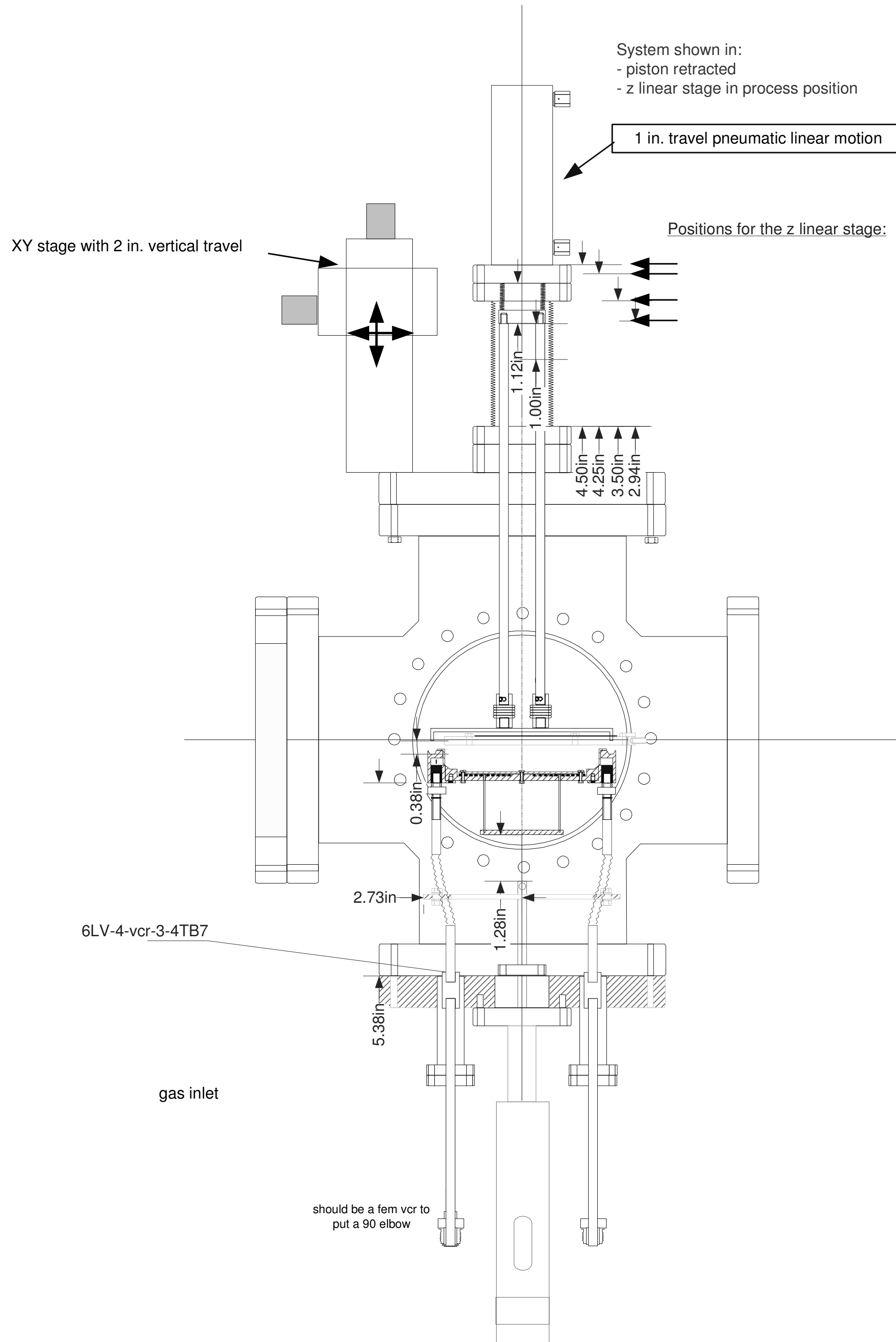

Fig. V – Calibration of ALD substrate heater as measured by 13 point thermocouple wafer. a) wafer temperature as a function of controller temperature at 100 mTorr. b) Wafer temperature as a function of pressure at 175˚C setpoint temperature.

V-a

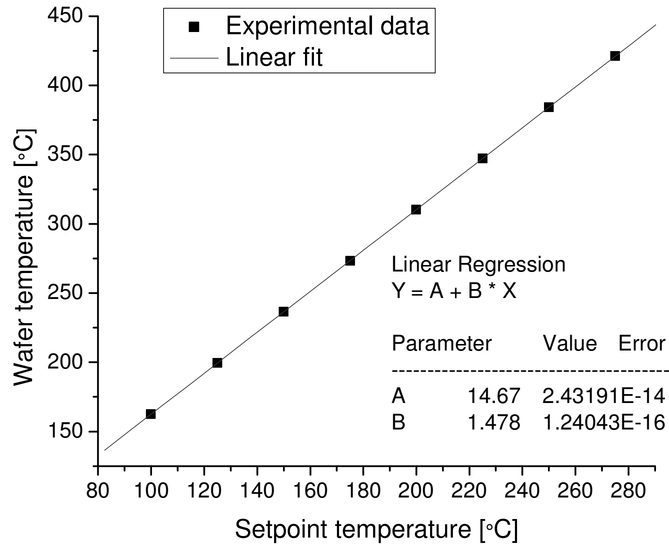

V-b

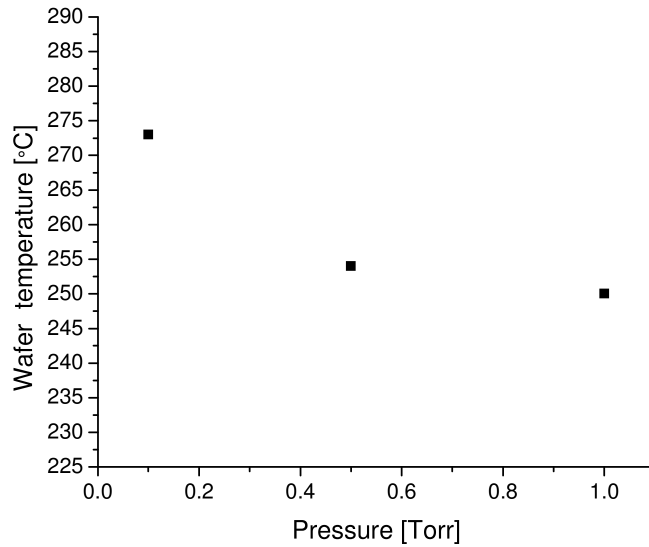

Fig. VI – Reactant vapor pressure vs. temperature for trimethylaluminum, water and titanium isopropoxide.

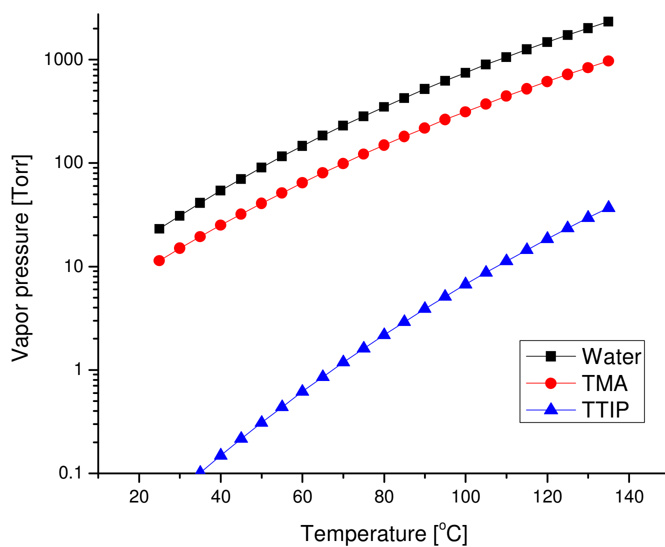

Vapor pressure laws for liquid precursors (Source: Air Liquide, France)

Water	log P [Torr] = 8.07-1730/T[K]
TMA	log P [Torr] = 8.22-2134.8/T [K]
TTIP	log P [Torr] = 9.465-3222/T [K]

Fig. VII – Schematics of MKS Vision 1000C mass-spectrometer. Dimensions are given in inches. (Source: User manual, LP101012 Revision 1.01, MKS Instruments, Spectra Products, 2002)

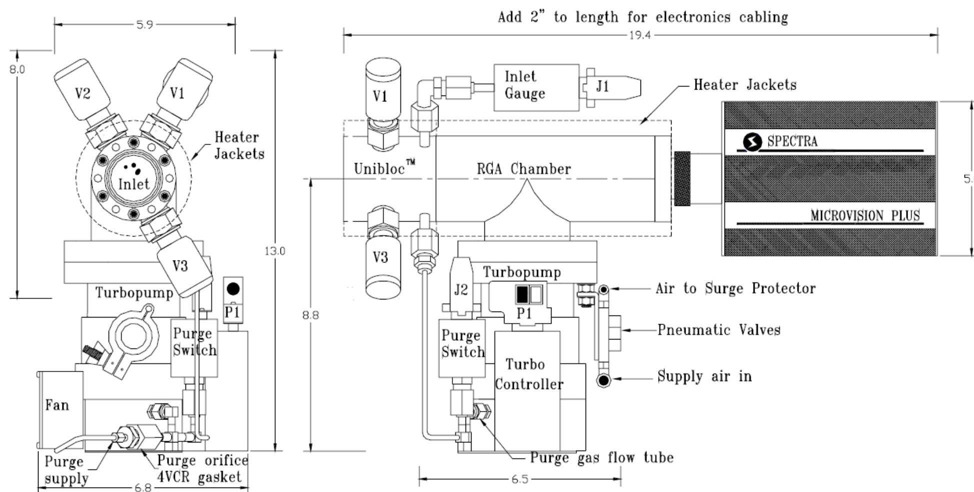

Fig. VIII – Schematic of orifice configuration for QMS differential pumping (Source: User manual, LP101012 Revision 1.01, MKS Instruments, Spectra Products, 2002)

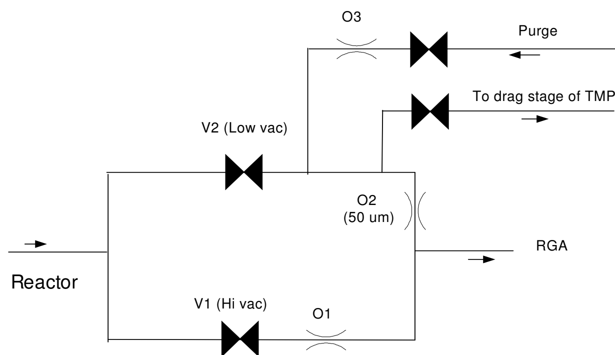

Fig. IX – LabView user interface for CV/IV probe station.

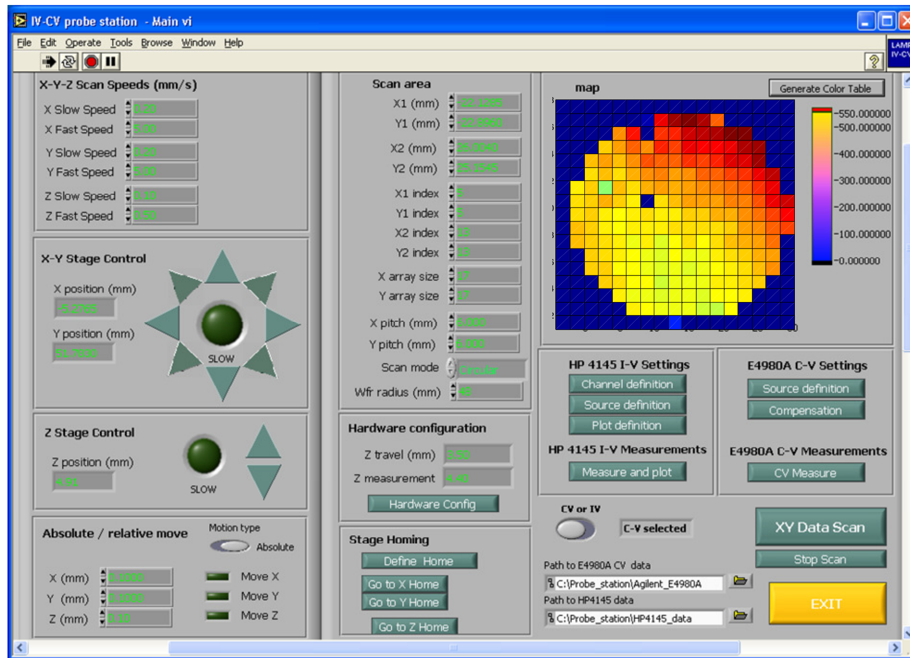

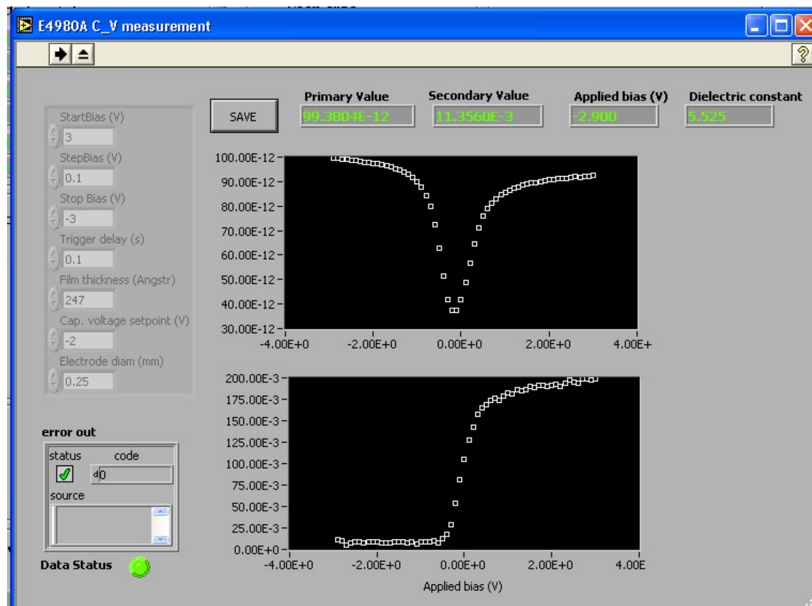

Fig. X – Comparison of electrical performances for 12 nm Al_2O_3 film deposited at 275˚C on p-doped Silicon with $Al(CH_3)_3$ and ozone under saturating conditions. The MOS capacitors were fabricated by four distincts methods: I : lift-off and gold thermal evaporation, II: lift-off and aluminum thermal evaporation, III: aluminum thermal evaporation and wet chemical etch (Transene D type), IV: gold thermal evaporation and gold wet chemical etch (Transene TFA type)

Fabrication method	Permittivity ε_r	Current density at 1MV/cm [nA/cm^2]	Breakdown field [MV/cm]
Liftoff/Au	9.2+/-0.04	22+/-10	9+/-0.5
Liftoff/Al	8.6 +/-0.06	29+/-11	8+/-1
Wet etch/Al	6.9+/-0.1	22+/-5	8.5+/-2
Wet etch/ Au	6.7+/-0.04	17+/-12	9.5+/-0.5

Fig. XI – Operating procedure for image reversal and lift-off process using AZ 5214E photoresist.

- Dehydration bake of sample at 120°C for 10 min. *Let sample cool (~ 5 minutes)*
- Spin AZ5214E at 3000 rpm for 60s (1.6 µm thickness).
- Soft bake at 100°C for 60s
- UV exposure (34 mJ/cm²)
    - The exposure time will depend on the mask-aligner used.
    - The type of mask (chrome vs Mylar transparency) also should be taken into consideration when determining the exposure time. Use bright field mask.
- Critical step: Hard bake at exactly 120°C for 45s. *Exposed PR cross-links and becomes non-soluble (negative tone behavior)*
- Flood exposure at >200 mJ/cm² without mask so that non-exposed PR becomes soluble
- Develop in AZ400K 1:4 water for 60s (4 parts water, 1 part AZ400k developer)
- Deposit metal layer. *Be careful with metal quality and adhesion to the sub straight to insure clean lift-off*
- Liftoff in sonic bath with acetone. *Do pulses of 10s repeatedly until you notice the top metalization layer completely removed. If there is uncharacteristic delamination or peeling of the bottom films, stop. Remember to use clean acetone for each sample to insure clean a sample.*

<u>Principle of image reversal with AZ5214E</u>

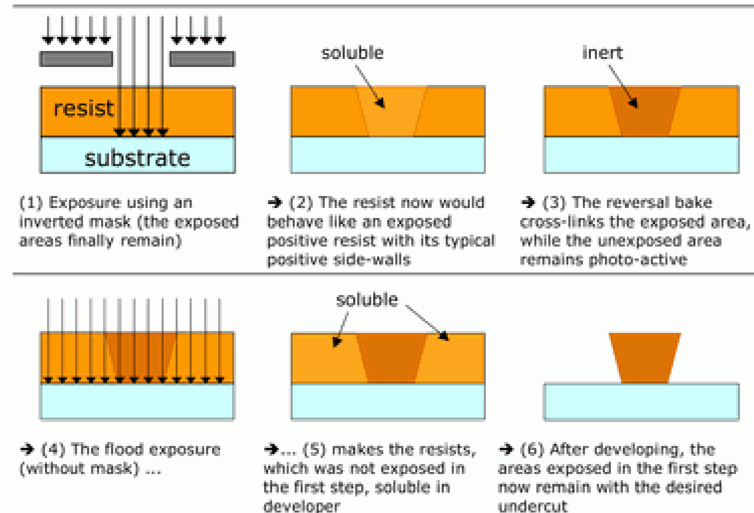

Source:http://www.microchemicals.com/photoresist/photoresist_image_reversal_resists_eng.html

Fig. XII – 5” chrome mask layout for capacitor fabrication on 100 mm diameter wafer. Each set include 3 capacitor shapes (circular, square, crenel) and 4 surface areas (0.1962, 0.0491, 0.0078, 0.0019 mm^2). The mask is bright field. Hatched sections come out opaque, black sections come out transparent.

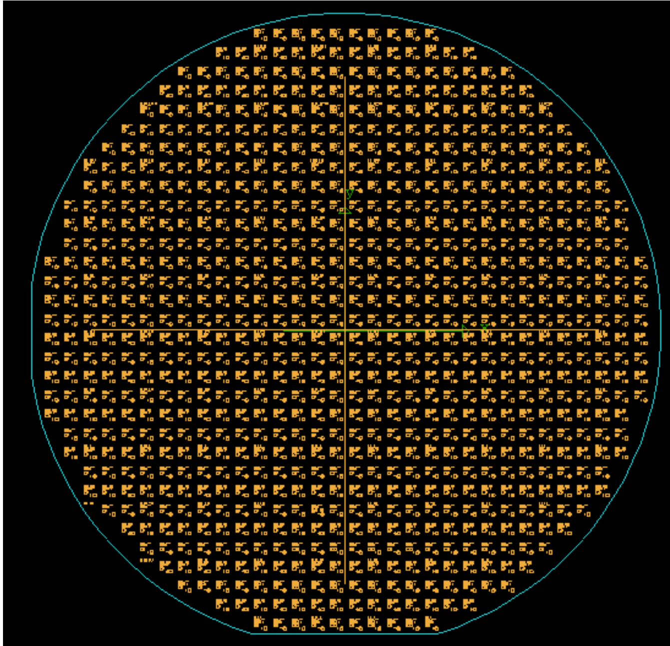

Details of one set of capacitors (row 21, column 31). Some key dimensions are in green (not part of actual mask)

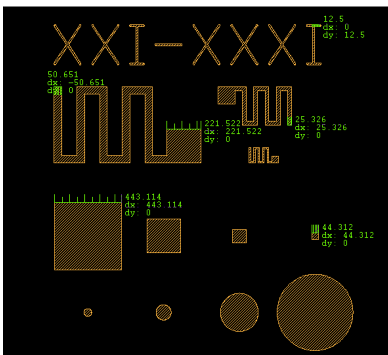

Fig. XIII – Summary table of CV and IV measurements done on 10nm Al_2O_3 dielectrics deposited from either TMA/water or TMA/ozone. MOS capacitors ($Si/Al_2O_3/Au$) and MIM ($Si/Ti/Pt/Al_2O_3/Au$) were fabricated using Shipley 1813 photoresist patterned with UV lithography followed by a Transene gold wet etch.

Capacitor type	Substrate	Process chemistry	Permittivity	Breakdown [MV/cm]	Current density at 1MV/cm [A/cm^2]
MOS	Si	TMA/H_2O	7.5	7.8	2.5E-7
MOS	Si	TMA/O_3	7.5	8.3	2.3E-7
MIM	Pt	TMA/H_2O	8.4	6.8	8E-8
MIM	Pt	TMA/O_3	8.7	7.1	7.5E-8

Fig. XIV – Model showing impact of SiO_2 interfacial layer on Al_2O_3 film capacitance as a function of Al_2O_3 film thickness. For example, a 5 Å interfacial layer at the interface of a 100Å Al_2O_3 film will lower the capacitance by ~11% (dashed lines).

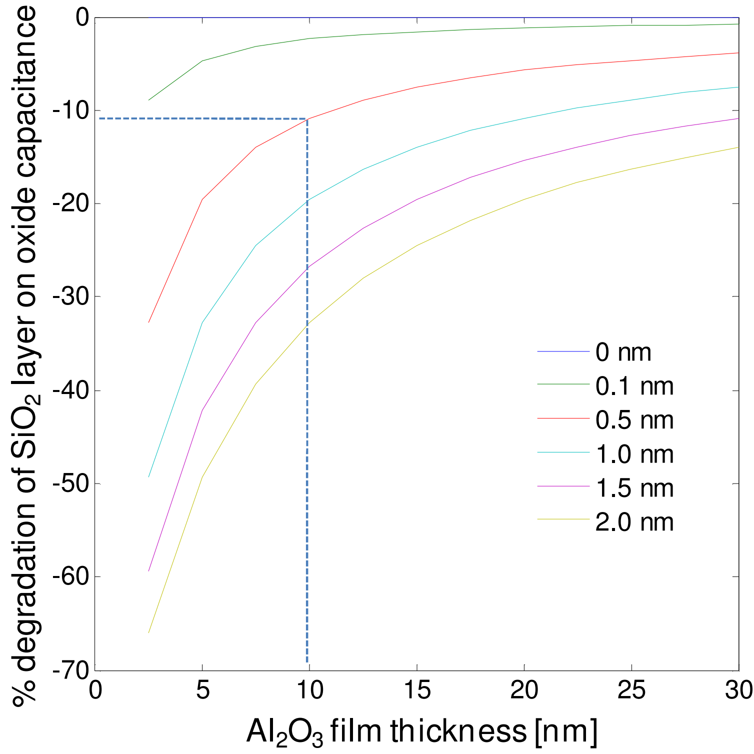

List of publications as of Nov. 2009

[1] P. Banerjee, I. Perez, L. Henn-Lecordier, S. B. Lee, and G. W. Rubloff, " ALD based Metal-insulator-metal (MIM) Nanocapacitors for Energy Storage," *ECS Transactions,* vol. 25 (4) pp. 345-353, 2009.

[2] P. Banerjee, I. Perez, L. Henn-Lecordier, S. B. Lee, and G. W. Rubloff, "Nanotubular metal-insulator-metal capacitor arrays for energy storage," *Nature Nanotechnology,* vol. 4, pp. 292-296, 2009.

[3] I. Perez, E. Robertson, P. Banerjee, L. Henn-Lecordier, S. J. Son, S. B. Lee, and G. W. Rubloff, "TEM-based metrology for HfO2 layers and nanotubes formed in anodic aluminum oxide nanopore structures," *Small,* vol. 4, pp. 1223-1232, 2008.

[4] L. Henn-Lecordier, W. Lei, M. Anderle, and G. W. Rubloff, "Real-time sensing and metrology for atomic layer deposition processes and manufacturing," *Journal of Vacuum Science & Technology B,* vol. 25, pp. 130-139, 2007.

[5] Y. Cai, L. Henn-Lecordier, G. W. Rubloff, R. Sreenivasan, J. O. Choo, and R. A. Adomaitis, "Multiplexed mass spectrometry for real-time sensing in a spatially programmable chemical vapor deposition reactor," *Journal of Vacuum Science & Technology B,* vol. 25, pp. 1288-1297, 2007.

[6] W. Lei, L. Henn-Lecordier, M. Anderle, G. W. Rubloff, M. Barozzi, and M. Bersani, "Real-time observation and optimization of tungsten atomic layer deposition process cycle," *Journal of Vacuum Science & Technology B,* vol. 24, pp. 780-789, 2006.

[7] J. O. Choo, R. A. Adomaitis, G. W. Rubloff, L. Henn-Lecordier, and Y. J. Liu, "Simulation-based design and experimental evaluation of a spatially controllable CVD reactor," *Aiche Journal,* vol. 51, pp. 572-584, 2005.

[8] J. O. Choo, R. A. Adomaitis, L. Henn-Lecordier, Y. Cai, and G. W. Rubloff, "Development of a spatially controllable chemical vapor deposition reactor with combinatorial processing capabilities," *Review of Scientific Instruments,* vol. 76, 2005.

[9] L. Henn-Lecordier, J. N. Kidder, and G. W. Rubloff, "Real-time acoustic sensing and control of metalorganic chemical vapor deposition precursor concentrations delivered from solid phase sources," *Journal of Vacuum Science & Technology A,* vol. 22, pp. 1984-1991, 2004.

[10] S. Cho, L. Henn-Lecordier, Y. J. Liu, and G. W. Rubloff, "In situ mass spectrometry in a 10 Torr W chemical vapor deposition process for film thickness metrology and real-time advanced process control," *Journal of Vacuum Science & Technology B,* vol. 22, pp. 880-887, 2004.

[11] L. Henn-Lecordier, J. N. Kidder, G. W. Rubloff, C. A. Gogol, and A. Wajid, "Real-time, in situ film thickness metrology in a 10 Torr W chemical vapor deposition process using an acoustic sensor," *Journal of Vacuum Science & Technology B,* vol. 21, pp. 1055-1063, 2003.

[12] Y. Xu, T. Gougousi, L. Henn-Lecordier, Y. Liu, S. Cho, and G. W. Rubloff, "Thickness metrology and end point control in W chemical vapor deposition

process from SiH4/WF6 using in situ mass spectrometry," *Journal of Vacuum Science & Technology B,* vol. 20, pp. 2351-2360, 2002.

[13] L. Henn-Lecordier, J. N. Kidder, G. W. Rubloff, C. A. Gogol, and A. Wajid, "Real-time growth rate metrology for a tungsten chemical vapor deposition process by acoustic sensing," *Journal of Vacuum Science & Technology A,* vol. 19, pp. 621-626, 2001.

List of upcoming publications based on present dissertation

[1] L. Henn-Lecordier, M. Anderle, G.W. Rubloff, "Ozone vs. water, wafer-scale impact of oxidant selection on process performances in cross-flow atomic layer deposition", to be submitted in Chemical Vapor Deposition

[2] L. Henn-Lecordier, M. Anderle, G.W. Rubloff, "Novel in-situ methodology for process optimization in atomic layer deposition", to be submitted in Chemical Vapor Deposition

Bibliography

[1] M. Leskela and M. Ritala, "Atomic layer deposition (ALD): from precursors to thin film structures," *Thin Solid Films,* vol. 409, pp. 138-146, 2002.

[2] L. Niinisto, J. Paivasaari, J. Niinisto, M. Putkonen, and M. Nieminen, "Advanced electronic and optoelectronic materials by Atomic Layer Deposition: An overview with special emphasis on recent progress in processing of high-k dielectrics and other oxide materials," *Physica Status Solidi a-Applied Research,* vol. 201, pp. 1443-1452, May 2004.

[3] R. L. Puurunen, "Surface chemistry of atomic layer deposition: A case study for the trimethylaluminum/water process," *Journal of Applied Physics,* vol. 97, p. 52, Jun 2005.

[4] O. Sneh, R. B. Clark-Phelps, A. R. Londergan, J. Winkler, and T. E. Seidel, "Thin film atomic layer deposition equipment for semiconductor processing," *Thin Solid Films,* vol. 402, pp. 248-261, Jan 2002.

[5] D. R. G. Mitchell, D. J. Attard, K. S. Finnie, G. Triani, C. J. Barbe, C. Depagne, and J. R. Bartlett, "TEM anti ellipsometry studies of nanolaminate oxide films prepared using atomic layer deposition," *Applied Surface Science,* vol. 243, pp. 265-277, 2005.

[6] T. Suntola and J. Hyvarinen, "Atomic Layer Epitaxy," *Annual Review of Materials Science,* vol. 15, pp. 177-195, 1985.

[7] International Technology Roadmap for Semiconductors 2003 Edition: Metrology, International Sematech, Austin, TX, 2003.

[8] J. Robertson, "High dielectric constant gate oxides for metal oxide Si transistors," *Reports on Progress in Physics,* vol. 69, pp. 327-396, 2006.

[9] "A 45nm Logic Technology with High-k+Metal Gate Transistors, Strained Silicon, 9 Cu Interconnect Layers, 193nm Dry Patterning, and 100% Pb-free Packaging, URL: http://download.intel.com/technology/IEDM2007/HiKMG_paper.pdf," Intel Corporation, 2006.

[10] E. Gerritsen, N. Emonet, C. Caillat, N. Jourdan, M. Piazza, D. Fraboulet, B. Boeck, A. Berthelot, S. Smith, and P. Mazoyer, "Evolution of materials technology for stacked-capacitors in 65 nm embedded-DRAM," *Solid-State Electronics,* vol. 49, pp. 1767-1775, 2005.

[11] N. D. Hoivik, J. W. Elam, R. J. Linderman, V. M. Bright, S. M. George, and Y. C. Lee, "Atomic layer deposited protective coatings for micro-electromechanical systems," *Sensors and Actuators a-Physical,* vol. 103, pp. 100-108, Jan 2003.

[12] C. F. Herrmann, F. W. DelRio, D. C. Miller, S. M. George, V. M. Bright, J. L. Ebel, R. E. Strawser, R. Cortez, and K. D. Leedy, "Alternative dielectric films for rf MEMS capacitive switches deposited using atomic layer deposited Al2O3/ZnO alloys," *Sensors and Actuators a-Physical,* vol. 135, pp. 262-272, Mar 2007.

[13] T. M. Mayer, J. W. Elam, S. M. George, P. G. Kotula, and R. S. Goeke, "Atomic-layer deposition of wear-resistant coatings for microelectromechanical devices," *Applied Physics Letters,* vol. 82, pp. 2883-2885, Apr 2003.
[14] C. Nistorica, J. F. Liu, I. Gory, G. D. Skidmore, F. M. Mantiziba, B. E. Gnade, and J. Kim, "Tribological and wear studies of coatings fabricated by atomic layer deposition and by successive ionic layer adsorption and reaction for microelectromechanical devices," *Journal of Vacuum Science & Technology A,* vol. 23, pp. 836-840, Jul-Aug 2005.
[15] T. W. Scharf, S. V. Prasad, M. T. Dugger, P. G. Kotula, R. S. Goeke, and R. K. Grubbs, "Growth, structure, and tribological behavior of atomic layer-deposited tungsten disulphide solid lubricant coatings with applications to MEMS," *Acta Materialia,* vol. 54, pp. 4731-4743, Oct 2006.
[16] P. Banerjee, I. Perez, L. Henn-Lecordier, S. B. Lee, and G. W. Rubloff, "Nanotubular metal-insulator-metal capacitor arrays for energy storage," *Nature Nanotechnology,* vol. 4, pp. 292-296, 2009.
[17] Q. Fu and T. Wagner, "Interaction of nanostructured metal overlayers with oxide surfaces," *Surface Science Reports,* vol. 62, pp. 431-498, Nov 2007.
[18] J. S. King, A. Wittstock, J. Biener, S. O. Kucheyev, Y. M. Wang, T. F. Baumann, S. K. Giri, A. V. Hamza, M. Baeumer, and S. F. Bent, "Ultralow loading Pt nanocatalysts prepared by atomic layer deposition on carbon aerogels," *Nano Letters,* vol. 8, pp. 2405-2409, Aug 2008.
[19] S. T. Christensen, J. W. Elam, F. A. Rabuffetti, Q. Ma, S. J. Weigand, B. Lee, S. Seifert, P. C. Stair, K. R. Poeppelmeier, M. C. Hersam, and M. J. Bedzyk, "Controlled Growth of Platinum Nanoparticles on Strontium Titanate Nanocubes by Atomic Layer Deposition," *Small,* vol. 5, pp. 750-757, 2009.
[20] J. D. Ferguson, A. W. Weimer, and S. M. George, "Atomic layer deposition of ultrathin and conformal Al2O3 films on BN particles," *Thin Solid Films,* vol. 371, pp. 95-104, Aug 2000.
[21] J. W. Elam, D. Routkevitch, P. P. Mardilovich, and S. M. George, "Conformal coating on ultrahigh-aspect-ratio nanopores of anodic alumina by atomic layer deposition," *Chemistry of Materials,* vol. 15, pp. 3507-3517, Sep 2003.
[22] J. S. Lee, B. Min, K. Cho, S. Kim, J. Park, Y. T. Lee, N. S. Kim, M. S. Lee, S. O. Park, and J. T. Moon, "Al2O3 nanotubes and nanorods fabricated by coating and filling of carbon nanotubes with atomic-layer deposition," *Journal of Crystal Growth,* vol. 254, pp. 443-448, Jul 2003.
[23] A. Javey, J. Guo, D. B. Farmer, Q. Wang, D. W. Wang, R. G. Gordon, M. Lundstrom, and H. J. Dai, "Carbon nanotube field-effect transistors with integrated ohmic contacts and high-k gate dielectrics," *Nano Letters,* vol. 4, pp. 447-450, Mar 2004.
[24] A. Javey, H. Kim, M. Brink, Q. Wang, A. Ural, J. Guo, P. McIntyre, P. McEuen, M. Lundstrom, and H. J. Dai, "High-kappa dielectrics for advanced carbon-nanotube transistors and logic gates," *Nature Materials,* vol. 1, pp. 241-246, 2002.

[25] M. Kemell, V. Pore, J. Tupala, M. Ritala, and M. Leskela, "Atomic layer deposition of nanostructured TiO2 photocatalysts via template approach," *Chemistry of Materials,* vol. 19, pp. 1816-1820, 2007.
[26] B. K. Lee, S. Y. Park, H. C. Kim, K. Cho, E. M. Vogel, M. J. Kim, R. M. Wallace, and J. Y. Kim, "Conformal Al2O3 dielectric layer deposited by atomic layer deposition for graphene-based nanoelectronics," *Applied Physics Letters,* vol. 92, 2008.
[27] Y. Xuan, Y. Q. Wu, T. Shen, M. Qi, M. A. Capano, J. A. Cooper, and P. D. Ye, "Atomic-layer-deposited nanostructures for graphene-based nanoelectronics," *Applied Physics Letters,* vol. 92, 2008.
[28] A. C. Jones, H. C. Aspinall, P. R. Chalker, R. J. Potter, K. Kukli, A. Rahtu, M. Ritala, and M. Leskela, "Some recent developments in the MOCVD and ALD of high-kappa dielectric oxides," *Journal of Materials Chemistry,* vol. 14, pp. 3101-3112, 2004.
[29] B. S. Lim, A. Rahtu, and R. G. Gordon, "Atomic layer deposition of transition metals," *Nature Materials,* vol. 2, pp. 749-754, Nov 2003.
[30] M. J. Cho, H. B. Park, J. Park, C. S. Hwang, J. C. Lee, S. J. Oh, J. Jeong, K. S. Hyun, H. S. Kang, Y. W. Kim, and J. H. Lee, "Thermal annealing effects on the structural and electrical properties of HfO2/Al2O3 gate dielectric stacks grown by atomic layer deposition on Si substrates," *Journal of Applied Physics,* vol. 94, pp. 2563-2571, Aug 2003.
[31] J. W. Elam, M. D. Groner, and S. M. George, "Viscous flow reactor with quartz crystal microbalance for thin film growth by atomic layer deposition," *Review of Scientific Instruments,* vol. 73, pp. 2981-2987, Aug 2002.
[32] M. M. Frank, G. D. Wilk, D. Starodub, T. Gustafsson, E. Garfunkel, Y. J. Chabal, J. Grazul, and D. A. Muller, "HfO2 and Al2O3 gate dielectrics on GaAs grown by atomic layer deposition," *Applied Physics Letters,* vol. 86, p. 3, Apr 2005.
[33] L. G. Gosset, J. F. Damlencourt, O. Renault, D. Rouchon, P. Holliger, A. Ermolieff, I. Trimaille, J. J. Ganem, F. Martin, and M. N. Semeria, "Interface and material characterization of thin Al2O3 layers deposited by ALD using TMA/H2O," *Journal of Non-Crystalline Solids,* vol. 303, pp. 17-23, May 2002.
[34] M. D. Groner, J. W. Elam, F. H. Fabreguette, and S. M. George, "Electrical characterization of thin Al2O3 films grown by atomic layer deposition on silicon and various metal substrates," *Thin Solid Films,* vol. 413, pp. 186-197, Jun 2002.
[35] M. D. Groner, F. H. Fabreguette, J. W. Elam, and S. M. George, "Low-temperature Al2O3 atomic layer deposition," *Chemistry of Materials,* vol. 16, pp. 639-645, Feb 2004.
[36] M. Juppo, A. Rahtu, M. Ritala, and M. Leskela, "In situ mass spectrometry study on, surface reactions in atomic layer deposition of Al2O3 thin films from trimethylaluminum and water," *Langmuir,* vol. 16, pp. 4034-4039, 2000.
[37] J. B. Kim, D. R. Kwon, K. Chakrabarti, C. Lee, K. Y. Oh, and J. H. Lee, "Improvement in Al2O3 dielectric behavior by using ozone as an oxidant for

the atomic layer deposition technique," *Journal of Applied Physics,* vol. 92, pp. 6739-6742, Dec 2002.

[38] R. Matero, A. Rahtu, M. Ritala, M. Leskela, and T. Sajavaara, "Effect of water dose on the atomic layer deposition rate of oxide thin films," *Thin Solid Films,* vol. 368, pp. 1-7, Jun 2000.

[39] A. Rahtu, T. Alaranta, and M. Ritala, "In situ quartz crystal microbalance and quadrupole mass spectrometry studies of atomic layer deposition of aluminum oxide from trimethylaluminum and water," *Langmuir,* vol. 17, pp. 6506-6509, Oct 2001.

[40] S. J. Yun, K. H. Lee, J. Skarp, H. R. Kim, and K. S. Nam, "Dependence of atomic layer-deposited Al2O3 films characteristics on growth temperature and Al precursors of Al(CH3)3 and AlCl3," *Journal of Vacuum Science & Technology a-Vacuum Surfaces and Films,* vol. 15, pp. 2993-2997, Nov-Dec 1997.

[41] A. Sherman, *Atomic layer deposition for nanotechnology*, 1st ed.: Ivoryton Press, 2008.

[42] A. C. Dillon, A. W. Ott, J. D. Way, and S. M. George, "Surface chemistry of Al2O3 deposition using Al(CH3)3 and H2O in a binary reaction sequence," *Surface Science,* vol. 322, pp. 230-242, Jan 1995.

[43] M. Houssa, "High-K gate dielectrics," in *Materials Science and Engineering*, M. J. G. B. Cantor, Ed. Bristol: Institute of Physics Publishing, 2004.

[44] M. L. Green, M. Y. Ho, B. Busch, G. D. Wilk, T. Sorsch, T. Conard, B. Brijs, W. Vandervorst, P. I. Raisanen, D. Muller, M. Bude, and J. Grazul, "Nucleation and growth of atomic layer deposited HfO2 gate dielectric layers on chemical oxide (Si-O-H) and thermal oxide (SiO2 or Si-O-N) underlayers," *Journal of Applied Physics,* vol. 92, pp. 7168-7174, 2002.

[45] O. Sneh, M. A. Cameron, and S. M. George, "Adsorption and desorption kinetics of H2O on a fully hydroxylated SiO2 surface," *Surface Science,* vol. 364, pp. 61-78, Aug 10 1996.

[46] A. C. Jones, H. C. Aspinall, R. R. Chalker, R. J. Potter, K. Kukli, A. Rahtu, M. Ritala, and M. Leskela, "Recent developments in the MOCVD and ALD of rare earth oxides and silicates," *Materials Science and Engineering B-Solid State Materials for Advanced Technology,* vol. 118, pp. 97-104, 2005.

[47] J. I. Skarp, P. J. Soininen, and P. T. Soininen, "ALE-reactor for large area depositions," *Applied Surface Science,* vol. 112, pp. 251-254, 1997.

[48] M. Ylilammi, "Mass-transport in atomic layer deposition carrier gas reactors," *Journal of the Electrochemical Society,* vol. 142, pp. 2474-2479, 1995.

[49] K. E. Elers, T. Blomberg, M. Peussa, B. Aitchison, S. Haukka, and S. Marcus, "Film uniformity in atomic layer deposition," *Chemical Vapor Deposition,* vol. 12, pp. 13-24, 2006.

[50] J. Kim, K. Chakrabarti, J. Lee, K. Y. Oh, and C. Lee, "Effects of ozone as an oxygen source on the properties of the Al2O3 thin films prepared by atomic layer deposition," *Materials Chemistry and Physics,* vol. 78, pp. 733-738, 2003.

[51] H. Siimon and J. Aarik, "Thickness profiles of thin films caused by secondary reactions in flow-type atomic layer deposition reactors," *Journal of Physics D-Applied Physics,* vol. 30, pp. 1725-1728, 1997.
[52] G. S. Higashi and C. G. Fleming, "Sequential surface chemical-reaction limited growth of high quality Al2O3 dielectrics," *Applied Physics Letters,* vol. 55, pp. 1963-1965, Nov 1989.
[53] R. Kuse, M. Kundu, T. Yasuda, N. Miyata, and A. Toriumi, "Effect of precursor concentration in atomic layer deposition of Al2O3," *Journal of Applied Physics,* vol. 94, pp. 6411-6416, Nov 2003.
[54] M. Y. Li, Y. Y. Chang, H. C. Wu, C. S. Huang, J. C. Chen, J. L. Lue, and S. M. Chang, "Effect of process pressure on atomic layer deposition of Al2O3," *Journal of the Electrochemical Society,* vol. 154, pp. H967-H972, 2007.
[55] M. Ylilammi, "Monolayer thickness in atomic layer deposition," *Thin Solid Films,* vol. 279, pp. 124-130, 1996.
[56] L. Henn-Lecordier, W. Lei, M. Anderle, and G. W. Rubloff, "Real-time sensing and metrology for atomic layer deposition processes and manufacturing," *Journal of Vacuum Science & Technology B,* vol. 25, pp. 130-139, 2007.
[57] W. Lei, L. Henn-Lecordier, M. Anderle, G. W. Rubloff, M. Barozzi, and M. Bersani, "Real-time observation and optimization of tungsten atomic layer deposition process cycle," *Journal of Vacuum Science & Technology B,* vol. 24, pp. 780-789, 2006.
[58] S. D. Elliott, G. Scarel, C. Wiemer, M. Fanciulli, and G. Pavia, "Ozone-based atomic layer deposition of alumina from TMA: Growth, morphology, and reaction mechanism," *Chemistry of Materials,* vol. 18, pp. 3764-3773, 2006.
[59] S. C. Ha, E. Choi, S. H. Kim, and J. S. Roh, "Influence of oxidant source on the property of atomic layer deposited Al2O3 on hydrogen-terminated Si substrate," *Thin Solid Films,* vol. 476, pp. 252-257, 2005.
[60] D. N. Goldstein, J. A. McCormick, and S. M. George, "Al2O3 Atomic Layer Deposition with Trimethylaluminum and Ozone Studied by in Situ Transmission FTIR Spectroscopy and Quadrupole Mass Spectrometry," *Journal of Physical Chemistry C,* vol. 112, pp. 19530-19539, Dec 2008.
[61] L. Henn-Lecordier, J. N. Kidder, and G. W. Rubloff, "Real-time acoustic sensing and control of metalorganic chemical vapor deposition precursor concentrations delivered from solid phase sources," *Journal of Vacuum Science & Technology A,* vol. 22, pp. 1984-1991, Sep-Oct 2004.
[62] L. Henn-Lecordier, J. N. Kidder, G. W. Rubloff, C. A. Gogol, and A. Wajid, "Real-time, in situ film thickness metrology in a 10 Torr W chemical vapor deposition process using an acoustic sensor," *Journal of Vacuum Science & Technology B,* vol. 21, pp. 1055-1063, May-Jun 2003.
[63] Y. Cai, L. Henn-Lecordier, G. W. Rubloff, R. Sreenivasan, J. O. Choo, and R. A. Adomaitis, "Multiplexed mass spectrometry for real-time sensing in a spatially programmable chemical vapor deposition reactor," *Journal of Vacuum Science & Technology B,* vol. 25, pp. 1288-1297, 2007.

[64] S. Cho, L. Henn-Lecordier, Y. J. Liu, and G. W. Rubloff, "In situ mass spectrometry in a 10 Torr W chemical vapor deposition process for film thickness metrology and real-time advanced process control," *Journal of Vacuum Science & Technology B,* vol. 22, pp. 880-887, 2004.

[65] J. O. Choo, R. A. Adomaitis, L. Henn-Lecordier, Y. Cai, and G. W. Rubloff, "Development of a spatially controllable chemical vapor deposition reactor with combinatorial processing capabilities," *Review of Scientific Instruments,* vol. 76, 2005.

[66] Trinity College School of Physics, URL:www.tcd.ie/Physics/Surfaces/images/elli_dia.JPG, accessed Sept. 2009.

[67] H. G. Tompkins, McGahan, W. A., *Spectroscopic ellipsometry and reflectometry, a user's guide*: Wiley-Interscience, 1999.

[68] R. Matero, A. Rahtu, and M. Ritala, "In situ quadrupole mass spectrometry and quartz crystal microbalance studies on the atomic layer deposition of titanium dioxide from titanium tetrachloride and water," *Chemistry of Materials,* vol. 13, pp. 4506-4511, 2001.

[69] R. A. Matero, A. Rahtu, and M. Ritala, "In situ reaction mechanism studies on the atomic layer deposition of Al2O3 from (CH3)(2)AlCl and water," *Langmuir,* vol. 21, pp. 3498-3502, Apr 2005.

[70] M. Rodahl, F. Hook, A. Krozer, P. Brzezinski, and B. Kasemo, "Quartz crystal microbalance setup for frequency and Q-factor measurements in gaseous and liquid environments," *Review of Scientific Instruments,* vol. 66, pp. 3924-3930, Jul 1995.

[71] S. B. S. Heil, J. L. van Hemmen, M. de Sanden, and W. M. M. Kessels, "Reaction mechanisms during plasma-assisted atomic layer deposition of metal oxides: A case study for Al2O3," *Journal of Applied Physics,* vol. 103, 2008.

[72] E. Langereis, S. B. S. Heil, H. C. M. Knoops, W. Keuning, M. C. M. van de Sanden, and W. M. M. Kessels, "In situ spectroscopic ellipsometry as a versatile tool for studying atomic layer deposition," *Journal of Physics D-Applied Physics,* vol. 42, p. 19, Apr 2009.

[73] E. Langereis, S. B. S. Heil, M. C. M. van de Sanden, and W. M. M. Kessels, "In situ spectroscopic ellipsometry study on the growth of ultrathin TiN films by plasma-assisted atomic layer deposition," *Journal of Applied Physics,* vol. 100, 2006.

[74] W. A. M. H. G. Tompkins, *Spectroscopic ellipsometry and reflectometry, a user's guide*: John Wiley and sons, Inc., 1999.

[75] J. W. Elam, M. Schuisky, J. D. Ferguson, and S. M. George, "Surface chemistry and film growth during TiN atomic layer deposition using TDMAT and NH3," *Thin Solid Films,* vol. 436, pp. 145-156, Jul 2003.

[76] R. K. Grubbs, N. J. Steinmetz, and S. M. George, "Gas phase reaction products during tungsten atomic layer deposition using WF6 and Si2H6," *Journal of Vacuum Science & Technology B,* vol. 22, pp. 1811-1821, Jul-Aug 2004.

[77] J. Sterner, J. Kessler, and L. Stolt, "XPS instrument coupled with ALCVD reactor for investigation of film growth," *Journal of Vacuum Science & Technology a-Vacuum Surfaces and Films,* vol. 20, pp. 278-284, 2002.

[78] Y. Won, S. Park, J. Koo, S. Kim, J. Kim, and H. Jeon, "Initial reaction of hafnium oxide deposited by remote plasma atomic layer deposition method," *Applied Physics Letters,* vol. 87, 2005.

[79] H. S. Chang, H. Hwang, M. H. Cho, and D. W. Moon, "Investigation of the initial stage of growth of HfO2 films on Si(100) grown by atomic-layer deposition using in situ medium energy ion scattering," *Applied Physics Letters,* vol. 86, 2005.

[80] S. Cho, G. W. Rubloff, M. E. Aumer, D. B. Thomson, and D. P. Partlow, "Real-time material quality prediction, fault detection, and contamination control in AlGaN/GaN high electron mobility transistor metalorganic chemical vapor deposition process using in situ chemical sensing," *Journal of Vacuum Science & Technology B,* vol. 23, pp. 1849-1855, 2005.

[81] J. J. Chambers, K. Min, and G. N. Parsons, "Endpoint uniformity sensing and analysis in silicon dioxide plasma etching using in situ mass spectrometry," *Journal of Vacuum Science & Technology B,* vol. 16, pp. 2996-3002, 1998.

[82] S. Thomas, H. H. Chen, C. K. Hanish, J. W. Grizzle, and S. W. Pang, "Minimized response time of optical emission and mass spectrometric signals for optimized endpoint detection," *Journal of Vacuum Science & Technology B,* vol. 14, pp. 2531-2536, 1996.

[83] T. Gougousi, Y. H. Xu, J. N. Kidder, G. W. Rubloff, and C. R. Tilford, "Process diagnostics and thickness metrology using in situ mass spectrometry for the chemical vapor deposition of W from H-2/WF6," *Journal of Vacuum Science & Technology B,* vol. 18, pp. 1352-1363, 2000.

[84] J. Niinisto, A. Rahtu, M. Putkonen, M. Ritala, M. Leskela, and L. Niinisto, "In situ quadrupole mass spectrometry study of atomic-layer deposition of ZrO2 using Cp2Zr(CH3)(2) and water," *Langmuir,* vol. 21, pp. 7321-7325, 2005.

[85] A. Rahtu, K. Kukli, and M. Ritala, "In situ mass spectrometry study on atomic layer deposition from metal (Ti, Ta, and Nb) ethoxides and water," *Chemistry of Materials,* vol. 13, pp. 817-823, 2001.

[86] M. Juppo, A. Rahtu, and M. Ritala, "In situ mass spectrometry study on surface reactions in atomic layer deposition of TiN and Ti(Al)N thin films," *Chemistry of Materials,* vol. 14, pp. 281-287, 2002.

[87] T. Aaltonen, A. Rahtu, M. Ritala, and M. Leskela, "Reaction mechanism studies on atomic layer deposition of ruthenium and platinum," *Electrochemical and Solid State Letters,* vol. 6, pp. C130-C133, 2003.

[88] J. O. Choo, R. A. Adomaitis, G. W. Rubloff, L. Henn-Lecordier, and Y. J. Liu, "Simulation-based design and experimental evaluation of a spatially controllable CVD reactor," *Aiche Journal,* vol. 51, pp. 572-584, 2005.

[89] Y. Xu, T. Gougousi, L. Henn-Lecordier, Y. Liu, S. Cho, and G. W. Rubloff, "Thickness metrology and end point control in W chemical vapor deposition process from SiH4/WF6 using in situ mass spectrometry," *Journal of Vacuum Science & Technology B,* vol. 20, pp. 2351-2360, 2002.

[90] C. Soto, R. Wu, D. W. Bennett, and W. T. Tysoe, "Infrared-spectroscopy of trimethylaluminum and dimethyl aluminum chloride adsorbed on alumina," *Chemistry of Materials,* vol. 6, pp. 1705-1711, 1994.

[91] C. Contescu, A. Contescu, and J. A. Schwarz, "Thermodynamics of proton binding at the alumna/aqueous solution interface - a phenomenological approach," *Journal of Physical Chemistry,* vol. 98, pp. 4327-4335, 1994.

[92] T. Morimoto, M. Nagao, and F. Tokuda, "Relation between amounts of chemisorbed and physisorbed water on metal oxides," *Journal of Physical Chemistry,* vol. 73, pp. 243-&, 1969.

[93] P. Raghu, C. Yim, F. Shadman, and E. Shero, "Susceptibility of SiO2, ZrO2, and HfO2 dielectrics to moisture contamination," *Aiche Journal,* vol. 50, pp. 1881-1888, 2004.

[94] K. S. Chang, M. L. Green, J. Suehle, E. M. Vogel, H. Xiong, J. Hattrick-Simpers, I. Takeuchi, O. Famodu, K. Ohmori, P. Ahmet, T. Chikyow, P. Majhi, B. H. Lee, and M. Gardner, "Combinatorial study of Ni-Ti-Pt ternary metal gate electrodes on HfO2 for the advanced gate stack," *Applied Physics Letters,* vol. 89, Oct 2 2006.

[95] I. Takeuchi, O. O. Famodu, J. C. Read, M. A. Aronova, K. S. Chang, C. Craciunescu, S. E. Lofland, M. Wuttig, F. C. Wellstood, L. Knauss, and A. Orozco, "Identification of novel compositions of ferromagnetic shape-memory alloys using composition spreads," *Nature Materials,* vol. 2, pp. 180-184, Mar 2003.